

The UNIVERSITY OF HAWAII  
LIBRARY

JUL 18 1960

# Philosophical Magazine

FIRST PUBLISHED IN 1798

## A Journal of Theoretical Experimental and Applied Physics

Vol. 5

March 1960  
*Eighth Series*

No. 51

25s. 0d., plus postage  
Annual Subscription £13 10s. 0d., payable in advance



*Printed and Published by*

**TAYLOR & FRANCIS LTD**  
RED LION COURT, FLEET STREET, LONDON, E.C.4

# THE PHILOSOPHICAL MAGAZINE

## *Editor*

Professor N. F. MOTT, M.A., D.Sc., F.R.S.

## *Editorial Board*

Sir LAWRENCE BRAGG, O.B.E., M.C., M.A., D.Sc., F.R.S.

Sir GEORGE THOMSON, M.A., D.Sc., F.R.S.

Professor A. M. TYNDALL, C.B.E., D.Sc., F.R.S.

AUTHORS wishing to submit papers for publication in the Journal should send manuscripts directly to the Publishers.

Manuscripts should be typed in *double* spacing on one side of quarto (8×10 in.) paper, and authors are urged to aim at absolute clarity of meaning and an attractive presentation of their texts.

References should be listed at the end in alphabetical order of authors and should be cited in the text in terms of author's name and date. Diagrams should normally be in Indian ink on white card, with lettering in soft pencil, the captions being typed on a separate sheet.

A leaflet giving detailed instructions to authors on the preparation of papers is available on request from the Publishers.

Authors are entitled to receive 25 offprints of a paper in the Journal free of charge, and additional offprints can be obtained from the Publishers.

The *Philosophical Magazine* and its companion journal, *Advances in Physics*, will accept papers for publication in experimental and theoretical physics. The *Philosophical Magazine* publishes contributions describing new results, letters to the editor and book reviews. *Advances in Physics* publishes articles surveying the present state of knowledge in any branch of the science in which recent progress has been made. The editors welcome contributions from overseas as well as from the United Kingdom, and papers may be published in English, French and German.

## Point Defects in Platinum†

By G. R. PIERCY

Atomic Energy of Canada Limited, Chalk River, Ontario

[Received August 24, 1959]

### ABSTRACT

An investigation was made of the mobility and types of point defect introduced in platinum by deformation in liquid nitrogen, quenching into water from 1600°C, or reactor irradiation at 50°C. In all cases the activation energy for motion of the defect was determined from measurements of electrical resistivity. Measurements of density, hardness, and x-ray line broadening were also made where applicable.

These experiments indicated that the principal defects remaining in platinum after irradiation were single vacant lattice sites and after quenching were pairs of vacant lattice sites. Those present after deformation in liquid nitrogen were single vacant lattice sites and another type of defect, perhaps interstitial atoms.

### § 1. INTRODUCTION

ALTHOUGH an equilibrium number of the point defects, vacancies and interstitial atoms are present in a metal, a larger concentration is thought to be introduced by cold working, quenching, or irradiating. The concentration, distribution and type of the extra defects retained in the sample will depend on the temperature and method of production. If the defects are mobile at the temperature of production, they will move about the lattice until they reach a position of lower energy where they are trapped or annihilated. Foreign atoms are expected to act as trapping centres, while grain boundaries voids, free surfaces, and perhaps dislocations will act as annihilation centres or sinks. An interesting review on the effect of lattice defects on some physical properties of metals was recently given by Broom and Ham (1958).

Many different physical properties have been measured to detect vacancies and interstitial atoms. Electrical resistivity, which is very sensitive to their presence, is often used to measure their mobility. From this the activation energy required for one atomic jump of the defect can be calculated and the type of defect can be inferred. Also, the number of jumps required by the defect to reach the sink can be determined, from which the type of sink can be inferred. Unfortunately, all point defects increase the resistivity so that changes in other physical

---

† Communicated by the Author.



properties are necessary to determine exactly what type of defect is present. Changes in density and lattice parameter should discriminate between vacancies and interstitial atoms. The x-ray line width is unchanged by point defects but indicates the amount of lattice strain produced by dislocations in deformed samples.

In the present experiments the point defects were introduced by cold work at  $-196^{\circ}\text{C}$ , by quenching from above  $1600^{\circ}\text{C}$ , and by fast neutron irradiation at  $50^{\circ}\text{C}$ . The electrical resistivity, density, lattice parameter, hardness, and x-ray line width were measured before and after the defects were introduced into the sample. In addition, the mobility of the defects was determined from changes of electrical resistivity due to heat treatment.

## § 2. CHOICE OF MATERIAL

The choice of sample material for these experiments was mainly determined by the irradiation conditions. The sample should have a high melting point in order to retain a maximum amount of radiation damage at  $50^{\circ}\text{C}$ , the temperature of irradiation. In addition it should have a low gamma activity after irradiation. These two conditions, combined with the usual requirements of simple crystal structure, high purity, and good surface properties, made platinum the obvious choice.

The platinum used was Johnson Matthey and Mallory thermocouple grade (99.99%), so that direct comparison could be made with the platinum self-diffusion experiments of Kidson and Ross (1957), which were made on similar material.

## § 3. METHODS FOR INTRODUCING DEFECTS INTO PLATINUM

### 3.1. *Deformation*

The 0.010 in. diameter platinum wires were annealed in air at  $900^{\circ}\text{C}$ . for 30 min, and then extended 8% in liquid nitrogen. They were removed from the extension apparatus while immersed in liquid nitrogen. Since the potential leads were silver-soldered to the sample before the extension, the resistivity could be measured after any recovery anneal above  $-196^{\circ}\text{C}$ .

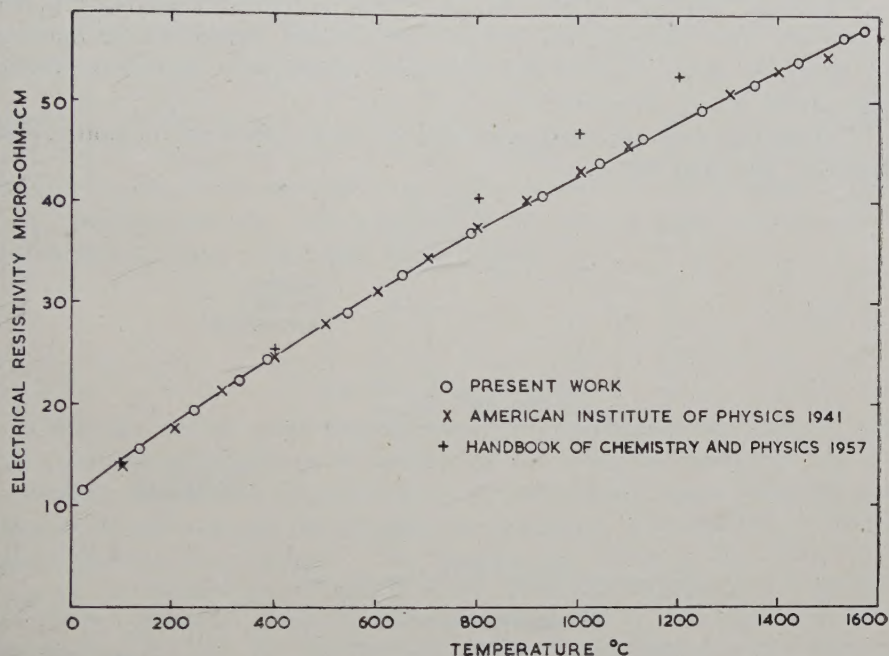
The hardness samples were 0.1 in. thick platinum flats rolled to 8% reduction with the sample immersed in liquid nitrogen between each pass.

### 3.2. *Quenching*

An electric current was used to heat a 4 in. long 0.010 in. diameter platinum wire. The potential leads of 0.003 in. diameter platinum wire were spot-welded one inch from the ends of the sample. The temperature of the heated sample was determined from its resistance. The calibration curve for resistance against temperature is shown in fig. 1.

The sample was cooled rapidly (quenched) by sudden immersion into cold water. To reduce the deformation during this quench, the axis of the wire sample was perpendicular to the surface of the water. The time taken to cool the sample was measured by retaining the heating current and recording the voltage across the sample on an oscillograph. A typical quench, shown in fig. 2 (Pl. 25), gives a time of 0.02 sec to cool from 1600°C to 20°C.

Fig. 1



Electrical resistivity of thermocouple grade platinum. No correction was made for the change in sample dimensions with temperature.

### 3.3. Fast Neutron Radiation

The 0.010 in. diameter platinum wire was annealed in air at 900°C for 30 min and then irradiated at 50°C inside a uranium tube in the NRX reactor (Cook and Cushing 1953). Half the fast neutrons hitting the sample were from the uranium tube and had a fission energy spectrum. The other half from neighbouring fuel rods had the usual  $E^{-1}$  spectrum. The definition of fast neutrons used in this report is neutrons with energy above 1200 eV. This is the minimum energy neutron capable of knocking a platinum atom from its lattice site.

After irradiation, the platinum wires were decontaminated and platinum potential leads spot-welded on.



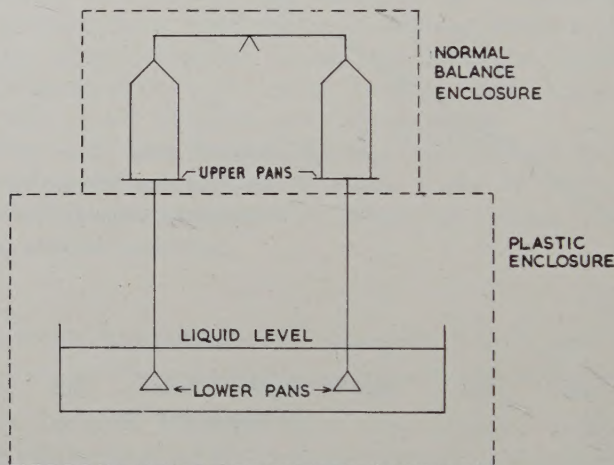
## § 4. METHODS FOR DETECTING DEFECTS IN PLATINUM

4.1. *Electrical Resistivity*

Potential leads were spot-welded to the wire samples, which were 0.010 in. in diameter, and the electrical resistances measured in liquid nitrogen. The values obtained were corrected to a constant nitrogen bath temperature by measuring the resistance of an annealed sample in the same bath. The electrical circuit was made completely of copper with low thermal e.m.f. solder at all joints. A 100 mA current was used with the bath vigorously stirred to prevent temperature fluctuations due to gas bubbles forming on the sample. The potential was read to 0.1 microvolt. By reversing the sample current and potentiometer battery to eliminate stray e.m.f.'s, the resistance values were reproducible to one part in thirty thousand.

The samples were annealed in silicone oil up to 250°C and in molten salt between 250° and 900°C.

Fig. 3



Schematic diagram showing the balance assembly for density measurements.

4.2. *X-ray Line Width*

A long 0.010 in. diameter platinum wire was extended 8% in liquid nitrogen. Sections of it were spot-welded side by side on a platinum frame to fit the diffractometer. The half widths of the (331), (420) and (422) x-ray lines were then measured after annealing the wire sample assembly at successively higher temperatures.

4.3. *Density*

The density of platinum was determined by weighing a 13 g sample in air and water with a weight sensitivity of 0.01 milligrams. The density of the sample was directly compared with an annealed reference sample of

the same size using the system shown in fig. 3. The sample was put in the upper left pan and the reference sample in the upper right pan to obtain the difference between their weights in air. The sample was then placed under the liquid in the lower left pan and the standard in the lower right pan, to obtain the difference between their weights in liquid. The calculations for this method of density determination are given elsewhere (Piercy 1958). This is a very sensitive method for measuring changes in density since the measurements are not strongly dependent on the liquid density, air density, or temperature. Of course, the absolute value depends on the accuracy of the density taken for the reference sample.

Distilled water with the air removed was used for the density measurements. However, hysteresis in the contact angle between water and the 0.003 in. tantalum wire, caused the measured weight to depend on the direction of vertical motion of the balance pan. This effect was markedly reduced by using a solution of 0.08% wetting agent (Kodak Photoflo) in distilled water, which resulted in a density reproducibility of 0.005% for a 13 g platinum sample. The addition of the wetting agent did not affect the absolute value within this limit of error.

#### 4.4. Reaction Kinetics

Once the excess point defects were introduced into the sample, the preliminary investigation of measuring the drop in resistivity due to annealing the sample for equal times at successively higher temperatures (an isochronal anneal) determined the minimum temperatures at which these defects were mobile. The decrease in resistance for each 5 min anneal was plotted as a function of the annealing temperature, a typical result for deformed platinum being shown in fig. 4. Once the temperature range for recovery was known, the activation energy was found by measuring the change in slope of the isothermal resistivity-time curve when the temperature was raised by 10°C. The value for the activation energy  $\Delta H_2$  was calculated from the usual equation

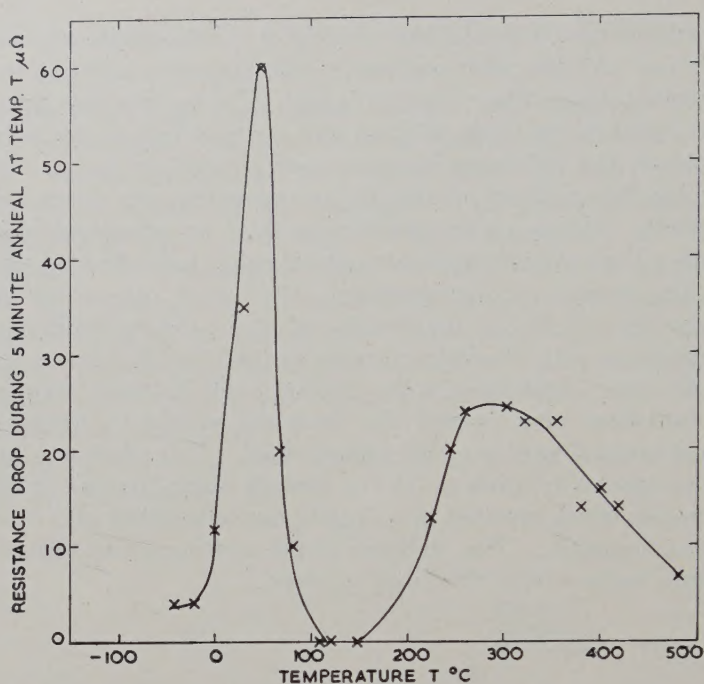
$$\Delta H_2 = \frac{T_1 T_2}{T_2 - T_1} K \log_e (S_2/S_1) \quad . \quad . \quad . \quad . \quad . \quad (1)$$

where  $K$  is Boltzmann's constant,  $S_1$  is the final slope of the resistivity-time curve at absolute temperature  $T_1$  and  $S_2$  is the initial slope after raising the temperature from  $T_1$  to  $T_2$ . This process was repeated until there was no further drop in resistivity. A typical set of curves for irradiated platinum is shown in fig. 5.

The slope at the end of each curve was determined in the following manner: the slope at the midpoint of a curve between two experimental points A and B was assumed equal to that of the straight line joining A and B. Therefore by measuring seven experimental points on the isothermal

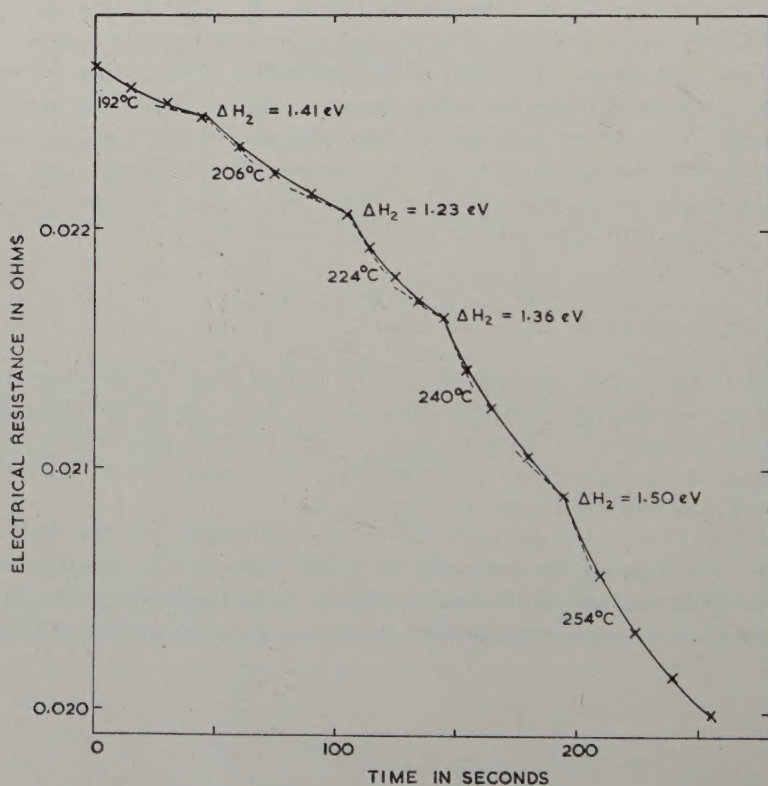


Fig. 4



Isochronal recovery of platinum after deformation in liquid nitrogen. The drop in sample resistance for successive anneals of 5 min at temperature  $T$  is plotted against annealing temperature.

Fig. 5

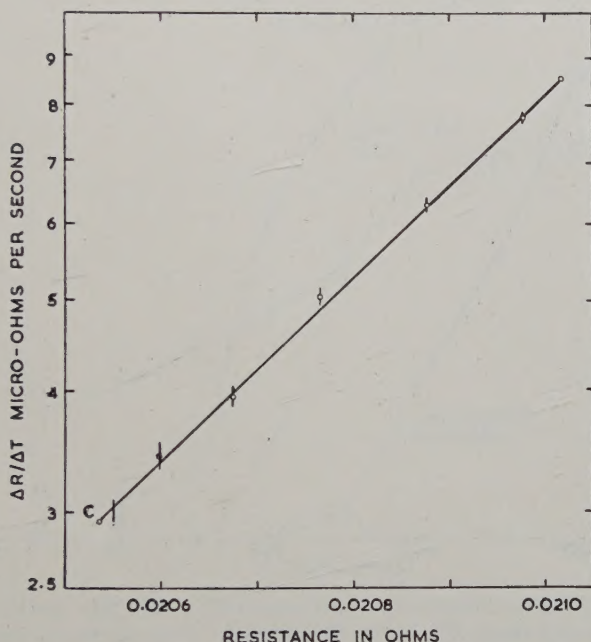


A typical set of curves to determine the activation energy required for recovery of irradiated platinum.



anneal, the values for the slope of the curve at the six intermediate points were determined. Then, by plotting the curve for these values of slope against the resistivity at these intermediate points and extrapolating the curve a short distance, the value for the slope at the end of the curve was obtained. The logarithm of the slope against the resistance at the intermediate points was usually plotted in order to have a straighter line to extrapolate. A typical example for irradiated platinum is shown in fig. 6. This is one of the few methods that determines the slope using all the experimental points equally.

Fig. 6



Determination of slope at the end of an isothermal annealing curve. The log of the slope found at a point midway between two experimental points is plotted against the electrical resistance at that point. The line is extrapolated to point C to obtain the slope at the end of the isothermal curve.

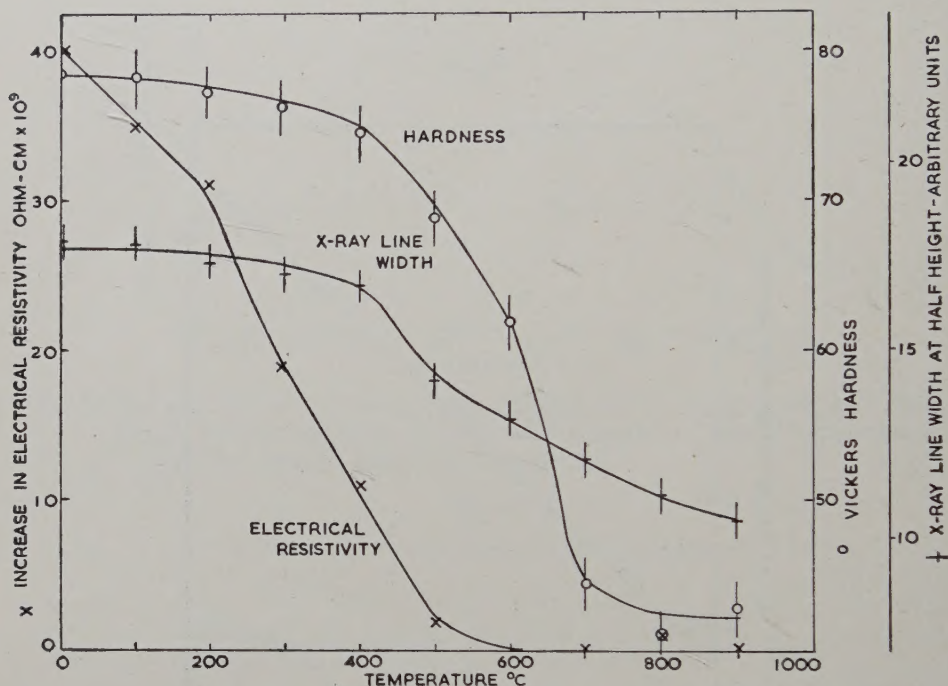
When the activation energy was known, the number of jumps required by the defect to reach the sink was determined from the slope of the curve obtained by plotting the logarithm of the fraction of resistivity increase remaining against the time at constant annealing temperature and applying eqn. (9) of the Appendix. The order of reaction was found from the same isothermal anneal using the method of Meehan and Brinkman (1956).

## § 5. RESULTS AND OBSERVATIONS

5.1. *Changes in Physical Properties*

The electrical resistivity isochronal recovery curve for platinum extended 8% in liquid nitrogen (fig. 4) has two distinct recovery stages; one below 100°C in which 0.004 micro-ohm-cm recovers, and one between 100°C and 600°C in which 0.024 micro-ohm-cm recovers. For comparison,

Fig. 7



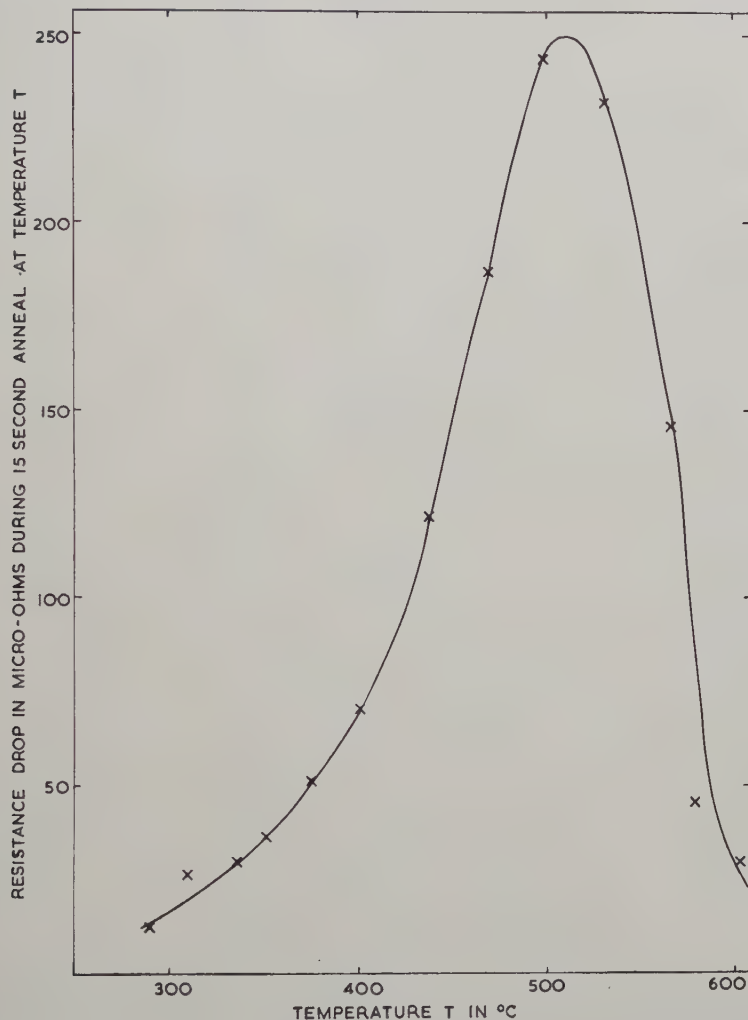
Recovery of electrical resistivity, hardness and x-ray line width of platinum samples deformed 8% in liquid nitrogen. Successive anneals for 30 min every 100°C were used.

the electrical resistivity of platinum in liquid nitrogen is 1.85 micro-ohm-cm. There was no appreciable recovery below -50°C which is contrary to the experiments of Manintveld (1954). The recovery of x-ray line width, electrical resistivity and hardness for platinum deformed 8% in liquid nitrogen are shown together in fig. 7. Because the temperature intervals are larger, this curve for the recovery of electrical resistivity does not resolve the two peaks shown in fig. 4. The x-ray line width does not change until nearly all the increase in electrical resistivity has recovered, indicating that both stages in the recovery of electrical resistivity shown in fig. 4 are mainly due to point defects, rather than to annihilation or redistribution of dislocations. However, some annihilation of dislocations



may be occurring at the very end of the recovery of electrical resistivity. The recovery of the hardness and x-ray line width above  $400^{\circ}\text{C}$  is probably due to recrystallization.

Fig. 8

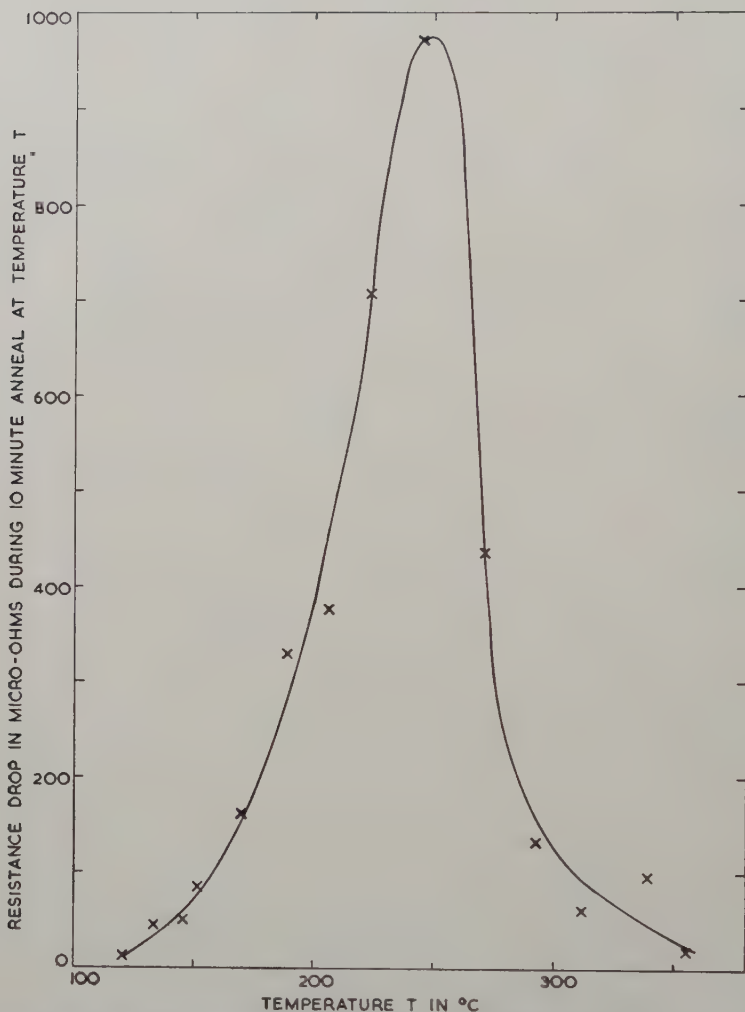


Isochronal recovery of quenched platinum showing the drop in sample resistance for successive anneals of 15 sec at temperature  $T$ .

The isochronal recovery of quenched platinum shown in fig. 8 has one recovery stage in the region  $300$  to  $600^{\circ}\text{C}$ , during which a resistivity drop of  $0.12$  micro-ohm-cm occurs. There was no further recovery on annealing up to  $800^{\circ}\text{C}$ . The isochronal anneal of irradiated platinum shown in fig. 9 also has only one recovery state and this occurs in the region  $130$ – $350^{\circ}\text{C}$ . However, the large decrease of  $0.48$  micro-ohm-cm occurs here. There was no further recovery on annealing up to  $900^{\circ}\text{C}$ .

The recovery of the density and yield stress of irradiated platinum was examined to determine whether these recovered at the same rate as the electrical resistance. The results shown in table 1 indicate that both the density and the yield stress recover at the same rate as the electrical resistance and, therefore, are probably due to the same defect. Since the

Fig. 9



Isochronal recovery of irradiated platinum showing the drop in sample resistance for successive anneals of 10 min at temperature  $T$ .

density decrease is 0.07% due to irradiation, while the lattice parameter change for the same irradiation is less than 0.005% (Tuxworth 1958 unpublished data), the defects remaining in the sample are probably single, double, or clusters of vacancies.



Table 1. The Recovery of Electrical Resistivity, Density, and Mechanical Properties of Irradiated Platinum

Treatment	Electrical resistivity in liq. N <sub>2</sub> $\mu\Omega$ cm $\pm 0.0001$ $\mu\Omega$ cm	% resistivity increase remaining	Density at 22.2°C g/cm <sup>3</sup> $\pm 0.001$ g/cm <sup>3</sup>	% density decrease remaining	Ultimate tensile strength p.s.i. $\pm 1000$ p.s.i.	% Ultimate strength increase remaining	Proportional limit p.s.i. $\pm 1000$ p.s.i.	% Proportional limit increase remaining
Annealed prior to irradiation	1.850	—	21.4413	—	19000	—	8000	—
Irradiated with $2 \times 10^{20}$ fast n/sq. cm	2.52	100	21.4255	100	26300	100	15000	100
Irradiated plus 50 min 200°C	2.22	55	21.4335	49	23000	54	10800	40
Irradiated plus 180 hr 200°C	1.94	13	21.4396	11	20200	—	8200	—

From the results shown in table 1, the ratio of the resistivity change to fractional volume change due to irradiation is  $9 \times 10^{-4}$  ohm-cm. Since this is comparable with the value  $3 \times 10^{-4}$  ohm-cm found in gold wire that was quenched from 900°C (Bauerle and Koehler 1957), the defects in irradiated platinum are probably similar to those in quenched gold, i.e. isolated or small grouping of vacancies rather than large clusters. If one vacancy in the irradiated platinum produces an effective volume change of 0.5 atomic volumes (the number will be less than 1.0 due to relaxation about the vacancy), then the resistivity per atomic per cent vacancies when calculated from the ratio of resistivity change to fractional volume change is 4.5 micro-ohm-cm. This value, which is about three times that predicted for copper (Overhauser and Gorman 1956) is a reasonable resistivity for vacancies in platinum and will be used for later calculations of defect concentrations produced in platinum by other means. The concentration of vacancies determined for the irradiated sample by using this value is  $1.2 \times 10^{-3}$ .

The defect concentration produced by fast neutrons can be calculated from the theory of Seitz and Koehler (1956), and also the theory of Brinkman (1956). Taking the total elastic scattering cross section for fast neutrons to be 5.5 barns (Langsdorf *et al.* 1957), the concentration of defects produced in platinum which is irradiated with  $2 \times 10^{20}$  fast neutrons per square centimetre in NRX is 0.30 when calculated from the theory of Seitz and Koehler. On the other hand, Brinkman's estimate for the concentration of defects remaining in a displacement spike is only about 0.001 (Brinkman 1954). Therefore, this should be the limiting value when all the atoms of the sample have been in at least one displacement spike, as would probably occur with the high integrated flux used here. The concentration of defects measured in this experiment, however, is expected to be much lower than the actual numbers produced, due to annihilation of the vacancies by interstitial atoms that are mobile during irradiation. Therefore, the experimental value of 0.0012 deduced from the density and resistivity change indicates that Brinkman's estimate of 0.001 for the concentration of defects remaining in a displacement spike is much too low if the displacement spike concept is applicable to platinum.

### 5.2. Reaction Kinetics

The results for the activation energy measurements on extended, quenched and irradiated platinum are given in table 2. They were all measured by the change in slope of an isothermal recovery curve when the temperature was raised.

A lattice distortion or strain will alter the distance between atoms and hence may alter the activation energy required for the atomic jump process. Since a comparison between the activation energy of recovery after cold working, quenching, and irradiating is required, and these do not produce the same lattice strain in the metal, the possible change in



activation energy with lattice strain was investigated using an irradiated sample. A load equal to half the proportional limit of platinum at 400°C was hung from an irradiated sample during recovery. Although this increased the rate of recovery by a factor of two, the activation energy was still the same within experimental error.

Table 2. Activation Energy for the Recovery of Platinum after Deformation, Quenching or Irradiation

Treatment	Temperature range °C	Activation energy ev	Number of determinations
Extended 8–10% in liquid nitrogen	38 to 135	$0.73 \pm 0.06^\dagger$	5
Extended 8–10% in liquid nitrogen and annealed to remove lower recovery stage	230 to 360	$1.43 \pm 0.09$	7
Quenched from above 1600°C to 20°C in less than 0.04 sec	240 to 370	$1.13 \pm 0.11$	14
Irradiated at 50°C with $6 \times 10^{19}$ fast neutrons per square centimetre	190 to 280	$1.40 \pm 0.11$	11

† The limits given are the standard deviations of all measurements taken.

The average values of activation energy from table 2 were used to calculate the order of reaction and the number of jumps required by the defect to reach the sink. These, together with the concentration of defects (based on recovery of electrical resistivity, assuming 4.5 micro-ohm-cm per atomic percent defects) are shown in table 3. The activation energy for the recovery of irradiated platinum, the only case for which two identical samples were available, was also measured by the technique of Meehan and Brinkman (1956). The result shown in fig. 10 and given in table 3 is within the limit of error of the slope change method.

## § 6. DISCUSSION

A comparison between the present results for the reaction kinetics and other investigators are given in table 4. The values for activation energy do not agree except for quenched platinum. Since the purity of Manintveld's extended platinum was not reported, the difference in results may be due to an impurity effect. Unfortunately, his annealing experiments were not taken above 90°C. Dugdale's results on platinum irradiated or extended at room temperature (Dugdale 1952) are both the same

Table 3. Summary of Parameters for the Motion of Defects in Platinum

Treatment	Temperature range of recovery °C	Activation energy ev	Order of reaction	Number of jumps to sink† for given amount of recovery remaining	Concentration of defects‡
8-10% extension in liquid nitrogen	0 to 100	0.73 ± 0.06	1.8 to 2.2	7 × 10 <sup>6</sup> for 50% remaining 2 × 10 <sup>7</sup> for 25% remaining	1 × 10 <sup>-5</sup>
Quenched from above 1600°C to 20°C in 0.03 sec	200 to 400	1.43 ± 0.09	5.05	3 × 10 <sup>4</sup> for 75% remaining 1 × 10 <sup>5</sup> for 50% remaining 7 × 10 <sup>6</sup> for 25% remaining	6 × 10 <sup>-5</sup>
Irradiated with n/sq. cm at 50°C	300 to 500	1.13 ± 0.12	1.46	6 × 10 <sup>8</sup> for 75% remaining 8 × 10 <sup>8</sup> for 50% remaining 1 × 10 <sup>9</sup> for 25% remaining	3 × 10 <sup>-4</sup>
	150 to 400	1.40 ± 0.11 1.46 ± 0.05§	2.8	1 × 10 <sup>3</sup> for 75% remaining 2 × 10 <sup>3</sup> for 50% remaining 7 × 10 <sup>3</sup> for 25% remaining	1.2 × 10 <sup>-3</sup>

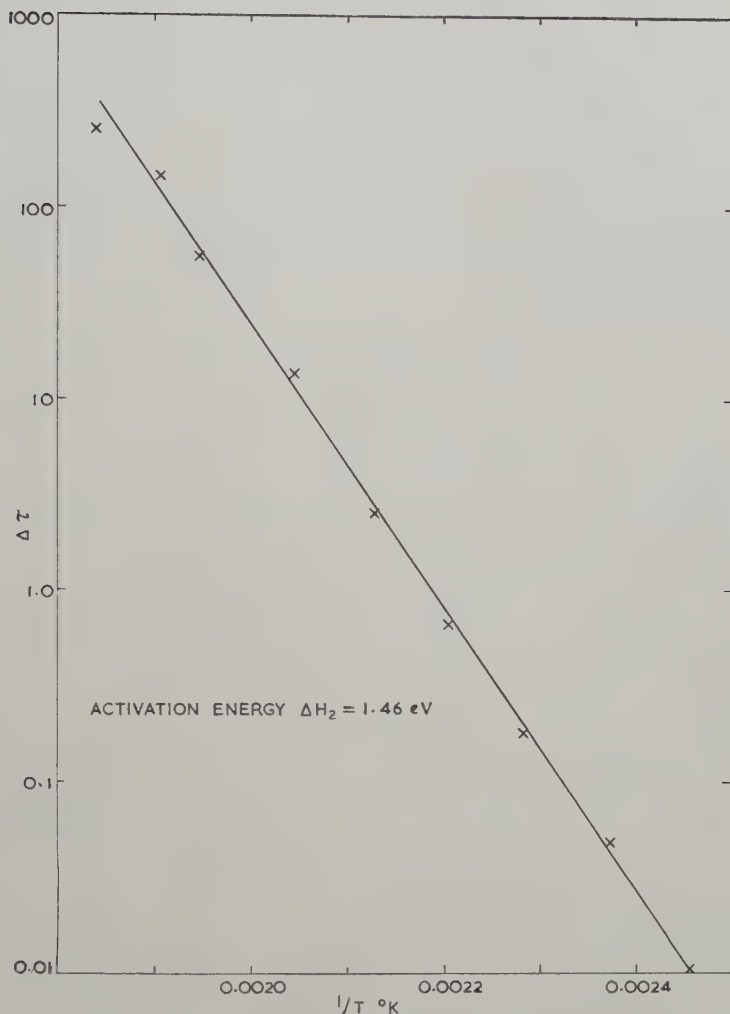
† Number of jumps calculated with eqn. (9) of the Appendix.

‡ The concentration is calculated from electrical resistivity measurements assuming 4.5 micro-ohm-centimetres per atom percent defects.

§ By the method of Meehan and Brinkman (Meehan 1956)—all others by the slope-change method from table 2.



Fig. 10



Activation energy for the recovery of irradiated platinum determined by the method of Meehan and Brinkman (Meehan 1956). The time  $\Delta\tau$  required at  $196^\circ\text{C}$  for the same recovery occurring 10 min at temperature  $T$  of the isochronal anneal is plotted against  $1/T$ . The slope of the line gives an activation energy of 1.46 eV for the whole recovery process.

but are significantly below those reported here. However, he made only three activation energy measurements and all were taken after about 8% recovery. Once again, the difference may be due to sample impurity since his is unspecified. Because of these discrepancies, no single model can explain all the past results. Therefore a model will be proposed to explain the results of the present experiments in which point defects were produced by three methods and in which all measurements were made under the same conditions.

Since the density of platinum decreased after irradiation while the lattice parameter showed no significant change, the defects remaining after a room temperature irradiation are probably vacancies, divacancies or vacancy clusters. Because the changes in density and electrical resistance recover at the same rate after irradiation, they are probably caused by the same point defect. Therefore, the recovery of electrical resistivity in irradiated platinum that requires an activation energy of 1.43 eV is probably due to vacancies, divacancies, or vacancy clusters.

There are several arguments that strongly suggest the defects in irradiated platinum are isolated or small groups of vacancies rather than large clusters. The first, mentioned previously, is the agreement between the

Table 4. A Summary of Activation Energies Measured for the Recovery of Platinum

Method of introducing defects	Recovery temperature range examined °C	Activation energy eV	Reference
Extended at $-196^{\circ}\text{C}$	$-150$ to $-70$	0.22	Manintveld 1954
Extended at $20^{\circ}\text{C}$	$-10$ to $70$	0.99	" "
Extended at $-196^{\circ}\text{C}$	$70$ to $100$	1.19	Dugdale 1952
	$0$ to $100$	0.73	Present work
	$200$ to $400$	1.43	" "
Quenching from above $1600^{\circ}\text{C}$	—	1.1	Lazarev and
	$300$ to $500$	1.10	Ovcharenko 1955
	$300$ to $500$	1.13	Bradshaw and Pearson 1956
Quenching from $1100^{\circ}\text{C}$ to $1400^{\circ}\text{C}$	$450$ to $580$	1.42	Ascoli <i>et al.</i> 1958
	—	1.48	Bacchella <i>et al.</i> 1959
Reactor irradiation at $50^{\circ}\text{C}$	$70$ to $90$	1.19	Dugdale 1952
	$100$ to $300$	1.43	Present work

ratio of density decrease to resistivity increase in irradiated platinum with that found in quenched gold. The second, is the excellent agreement between the migration energy for defects produced by irradiation (1.43 eV) with those produced by quenching platinum from temperatures substantially below the melting point, 1.42 eV (Ascoli *et al.* 1958). A quench from these temperatures is expected to leave single vacancies while a quench from near the melting point may leave double vacancies (Koehler *et al.* 1957). The lower values of 1.1 eV required for defect migration after quenching from near the melting point as shown in table 4 are probably due to double vacancies.

The third argument that suggests the defects produced by irradiation are single vacancies, is the qualitative agreement between the measured migration energy of  $1.43 \pm 0.1$  ev and the calculated migration energy of  $1.65 \pm 0.15$  ev from the energy of self-diffusion in platinum of  $2.96 \pm 0.06$  ev (Kidson and Ross 1957) less the formation energy of vacancies in platinum  $1.30 \pm 0.1$  ev (Bradshaw and Pearson 1956, Ascoli *et al.* 1958, Bacchella *et al.* 1959).

The activation energy required for recovery of the electrical resistivity after 8% extension in liquid nitrogen was 0.73 and 1.43 ev. The higher value has already been attributed to the migration of single vacancies and the lower one is perhaps due to the release of interstitial atoms from trapping sites. Both vacancies and interstitial atoms may be produced by the crossing of screw dislocations during deformation.

The order of reaction is a measure of the rate of change of the number of jumps required by a defect to reach the sink during the recovery process. Once it rises above the value two, its interpretation becomes vague and in many cases may be caused by a nonrandom initial distribution of defects. This nonrandom distribution of defects is one possible explanation for the high order of reaction and the low number of jumps required for the recovery of irradiated platinum. If the damage from a fast neutron is concentrated in one small volume the local concentration of defects may be very high. Therefore the vacancies would require only a small number of jumps before combining with another vacancy, after which they could move more rapidly. Also, if the damage from fast neutrons is concentrated in a small volume, there may be other traps for vacancies such as dislocation rings or clusters of interstitial atoms that are produced by the same neutron. Therefore the vacancies would again require only a small number of jumps before reaching these sinks.

From the number of jumps required for the defect to reach a sink in the recovery of quenched and deformed platinum, an interpretation of the type of sink can be made. In the quenched sample with a defect concentration of  $3 \times 10^{-4}$ , the number of jumps ( $8 \times 10^8$ ) is much too high for recombination of defects. The low order of reaction 1.46 also discourages this interpretation. However, if the defects are going to dislocations, an argument which agrees with the observed number of jumps, an order of reaction equal to 1.0 might be expected. The higher order of reaction observed (1.46) may be caused by the change in dislocation network due to extensive climb of dislocations which absorb defects. Thus, the last defects will migrate to a much different distribution and perhaps even different type of dislocation network than was initially present.

The eight per cent extension of platinum is expected to increase the dislocation density from  $10^8$  to about  $10^{10}$  lines per square centimetre. Therefore, the number of jumps required by the defect to reach a dislocation will be reduced from  $10^7$  to  $10^5$  (Lomer and Cottrell 1955) which is similar to the number of jumps required for the defects to combine. The recovery of extended platinum at 60°C appears to be by defects





where  $t$  is the time,  $\Gamma$  the defect jump frequency, and  $p$  the probability per jump that a defect reaches a sink.

The jump frequency  $\Gamma$  also depends on three factors

$$\Gamma = Z(\alpha\nu) \exp(-\Delta F_2/KT) \quad . \quad . \quad . \quad . \quad . \quad (2)$$

where  $Z$  is the number of adjacent sites to which the defect may go,  $\alpha\nu$  is the frequency of attempts by the defect to move to each adjacent site, and  $\exp(-\Delta F_2/KT)$  is the fraction of time that a defect has sufficient free energy to jump.  $\nu$  is the vibration frequency of the atom, and  $\alpha$  is the fraction of these vibrations in each jump direction. The free energy required by the defect to jump is

$$\Delta F_2 = \Delta H_2 - T\Delta S_2 \quad . \quad . \quad . \quad . \quad . \quad (3)$$

where  $\Delta H_2$  is the activation energy required to move the defect one jump and  $\Delta S_2$  is the entropy change produced by the defect moving from one site to the saddle point midway between sites.

The probability per jump that a defect reaches a sink is equal to the fraction of lattice sites from which the defect is directly attracted to the sink. This depends on the concentration of sink sites, their distribution, and the maximum distance of attraction between the defect and sink. Therefore

$$p = j^{-1} = \beta C_s \quad . \quad . \quad . \quad . \quad . \quad (4)$$

where  $j$  is the average number of jumps required by the defect to reach the sink,  $C_s$  is the concentration of sink sites and  $\beta$  is a term depending on the sink distribution and the maximum distance of attraction between defect and sink. The term  $\beta C_s$  could well be called the 'effective sink concentration'.

Putting eqns. (2), (3), (4) into eqn. (1) gives:

$$S = -\frac{1}{R} \frac{dR}{dt} = -\frac{d(\ln R)}{dt} = Z\alpha\nu j^{-1} \exp(\Delta S_2/K) \exp(-\Delta H_2/KT) \quad (5)$$

where  $S$  is the slope of the graph  $\ln R$  vs. time. Solving for  $j$  gives:

$$j = Z\alpha\nu S^{-1} \exp(\Delta S_2/K) \exp(-\Delta H_2/KT). \quad . \quad . \quad . \quad (6)$$

$\Delta H_2$  is calculated from other experiments using eqn. (1) of the main text. Unfortunately the frequency factor  $Z\alpha\nu \exp(\Delta S_2/K)$  has not been measured directly, but each factor can be estimated. Because the total vibrational energy is considered in the  $\Delta H_2$  term in eqn. (6),  $\nu$  must be the frequency of the resultant vibration containing the total vibrational energy of the atom making the jump and  $\alpha$  is the fraction of these resultant vibrations in each jump direction. The Debye frequency is usually used for  $\nu$ . Bradshaw and Pearson (1956) and LeClaire (1953) take  $\alpha = 1$  but the value  $\alpha = Z^{-1}$  assumed by Jost (1952) seems more reasonable for vacancy diffusion since only the resultant vibration is considered. Because there are  $Z$  possible jump directions, the fraction of the resultant vibrations in any one jump direction will be about  $Z^{-1}$ . If the resultant vibration of an atom adjacent

to a vacancy is always in the direction of the vacancy, then  $\alpha = 1$ . This is unlikely, however, because each atom vibrates in phase with its nearest neighbours and the wavelength of vibration is usually greater than three to four atoms. The remaining factor,  $\exp(\Delta S_2/K)$ , was assumed by Bradshaw and Pearson (1956) to lie between one and ten.

Because of uncertainty in the choice of these parameters for the frequency factor, a more direct value was taken from the self diffusion measurements of Kidson and Ross (1957). Their measured value for  $D_0$  was  $0.33 \text{ cm}^2 \text{ sec}^{-1}$  which gives (LeClaire 1953)

$$\alpha \nu \exp [(\Delta S_1 + \Delta S_2)/K] = D_0/a^2 = 2.2 \times 10^{14} \quad . \quad . \quad . \quad (7)$$

where  $a = 3.9 \times 10^{-8} \text{ cm}$  is the lattice parameter and  $\Delta S_1$  is the vibrational entropy due to a vacancy at a lattice site. The left side of eqn. (7) is similar to the frequency factor in eqn. (6) except for the added  $\Delta S_1$  term. However, from calculations on the relative values of  $\Delta S_1$  and  $\Delta S_2$  (Huntington *et al.* 1955)

$$\exp(\Delta S_2/K) = 0.24 \exp [(\Delta S_1 + \Delta S_2)/K]. \quad . \quad . \quad . \quad (8)$$

Therefore by combining eqns. (7) and (8) with (6) and taking  $Z = 12$  for f.c.c. lattices,  $j$  becomes

$$j = 6.3 \times 10^{14} S^{-1} \exp(-\Delta H_2/KT) \quad . \quad . \quad . \quad (9)$$

where  $S$  is the slope of  $\ln R$  vs. time and  $\Delta H_2$  is the activation energy for recovery at temperature  $T$ . This equation was used to calculate the number of jumps required by the defect to reach the sink for all recovery stages investigated. The frequency factor may be incorrect if recovery other than vacancy diffusion occurs. This frequency factor is the same as that of Bradshaw and Pearson's (1956) using their assumptions ( $B = \exp(\Delta S_2/K) = 5$ ,  $\alpha = 1$ ,  $\nu = 10^{13}$ ) and including the extra  $Z$  term discussed in his later paper (Bradshaw and Pearson 1957).

An estimate of  $B = \exp(\Delta S_2/K)$  can be made from eqns. (7) and (8). If  $\alpha = Z^{-1}$ , which seems reasonable for vacancy diffusion, and  $\nu = 5 \times 10^{12}$ , the Debye frequency for platinum (Seitz 1940); then a value for  $B$  of 125 is required to match the diffusion results.

#### REFERENCES

- American Institute of Physics, 1941, *Temperature, Its Measurement and Control in Science and Industry* (New York: Reinhold).  
 ASCOLI, A., ASDENTE, M., GERMAGNOLI, E., and MANARA, A., 1958, *J. Phys. and Chem. of Solids*, **6**, 59.  
 BACCHELLA, G. L., GERMAGNOLI, E., and GRANATA, S., 1959, *J. appl. Phys.*, **30**, 748.  
 BAUERLE, J. E., and KOEHLER, J. S., 1957, *Phys. Rev.*, **107**, 1493.  
 BRADSHAW, F. J., and PEARSON, S., 1956, *Phil. Mag.*, **1**, 812; 1957, *Ibid.* **2**, 379.  
 BRINKMAN, J. A., 1954, *J. appl. Phys.*, **25**, 961; 1956, *Amer. J. Phys.*, **24**, 246.  
 BROOM, T., and HAM, R. K., 1958, *Vacancies and other point defects in Metals and Alloys* (Inst. of Metals Monograph 23).



- COOK, L. G., and CUSHING, R. L., 1953, *Acta Met.*, **1**, 539.
- DUGDALE, R. A., 1952, *Phil. Mag.*, **43**, 912.
- Handbook of Chemistry and Physics*, 1957 39th Ed. (Cleveland : Chemical Rubber).
- HUNTINGTON, H. B., SHIRN, G. A., and WAJDA, E. S., 1955, *Phys. Rev.*, **99**, 1085.
- JOST, W., 1952, *Diffusion in Solids, Liquids and Gases* (New York : Academic Press), p. 135.
- KIDSON, G. V., and ROSS, R., 1957, Proc. of 1957 UNESCO Radio-isotope Conference in Paris.
- KOEHLER, J. S., SEITZ, F., and BAUERLE, J. E., 1957, *Phys. Rev.*, **107**, 1499.
- LANGSDORF, Jr., A., LANE, R. O., and MONAHAN, J. E., 1957, *Phys. Rev.*, **107**, 1077.
- LAZAREV, B. G., and OVCHARENKO, O. N., 1955, *Dokl. Akad. Nauk, S.S.S.R.*, **100**, 875 or AERE Lib/Trans. 602.
- LECLAIRE, A. D., 1953, *Acta Met.*, **1**, 438.
- LOMER, W. M., and COTTRELL, A. H., 1955, *Phil. Mag.*, **46**, 711.
- MANINTVELD, J. A., 1954, *Thesis*, Technische Hoge School, Delft.
- MEECHAN, C. J., and BRINKMAN, J. A., 1956, *Phys. Rev.*, **103**, 1193.
- OVERHAUSER, A. W., and GORMAN, R. L., 1956, *Phys. Rev.*, **102**, 676.
- PIERCY, G. R., 1958, Chalk River, Report CRMet-782.
- SEITZ, F., 1940, *Modern Theory of Solids* (New York : McGraw-Hill), p. 111.
- SEITZ, F., and KOEHLER, J. S., 1956, *Solid State Physics*, Vol. 2 (New York : Academic Press).

# Study of Adsorbed Gas Films by Electron Diffraction†

By L. H. GERMER, E. J. SCHEIBNER‡ and C. D. HARTMAN  
Bell Telephone Laboratories, Inc., Murray Hill, New Jersey

[Received September 30, 1959]

## ABSTRACT

Diffraction patterns of low energy electrons produced by a (111) face of a crystal of nickel have been accelerated sufficiently to show on a fluorescent screen, where they can be photographed. Various gases at low controlled pressures have been admitted to a clean surface, and the arrangements of atoms or molecules upon the surface deduced from their diffraction patterns. Molecules of CO are adsorbed at low pressures as monolayers. They form a single two-dimensional crystal having a spacing between molecules double that between surface nickel atoms; these molecules are completely removed from the surface by heating to 175°C. Experiments with nitrogen have produced a polycrystalline monolayer having the same structure as the CO crystal. (Because of low sticking probability adequate experiments to prove that the layer is really nitrogen are difficult and have not yet been satisfactorily completed. A new type of experimental equipment seems to be required which is now being constructed.) Crystal growth in this monolayer is induced by heating to 125°C; heating above 200°C results in transformation into one or the other of two polymorphic forms either of which is more stable than the original structure; heating to 300°C results in melting the monolayer without removing it, the crystalline structure returning upon cooling. Oxygen can be adsorbed in a layer several atoms or molecules thick; this shows no structure until annealed at 125°C after which the structure is that of the most complex of the polymorphic forms assigned to nitrogen; this complex structure is polycrystalline with very small individual crystals; its diffraction pattern is unchanged when the oxygen is reduced to a single monolayer by heating. No diffraction pattern has been obtained from hydrogen, although the presence of hydrogen is proved by rise in pressure when the crystal is subsequently heated.

## § 1. INTRODUCTION

THE arrangement of foreign atoms adsorbed as a single monolayer upon a crystal surface can be determined by the diffraction of very low energy electrons, of the order of 50 v. This has been known for a long time (Davisson and Germer 1927, Germer 1929) and a great deal of work in this field has been carried out by Farnsworth *et al.* (1929 to 1959). Up to the present time all observations of this sort have been obtained by the laborious method of discovering the features of a diffraction pattern by capturing scattered electrons in a Faraday box which is moved about over the entire field of the pattern.

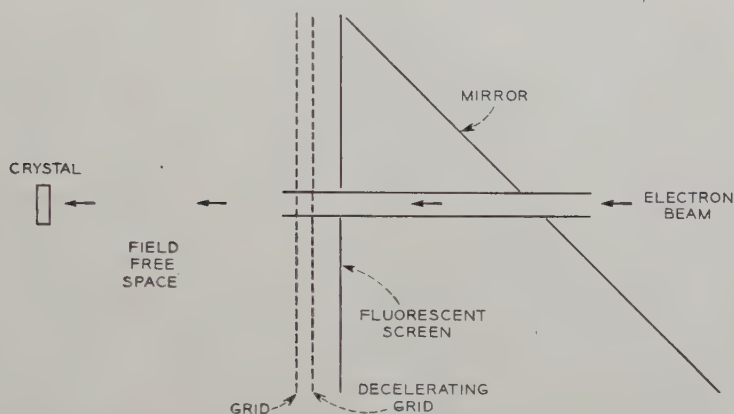
† Communicated by the Authors.

‡ Now at Georgia Institute of Technology, Atlanta, Georgia.

Ehrenberg (1934) showed that diffraction patterns produced by low energy electrons can be accelerated through a considerable potential difference so that the entire pattern can be seen on a fluorescent screen. This represented potentially a very great improvement in the experimental procedure over the earlier method. Nevertheless, Ehrenberg did not develop the technique to a point where it had practical usefulness, and he did not discover patterns due to adsorbed atoms.

We have improved this means of observing a diffraction pattern of low-energy electrons sufficiently to make it a valuable research tool, and by means of it we have determined the arrangements of various kinds of atoms and molecules upon a crystal surface. With this new technique, experiments which were very difficult by the older method are now quite easy, and a vast number of experiments can be carried out which were impossible up to this time (American Crystallographic Association 1959).

Fig. 1



Sketch of the arrangement of the electron diffraction tube, drawn to scale.

Details of the experimental tube will be published elsewhere. For the present purpose, the sketch of fig. 1 will suffice. Electrons emerging from the gun strike the crystal at normal incidence. The diffraction pattern moves in a field free space until it reaches a fine-mesh grid. Between this grid and a second grid is a decelerating field which removes most of the slow electrons. Beyond the second grid the pattern is accelerated by 1000 or 2000 v to a fluorescent screen. The pattern can be observed directly on the screen, or by its reflection in the mirror which is inclined by  $45^\circ$  to the direction of the primary beam. The reflection can be photographed.

The experimental tube of fig. 1 is attached to vacuum pumps and to a Granville-Phillips type vacuum valve through which various gases can be admitted at low controlled pressures. The crystal can be outgassed by electron bombardment and the pressure of residual gas reduced to about  $2 \times 10^{-10}$  mm Hg. Diffraction patterns can be observed when the



surface of the crystal is completely clean and the gradual development of new patterns noted as atoms or molecules of any one of a number of gases settle upon the surface. The observation of these changes is made easy by the fact that the separations of adsorbed gas atoms is greater than the separations of nickel atoms in the surface layer, and, as a consequence of this, diffraction patterns from adsorbed gas atoms are observed in general in a range of voltages lower than the lowest voltages for which the nickel lattice can give any pattern. Thus in most cases there is no superposition of a diffraction pattern from adsorbed gas atoms upon a pattern arising from the nickel crystal and hence no possible confusion.

## § 2. DIFFRACTION PATTERNS FROM A CLEAN CRYSTAL

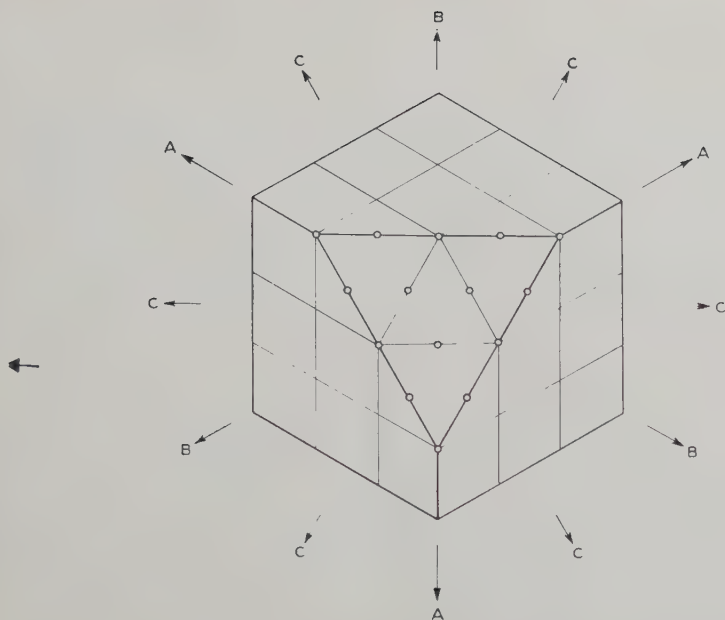
Representative diffraction patterns from a clean (111) face of a nickel crystal are reproduced in fig. 2 (Pl. 26). The first three of these, fig. 2(A), (B) and (C), represent respectively (533), (644) and (466) reflections from the lattice of the crystal, the patterns being taken at the electron beam voltages, 129, 200, and 262, for which the diffraction spots are strongest. Each pattern has threefold symmetry (except for some skewness due to an imperfect electron beam, and the fact that the spot at about 10 o'clock in fig. 2(C) is obscured by the position of the electron gun). In each case the diffraction spots appear in one or the other of the two principal azimuths of the crystal, designated A and B in the sketch of fig. 3. These are the azimuth designations used in earlier experiments (Davisson 1928 a, b, 1929, Germer 1928). The A azimuth has also been called the (111) azimuth, and the B azimuth the (100) azimuth (Davisson and Germer 1927).

In each of these three patterns, weak diffraction spots are seen in the other principal azimuth. This occurs because of the poor resolving power due to limited penetration of the electron beam into the crystal. This effect is shown in exaggerated form in fig. 2(D) in which the diffraction spots appear with equal intensities in the two azimuths: the beam voltage in this case is intermediate between 106 v, at which (244) reflections appear at maximum intensities in the A azimuth, and 129 v, at which (533) reflections appear at maximum intensities in the B azimuth.

For each diffraction pattern the tangent of the angle  $\phi$  between the primary beam and a diffraction beam is obtained by dividing the distance of a diffraction spot from the center of the pattern (measured on such a photograph as those of fig. 2) by 44 mm, the distance from the crystal face to the fine-mesh grid, and multiplying by the photographic enlargement of the pattern. The latter is the ratio of the diameter of the grid measured on the photograph (easily seen on fig. 2(D)) to 67.5 mm, the true diameter of the grid.

The lowest voltage diffraction beams from a clean crystal appear at maximum intensity at 106 v, in the A azimuth. When the voltage of the primary beam,  $V$ , is increased steadily from this value to 400, the limit of our observations, sets of three diffraction beams appear alternatively in the two principal azimuths, each set increasing gradually in intensity to a

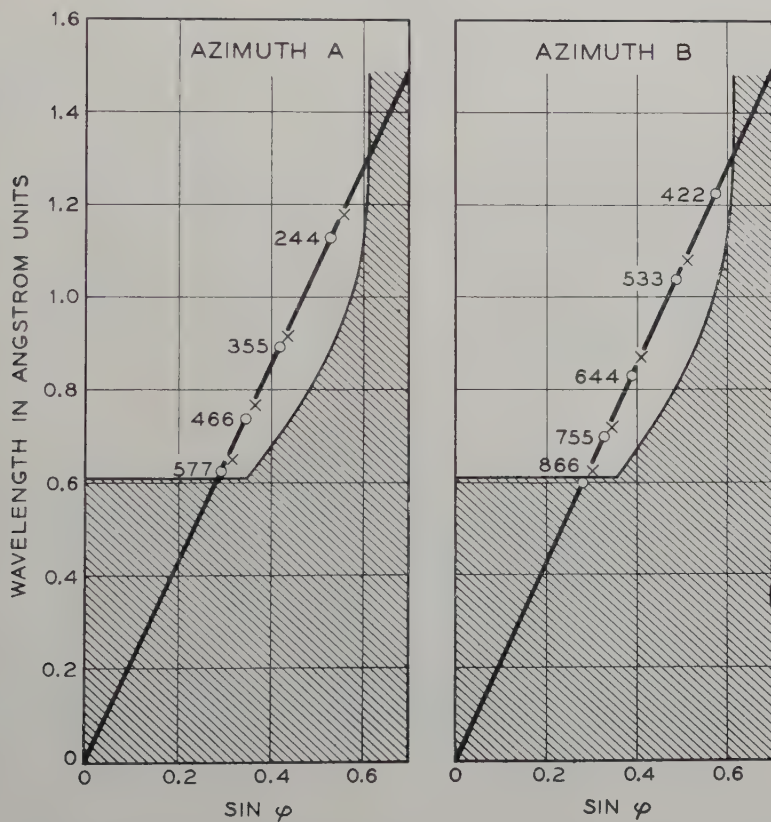
Fig. 3



DESIGNATION OF AZIMUTHS

Sketch showing the designations of azimuths of the crystal. The orientation is the same as that of all of the diffraction patterns reproduced in this paper.

Fig. 4



Plots of all diffraction beams observed from the nickel crystal. Observed diffraction beams plotted as crosses; calculated diffraction beams for zero inner potential plotted as open circles (see table 1). Inaccessible region marked by cross-hatching.

maximum value then decreasing in intensity and disappearing. For each such set of beams the electron wave-length at maximum intensity, calculated from  $\lambda = (150/V)^{1/2}$ , has been plotted in fig. 4 against the sine of the co-latitude angle,  $\phi$ , measured as described above. The observed diffraction beams at maximum intensity are plotted as crosses and the calculated positions of all possible Laue x-ray diffraction beams in this wavelength range are plotted as open circles. The region of the plot which is inaccessible to observation is marked off by cross hatching. The lines in fig. 4 upon which the experimental points fall have a slope of  $2.15 \text{ \AA}$  which is the spacing of lines of surface atoms in the A and B azimuths.

The correct correlation between observed and calculated diffraction beams is quite clear. All possible diffraction beams are found. These are written down in table I, with the potentials at which they are observed at maximum intensity, and the theoretical potentials for zero value of the inner work function. The experimental values of inner potential probably do not differ from the average value of 16 v by more than the possible experimental errors of finding the potential for maximum intensity. Thus the experiments supply no data on variation of inner potential with angle or voltage.

Table 1. Laue Diffraction Beams from a Nickel Crystal (See fig. 4)

Azimuth A				Azimuth B			
Reflec- tion	Voltage		Inner Potential	Reflec- tion	Voltage		Inner Potential
	Obs.	Calc.			Obs.	Calc.	
244	106	119	13	533	129	140	11
355	178	188	10	644	200	215	15
466	262	276	14	755	294	310	16
577	355	383	28	866	403	424	21

Average inner potential 16 v.

### § 3. ADSORBED LAYERS

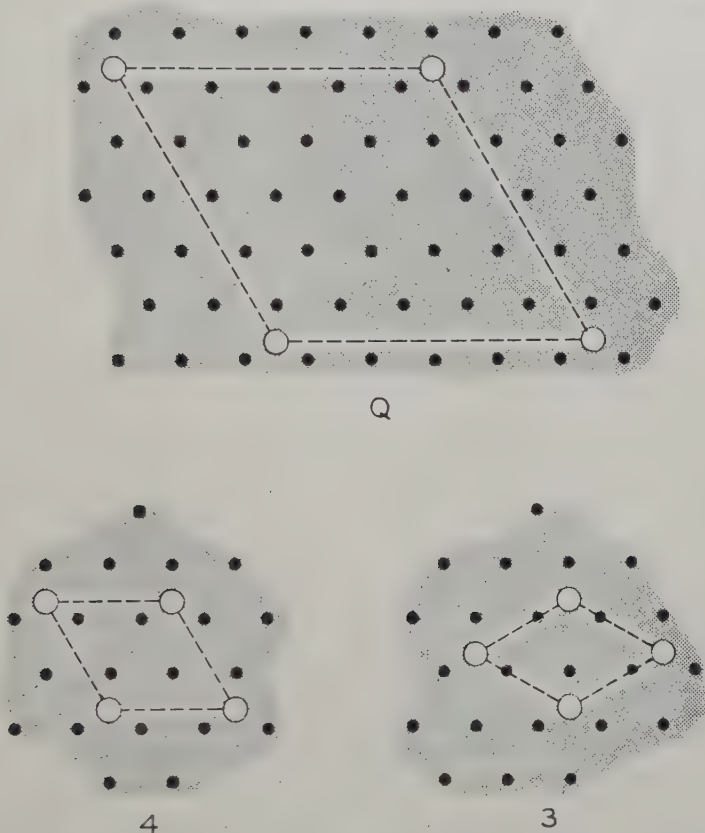
The nickel crystal had received considerable heating before the diffraction patterns of fig. 2 were obtained. A very brief summary of this heating seems to be a necessary prelude to an account of the diffraction patterns obtained from gas films deposited upon a clean surface.

Before the crystal was heated at all, no diffraction pattern could be observed. After heating to only  $500^\circ\text{C}$ , all of the Laue diffraction beams listed above were found, but there were in addition very elaborate patterns at low voltages. An example of one of these patterns is reproduced as fig. 5 (Pl. 28). (The structure giving rise to these complex patterns was



later identified as having the unit cell of the 'Q-structure' which is shown in fig. 6). Low voltage diffraction patterns were entirely eliminated only after the crystal had been heated a number of times at maximum temperatures of  $830^{\circ}\text{C}$ . There were finally no traces of patterns other than the normal Laue beams from the nickel crystal, not even a 'muddy' appearance of an annular region of the fluorescent screen, appearing at low voltages, which was later associated with less than a monolayer of gas on the surface.

Fig. 6



Sketches of the three different arrangements which atoms, which are presumably nitrogen, can take up upon the (111) surface of a nickel crystal. Black dots represent surface nickel atoms, open circles adsorbed atoms. The unit cells of the three different structures are drawn in; in the case of the Q structure, locations of atoms within the unit cell are not known.

### 3.1. Nitrogen on Nickel

Nitrogen was the first gas which was admitted to the experimental tube with the nickel crystal in a condition believed to be clean. Three different types of low voltage diffraction patterns have been observed after the

admission of nitrogen, corresponding to three different arrangements of atoms in a monolayer on the surface. One of these structures is not yet completely understood, although its two-dimensional unit cell is known. Sketches of these structures are shown in fig. 6.

Because of the rather low sticking probability observed in these experiments it has not been established with certainty that the adsorbed gas is nitrogen rather than an impurity gas present in small amount but having sticking probability close to unity. This uncertainty is aggravated by uncontrolled fluctuations of pressure incidental to the method of cleaning the crystal at high temperatures. The bombarding tungsten ribbon adsorbs gas readily, and the release of this gas whenever the ribbon is heated raises the pressure to undesirably high values. A nickel crystal which can be heated by conduction will reduce this difficulty, and this seems to be essential for better control of gas pressure.

In all of the following experiments with nitrogen the adsorbed gas will be spoken of as nitrogen, which we now doubt. Presumptive evidence that it is atomic rather than molecular is furnished by the low sticking probability and by the fact that it is not removed until crystal temperatures above 400°C are reached.

In the sketches of fig. 6 the black dots represent the centers of nickel atoms lying in the surface layer, and the open circles the positions of adsorbed nitrogen atoms. In the structure marked 4 the separations between adjacent nitrogen atoms is double that between nickel atoms in the surface layer; the ratio of the number of nickel atoms to the number of nitrogen atoms is 4, which number has been chosen to designate the structure. In the structure marked 3 the corresponding ratio of distances is  $3^{1/2}$ , and the ratio of the numbers of atoms is 3.

The structure marked Q is much more complex with a two-dimensional hexagonal unit cell having an edge of 12.4 Å, five times larger than the separation of adjacent nickel atoms. The relative intensities of different diffraction spots of a pattern representing the Q structure are not the same in different experiments. For example, the (22) and (33) reflections are sometimes strong and sometimes weak. This seems to mean that the locations of atoms within the unit cell of this structure is not always the same. Furthermore, there is, in general, no single arrangement in the different unit cells which can account for the observed intensities, which is interpreted to mean that the arrangement is not the same in all the unit cells.

In all three of these structures it has been assumed that adsorbed atoms are located between surface nickel atoms as indicated, although the diffraction patterns do not establish this fact. As the sketches of fig. 6 are reproduced here, there is no distinction between the centres of small triangles of nickel atoms having their apices up and down. If we identify azimuths in fig. 6 with those marked on fig. 3 (and with the approximate orientation of the diffraction patterns of fig. 2(A), (B) and (C), then the placing of atoms at the centres of triangles with apices upward (as is done)

is equivalent to placing them above nickel atoms of the second layer below the surface rather than above atoms only one layer below. There is some experimental evidence that this is the correct placement.

Representative diffraction patterns from which the 4, 3 and Q structures have been deduced are reproduced respectively in figs. 7, 8 and 9 (Pls. 27-29). Data relating to the patterns representing the 4 and 3 structures are assembled in table 2, and data relating to the patterns from the Q structure in table 3.

The experimental conditions under which atoms take up these different arrangements on the crystal surface are imperfectly understood, and the clarification must wait upon further work. The observations which are now available are summarized below, together with the difficulties encountered in understanding the factors involved.

Table 2. Patterns Representing the 4 and 3 Structures

(1)	(2)	(3)	(4)	(5)	(6)	(7)	(8)
	Voltage and wave length	Range of Observ- able spacings	Calculated beams within this range			Observed beams	
			Miller indices	Spacing	Azimuth	Spacing	Azimuth
The 4—structure							
Fig. 7(A)	52 v 1.69 Å	From 6.8 Å to 2.9 Å	(10)	4.30 Å	A, B	4.30 Å	A, B
Fig. 7(B)	57 v 1.615 Å	From 6.5 Å to 7 Å	(10)	4.30 Å	A, B	4.45 Å	A strong B weak
Fig. 7(C)	65 v 1.52 Å	From 6.1 Å to 2.6 Å	(10)	4.30 Å	A, B	4.21 Å	B strong A weak
Fig. 7(D)	77 v 1.40 Å	From 5.7 Å to 2.4 Å	(10) (11)	4.30 Å 2.48 Å	A, B C	4.51 Å 2.46 Å	A, B C
The 3—structure							
Fig. 8	62 v 1.555 Å	From 6.3 Å to 2.6 Å	(10)	3.72 Å	C	3.76 Å	C

The 4 structure seems to be favoured by deposition at very low pressure upon a crystal at room temperature. At an appropriate electron beam voltage, the pattern representing this structure makes its appearance on the fluorescent screen rather gradually. The diffraction spots are initially very diffuse, presumably representing simultaneous nucleation of individual two-dimensional crystallites at many different points on the surface. The two-dimensional layer of atoms is then polycrystalline, however with almost certainly all of the crystals similarly oriented and representing only



lateral displacements with respect to each other without rotation. There can be only four, or possibly eight, different kinds of crystallites. Since all of these two-dimensional crystallites are simply related to the structure of the underlying nickel, and therefore to each other, it is not at present clear why they do not conspire to give a sharp pattern.

Table 3. Patterns Representing the Q Structure

(1)	(2) Voltage and wave-length	(3) Range of observable spacings	(4) (5) (6) Calculated beams within this range			(7) (8) Observed beams	
			Miller indices	Spacing	Azimuth†	Spacing	Azimuth†
Fig. 9(A)	48 v 1.75 Å	6 Å  3.5 Å	(20) (21) (30)	5.37 Å 4.06 Å 3.59 Å	A, B 19° A, B	5.32 Å	A and B
Fig. 9(B)	75 v 1.415 Å	5.8 Å  2.7 Å	(20) (21) (30) (22) (31)	5.37 Å 4.06 Å 3.59 Å 3.10 Å 2.99 Å	A, B 19° A, B C 14°	Just detectable Just detectable 3.58 Å 3.10 Å not seen	A, B weak C strong
Fig. 9(D)	120 v 1.12 Å		(10) (11) (20) (21) (30) (22) (31) (40) (32) (41) (50) (33) (42) (51) (60) (43) (52)	10.75 Å 6.22 Å 5.37 Å 4.06 Å 3.59 Å 3.10 Å 2.99 Å 2.69 Å 2.47 Å 2.35 Å 2.15 Å 2.07 Å 2.03 Å 1.93 Å 1.79 Å 1.77 Å 1.72 Å	A, B C A, B 19° A, B C 14° A, B 23° 11° A, B C 20° 9° A, B 25° 16°	† † 5.59 Å  3.70 Å 3.15 Å  2.71 Å 2.47 Å 2.35 Å 2.15 Å 2.08 Å 2.05 Å 1.94 Å 1.82 Å 1.81 Å 1.77 Å	A, B  A, B C  A, B 23° 11° A, B C 20° 8° A, B 25° 16°

† Azimuths other than that A, B and C are designated by the angle which they make with the A and B azimuths.

‡ It should be pointed out that there are other diffraction patterns from the Q structure taken at 10 v and at 15 v (not reproduced here), which show the (10) and (11) reflections unmistakably and very strongly.

With the crystal at room temperature, this type of structure seems to last indefinitely. If the crystal is warmed to 100°C above room temperature the diffraction spots become considerably sharper, presumably corresponding to crystal growth. The spots can, however, never be made as sharp as one would expect them to be for the entire surface arranged in a single two-dimensional array. The patterns of fig. 7 are of intermediate sharpness.

At a temperature  $225^{\circ}\text{C}$  the patterns due to adsorbed gas atoms are very weak, and at slightly higher temperatures entirely missing, although the Laue spots from the nickel crystal are not greatly changed. This change with temperature seems to be due to melting the two-dimensional crystal of atoms so that they move about freely over the surface. A pattern reappears at once on allowing the crystal to cool. The pattern which appears after cooling is, however, never the 4 pattern. If the heating has been quite moderate,  $225^{\circ}\text{C}$ , the new arrangement is that of the Q structure. If the heating has been more severe, at temperatures which may be as high as  $400^{\circ}\text{C}$ , the pattern may be the Q or the 3. There seems to be no heat treatment which can produce the reverse change, from the Q or 3 pattern back to the 4. Thus the arrangement of atoms represented by the 4 pattern seems to be the least stable of the three arrangements.

Whether the spots of a Q type diffraction pattern are fuzzy, as in fig. 9(C), or sharp, as in fig. 9(D), is determined by the temperature to which the crystal has been raised after deposition of the gas. Maximum temperatures of the order of  $225^{\circ}\text{C}$  lead to patterns with diffuse spots (like fig. 9(C)), but sharp spots are found after heating at  $300^{\circ}\text{C}$  or  $400^{\circ}\text{C}$ .

Understanding the factors which determine the structure of adsorbed atoms is made difficult by inadequate independent control of temperature and gas pressure. The nickel crystal is heated by electron bombardment from a tungsten ribbon. Whenever this ribbon is heated the gas pressure rises (often by a factor greater than 10) because of the adsorbed nitrogen which it gives up, and whenever the ribbon is cooled there is a decrease of pressure (often by a factor of 10). A thin nickel crystal, which can be heated by conduction, is now being prepared. We expect that the factors which determine the different structures of adsorbed atoms can be found out from experiments with this crystal.

### 3.2. CO on Nickel

Carbon monoxide molecules arrange themselves on the surface of the nickel crystal in the 4-structure. Except for this one point the behaviours of carbon monoxide and nitrogen are, however, quite different. The probability that a CO molecule which strikes the surface will stick to it is very high. Yet the CO is held very weakly, and molecules of CO are completely removed by heating the crystal to only  $175^{\circ}\text{C}$ . Other differences in the behaviour of the two gases are the absence of polymorphic forms of two-dimensional CO crystals, and the greater tendency of CO molecules to arrange themselves in an almost perfect two-dimensional array, rather than imperfectly. A typical pattern from a monolayer of CO molecules is reproduced as fig. 10 (Pl. 30).

At an appropriate electron beam voltage and a suitably low CO pressure, the gradual development of a diffraction pattern can be observed quite clearly. An annular ring of nebulous character shows up first on the fluorescent screen. This ring seems at first circular, then assumes an angular appearance which soon can be identified as hexagonal. Finally,

the sides of the ring clear up and only six diffraction spots are left. Initially the spots are diffuse, but they rapidly become quite sharp. In the case of nitrogen, the development of a diffraction pattern is less easily followed.

The sticking probability measurements for CO, which are very crude, were made by observing the time required for the 4 pattern to appear at maximum intensity and sharpness upon the fluorescent screen immediately after the crystal had cooled from high temperature. A simultaneous record was made of the CO pressure, which was necessarily always changing rapidly. In a number of tests, values of the integrated product of the pressure and the time were found in the range  $0.4$  to  $6 \times 10^{-6}$  mm Hg sec. The theoretical value for CO molecules striking the surface at  $300^\circ\text{K}$  and forming a complete monolayer with the 4 arrangement is  $1.3 \times 10^{-6}$  mm Hg sec for sticking probability unity. Although the observations were extremely crude, they do prove that the sticking probability is very high and of the order of unity. They indicate also that CO molecules are fairly free to move about over the surface at room temperature.

The diffraction patterns from monolayers of CO molecules were always quite sharp and no change of sharpness was produced by warming the crystal after deposition or by deposition upon a warm crystal. There was, however, no deposition of CO upon the crystal at temperatures in excess of  $150^\circ\text{C}$ , and this temperature was just high enough to clean the surface completely.

In a series of interesting experiments, CO was deposited first upon a clean crystal surface, then the surface layer was removed by heating to  $175^\circ\text{C}$  after which a new layer of CO molecules was deposited. It was found that after two of these cycles the surface could be only partially cleaned at this low temperature, and the situation became worse after another cycle. The obvious conclusion from these tests is that we were observing the effects of impurities in the CO (from residual gas in the tube), which could not be removed at  $175^\circ\text{C}$ . Behaviour was normal again after the crystal had been heated above  $800^\circ\text{C}$ .

In some experiments the Q structure was observed, but this was only after the crystal had been exposed over night to CO at an exceptionally high pressure ( $2 \times 10^{-8}$  mm Hg as an average value). It seems altogether probable that this structure was due not at all to CO but to impurities.

### 3.3. *Oxygen on Nickel*

The behaviour of oxygen is very different from that of nitrogen or CO. Exposure of the clean crystal surface to oxygen results in gradual weakening and final disappearance of Laue beams from the nickel, without the appearance of any new diffraction beams at low voltages. When a crystal which shows no diffraction patterns of any sort, after for example having been exposed to oxygen at the comparatively high pressure of  $5 \times 10^{-8}$  mm Hg for 16 hours, is heated to progressively higher temperatures, the following series of changes can be observed.



After heating at 200°C, diffuse low voltage beams can be seen (fig. 11(A) Pl. 30) but the amount of oxygen on the surface is still so great that no Laue beams from the nickel are seen up to the limit of the observations at 400 v. Some sharpening of the oxygen diffraction pattern can be produced by further heating (fig. 11(B)), still without removing enough of the oxygen to permit the appearance of diffraction patterns from the nickel. More vigorous heating (probably† above 500°C) results in re-appearance of the nickel diffraction beams at apparently full intensity, *but with no change in the oxygen diffraction pattern* which is now almost certainly the pattern from a single monolayer. Finally the diffraction pattern from the oxygen is destroyed by heating at a bright cherry red.

The two dimensional spacings corresponding to the spots of fig. 11 are written down in table 4. The spots can be indexed as (22) and (40) reflections of the Q structure (see table 3). We do not understand how a thick layer of annealed oxygen can give the same type of Q pattern which is produced by a single monolayer.

Table 4. Patterns from Oxygen on Nickel

	Voltage and wave-length	Observed Beams		Miller indices (see table 3)
		Spacing	Azimuth	
Fig. 11(A)	82 v 1.35 Å	2.66 Å	A, B	(40)
Fig. 11(B)	82 v	3.17 Å	C	(22)
	1.35 Å	2.66 Å	A, B	(40)

### 3.4. Hydrogen on Nickel

No evidence has been obtained of any diffraction pattern due to hydrogen. In one test hydrogen flowed through the experimental tube for 65 hours at an average pressure of  $2 \times 10^{-7}$  mm Hg. At the end of this time no low voltage diffraction features could be found; the Laue beams from the nickel lattice seemed to be even stronger than they were initially; and there was a considerable improvement in the apparent resolving power of the crystal, shown by each Laue beam being observable over a narrower range of wavelengths. It was shown, by observing a rise in pressure when the crystal was heated, that there was considerable adsorbed hydrogen.

It seems altogether possible that hydrogen atoms or molecules may be as close together on the surface as are surface nickel atoms, and with the same lateral arrangement. If this were true, their presence would result only in modification of the intensities of diffraction beams attributed to the lattice of the crystal. The improved resolving power of the crystal remains to be explained.

† The thermocouple attached to the crystal was out of order when this test was carried out.

## § 4. DISCUSSION

Many observations of relative intensities of diffraction beams from adsorbed gas layers require clarification. Most of this will have to await further work.

Perhaps the simplest of these observations upon relative intensities is shown in the patterns of fig. 7. One notes that diffraction patterns representing the 4 structure are strong at some voltages in the A azimuth and at other voltages in the B azimuth. "It will be noticed that the nickel atoms in the surface are of two sorts—those that are adjacent to gas atoms and those that are not. One-fourth of the nickel atoms are of this latter class, and they together form a layer of the same structure, orientation and scale factor as the gas atoms. If the two classes of nickel atoms scatter radiation in different amounts—if, for example, the gas atoms shield the adjacent nickel atoms more effectively than the non-adjacent—then, of course, the layer of nickel atoms as a whole will give rise to a differential diffraction beam capable of interference with that due to the gas layer."† This accounts for the variation of intensity with azimuth, and its change with voltage. In principle, one can work out from it the distance between the adsorbed nitrogen atoms and the surface nickel atoms. The electron wavelength is, however, too short to give any respectable precision to such a calculation. The data are consistent with a separation of 3 Å which is a reasonable value.

It has already been pointed out that in different experiments, which have led to atoms arranged on the surface in the Q structure, relative intensities of diffraction spots have been widely different. This has been interpreted to mean that there are a number of different possible arrangements of atoms within the large two-dimensional hexagonal unit cell ( $a_0 = 12.4 \text{ Å}$ ) of the Q structure. And even one single diffraction pattern must be interpreted to arise from a structure in which there are different arrangements within the unit cell on different parts of the effective surface. It is hoped and expected that the distributions of arrangements giving rise to particular patterns can be found out.

In each diffraction pattern from a monolayer of adsorbed atoms or molecules, of whatever sort, it has been observed in general that the pattern appears most strongly at some particular electron wavelength. A single diffraction spot of the pattern can always be traced over a range of electron wavelengths, satisfying always the appropriate plane grating formula, but its intensity varies greatly. Such variation is not consistent with a pattern produced by a single atomically flat plane of atoms. The probable interpretation of this variation, which has not yet received theoretical quantitative confirmation, is that the variation is due to atomic steps on the surface within a distance appropriate to the wave-front of an electron. One single step, for example, would result in diffraction from two monolayers of atoms with a spacing of 2.03 Å (the separation of (111) planes

---

† The quotation is from Davisson and Germer (1927).

of nickel atoms). This interpretation should be amenable to easy confirmation.

That this interpretation is correct is suggested by the experimentally observed fact that quite flat crystal surfaces are required for the observation of any diffraction patterns from adsorbed monolayers. In earlier experiments, before the use of the present nickel crystal, tests were carried out upon a tungsten single crystal. Excellent Laue diffraction beams were obtained from this crystal. Single monolayers of adsorbed gas atoms were deposited upon its surface by well-known techniques, but in no case could any diffraction pattern at all be obtained from one of these monolayers. Tungsten crystals, of the type used in these experiments, are known to be notoriously rough. It is now believed that this was the cause of the failure of the tungsten experiments. It seems probable that the method of investigation outlined in this paper will be applicable only to selected crystal surfaces which can be made exceptionally flat on an atomic scale.

The remarkable anomalous improvement in the resolving power of the nickel crystal, which is produced by hydrogen, is not understood. Is it possible that this improvement is the result of a change to normal spacing of an abnormal spacing between the first and second layers of nickel atoms? Accurate intensity measurements are required to settle this question.

### § 5. NEW EXPERIMENTS

A number of continuations of the present experiments immediately suggest themselves:

1. The most pressing of these is the certain identification of the gas giving rise to the patterns assigned to nitrogen. This will require a nickel crystal which can be heated by conduction in order to avoid the fluctuations in pressure taking place on heating and cooling the tungsten ribbon used in bombarding the crystal.

2. Such a crystal, which can be heated by conduction, should be valuable in other experiments also; for example, in understanding the factors which determine the transitions between the crystalline forms of the 4, Q and 3 structures, and by the flash filament technique in finding just when we have a monolayer of adsorbed atoms in those cases in which it is now uncertain, and finally in determining unambiguously whether a gas is adsorbed as atoms or molecules.

3. Repetition of some of these tests upon a (100) face of a nickel crystal. This would seem to require preparation of an unusual surface without (111) facets. Present electropolishing techniques offer promise that a satisfactory (100) surface can be obtained.

4. Tests of the reaction of one gas with another upon a crystal surface. For example, will gas atoms (presumed to be nitrogen) adsorbed upon a nickel surface in the unstable 4 structure react more readily with hydrogen than will atoms in the other two more stable arrangements? Experiments of this sort require a considerable battery of valves with appropriate auxiliary pumps and gas bulbs. These are now being installed.



5. Studies of surface states of silicon crystals. The (111) surface of silicon can be made remarkably smooth on an atomic scale, and such surfaces should be very favourable also for studies of adsorption and catalytic reaction.

## REFERENCES

- American Crystallographic Association—Program and Abstracts, Annual Meeting July 19–24, 1959.  
DAVISSON, C. J., 1928 a, *Bell Syst. tech. J.*, **7**, 90 ; 1928 b, *J. Franklin Inst.*, **205**, 597 ; 1929, *Sci. Monthly*, **28**, 41.  
DAVISSON, C. J., and GERMER, L. H., 1927, *Phys. Rev.*, **30**, 705.  
EHRENBERG, W., 1934, *Phil. Mag.*, **18**, 878.  
FARNSWORTH, H. E. *et al.*, 1929, *Nature, Lond.*, **123**, 941 to 1959, *J. appl. Phys.*, **30**, 675. Many papers.  
GERMER, L. H., 1928, *J. chem. Educ.*, **5**, 1041 ; 1929, *Z. Phys.*, **54**, 408.

# The Hardening of Lithium Fluoride by Electron Irradiation†

By A. D. WHAPHAM and M. J. MAKIN

Metallurgy Division, Atomic Energy Research Establishment,  
Harwell

[Received October 1, 1959]

## ABSTRACT

A study has been made of the effect of 1 mev electron irradiation on the mechanical properties of lithium fluoride single crystals tested in compression. The yield point,  $\sigma$ , has been shown to vary with the irradiation dose,  $\phi$ , according to the law  $\sigma = \sigma_u + A[1 - \exp(-B\phi)]^{1/2}$ , where  $\sigma_u$ ,  $A$  and  $B$  are constants. This relationship has been derived theoretically by considering the passage of dislocations through radiation induced obstacles dispersed in the slip plane, together with the capture of point defects by existing obstacles. The empirical relationship  $\sigma = k\phi^{1/3}$ , previously used for radiation hardening in metals, is capable of representing only the medium dose results, but clearly does not fit at either low or high doses.

A new mechanism of cracking in heavily irradiated lithium fluoride, similar to that proposed by Cottrell for alpha iron, has been observed. With compression along a [001] axis, cracks are initiated at the intersections of orthogonal {110} type slip planes and extend on the (100) cleavage plane passing through the intersection and parallel to the compression axis.

## § 1. INTRODUCTION

Two types of irradiation hardening are theoretically possible in crystalline solids which normally deform by a slip process. Either (a) the nucleation of slip may be made more difficult by making dislocation sources harder to operate (source hardening), or (b) the stress for the propagation of slip may be increased (lattice hardening) by an increase in the stress required to move dislocations through the crystal. In well-annealed metals such as copper and nickel both types of hardening occur after neutron irradiation. In lithium fluoride the existence of lattice hardening after electron irradiation has been proved by observing the dislocation patterns (revealed by etching) produced by hardness indentations (Whapham 1958). In unirradiated material dislocations glide appreciable distances away from the indentation whereas after irradiation dislocations can be seen only in the immediate vicinity of the indentation, the irradiation induced lattice hardening preventing these dislocations from moving away.

Work preliminary to the present investigation has shown that it is the stress necessary to move dislocations that governs the plastic deformation of lithium fluoride. The mechanism of deformation of stressed crystals was investigated by etching to reveal the slip dislocations. It

---

†Communicated by the Author.

was found that in all specimens, both unirradiated and electron-irradiated, individual slip planes extended from their point of origin slowly, with progressive increase of stress. If the operation of dislocation sources determined the stress at which plastic deformation occurred then complete slip lines would be expected to form abruptly. This work also showed that dislocations in the compression specimens move at stresses well below the macroscopic yield stress at normal strain rates. In unirradiated material dislocation movement is first seen at a resolved shear stress of  $0.13 \text{ kg/mm}^2$ , whereas the macroscopic yield occurs at a shear stress of  $0.5 \text{ kg/mm}^2$  when the applied strain rate is  $10^{-4}$  per sec. In the electron-irradiated material, dislocation movement also starts at stresses roughly  $0.4 \text{ kg/mm}^2$  less than the value at the macroscopic yield.

Gilman and Johnston, who have measured the yield stress of lithium fluoride during bend tests (Gilman and Johnston 1956, 1958), and the stress dependence of dislocation velocity as a function of neutron irradiation (Johnston and Gilman 1958), concluded that the irradiation hardening is governed by the resistance to motion of dislocations through the crystal lattice. In addition the form of the stress-strain curve can be explained in terms of the variation of dislocation velocity with stress and the multiplication of dislocations. It is therefore apparent that the yield point at a given strain rate is a measure of the lattice hardening. No direct measurement of an increase in stress required to operate dislocation sources in lithium fluoride has yet been made.

The present experiments were undertaken to determine in detail the dependence of the lattice hardening on the irradiation dose, and to compare this with a theoretically predicted relationship.

### 1.1. *Dependence of Lattice Hardening on Irradiation Dose*

Lattice hardening must be caused by 'obstacles' of some kind distributed throughout the crystal lattice which oppose the motion of dislocations across the glide plane. It is not necessary to specify at this stage the nature of these obstacles except to point out that they are unlikely to be individual point defects during room temperature irradiation in view of the low temperatures at which these become mobile in most crystalline materials. It is more probable that each obstacle is a cluster or aggregate of defects of some kind.

If  $N$  is the number of dislocations per unit volume held up against  $N_z$  obstacles per unit area of glide plane then the strain rate  $\dot{\epsilon}$  at a temperature  $T$  and stress  $\sigma$  is given by

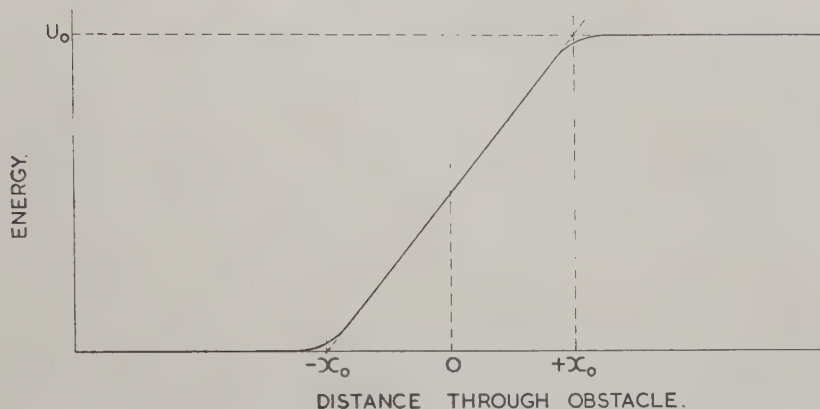
$$\dot{\epsilon} = \frac{N\mathbf{b}\nu_0}{N_z} \exp\left(-\frac{U(\sigma)}{kT}\right), \quad \dots \dots \dots (1)$$

where  $U$  is the activation energy for cutting through the obstacles,  $\mathbf{b}$  is the Burgers vector and  $\nu_0$  the frequency with which a dislocation line attempts to pass the obstacle. Solving eqn. (1) for  $\sigma$  gives the lattice hardening stress as a function of  $N_z$ . To do this is first necessary to



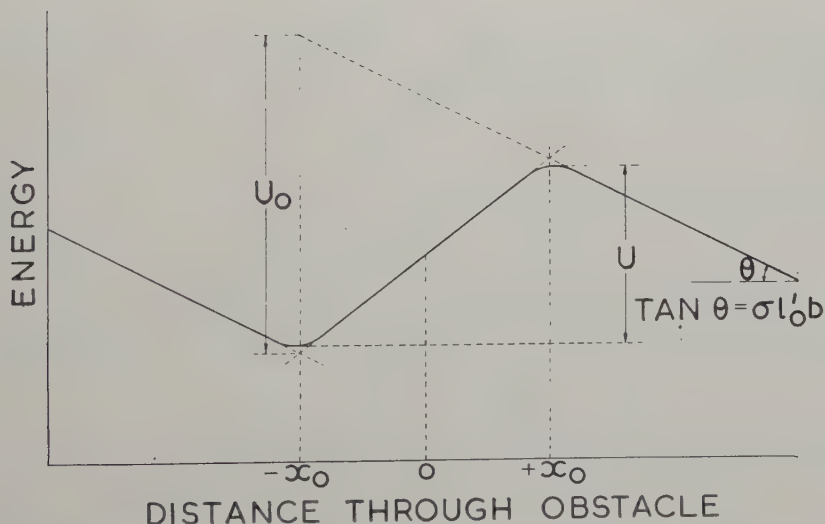
determine the stress dependence of the function  $U(\sigma)$ . Various equations can be chosen to represent the energy profile of the obstacle which is expected to be as shown in fig. 1. Application of stress to the crystal modifies the shape of the potential energy-distance curve as in fig. 2 by introducing a variation in potential energy with distance of  $\sigma l_0' b$  where  $l_0'$  is the average distance between obstacles in the slip plane. Mott and

Fig. 1



Energy profile of a dislocation cutting through an obstacle at zero externally applied stress.

Fig. 2



Energy profile of a dislocation cutting through an obstacle when an external stress  $\sigma$  is applied.

Nabarro (1948) and also Seeger (1958) have shown that a good approximation to the new value of  $U$  is given by

$$U = U_0 \left( 1 - \frac{\sigma}{\sigma_0} \right)^{3/2},$$

where  $U_0$  is the activation energy at zero stress and  $\sigma_0$  is the stress required to overcome the barrier without thermal activation.

When  $U = 0$ ,

$$\sigma_0 l_0' \mathbf{b} = \frac{U_0}{2x_0}$$

and hence

$$U = U_0 \left( 1 - \frac{2x_0 \mathbf{b} l_0' \sigma}{U_0} \right)^{3/2}. \quad (2)$$

Seeger derives an almost identical expression for  $U$  except for the constant 4 instead of 2.

In the simplest case, where no allowance is made for a stress dependence of  $l_0'$

$$l_0' = \frac{1}{N_z^{1/2}}$$

and

$$U = U_0 \left( 1 - \frac{2x_0 \mathbf{b} \sigma}{U_0 N_z^{1/2}} \right)^{3/2}.$$

Substituting for  $U$  in eqn. (1)

$$\sigma = N_z^{1/2} \frac{U_0}{2x_0 \mathbf{b}} \left[ 1 - \left\{ \frac{kT}{U_0} \ln \left( \frac{N \mathbf{b} v_0}{N_z \dot{\epsilon}} \right) \right\}^{2/3} \right]$$

is obtained and if  $N_z$  is proportional to the irradiation dose,  $\phi$ , initially,

$$\sigma \propto \phi^{1/2}.$$

Friedel (1956) has suggested that  $l_0'$  should decrease with increasing stress due to the greater probability of a dislocation bowing out sufficiently to meet another obstacle at high stresses. Friedel calculates that

$$(l_0')^3 = \frac{G \mathbf{b}}{\sigma N_z}.$$

Inserting this into eqn. (2), we obtain

$$U = U_0 \left[ 1 - \frac{2x_0 \mathbf{b}^{4/3} G^{1/3} \sigma^{2/3}}{U_0 N_z^{1/3}} \right]^{3/2}.$$

Substituting this modified expression for  $U$  into eqn. 1, the expression for  $\sigma$  becomes

$$\sigma = \left[ \frac{N_z}{G \mathbf{b}} \right]^{1/2} \left[ \frac{U_0}{2x_0 \mathbf{b}} \right]^{3/2} \left[ 1 - \left\{ \frac{kT}{U_0} \ln \left( \frac{N \mathbf{b} v_0}{N_z \dot{\epsilon}} \right) \right\}^{2/3} \right]^{3/2}.$$

In this expression also

$$\sigma \propto N_z^{1/2}.$$

In both cases therefore dislocation theory predicts a dependence of lattice hardening on  $N_z^{1/2}$ .

Initially the number of obstacles  $N_z$  is expected to be proportional to the irradiation dose  $\phi$  but, as the concentration of obstacles increases, there is an increasing probability that new defects will be captured by existing obstacles rather than nucleating new ones. Hence the number of new obstacles formed during a given increment of dose decreases as the dose increases. If there is a volume  $v$  associated with each obstacle within which capture will occur, then the rate at which new obstacles are formed  $\dot{N}_z$ , can be written

$$\dot{N}_z = a\dot{\phi}(1 - vN_z),$$

where  $a$  is the number of obstacles produced per electron and  $\dot{\phi}$  is the dose rate. Integrating, the number of obstacles  $N_z$  is given by

$$N_z = \frac{1}{v} [1 - \exp(-av\phi)]$$

and hence the lattice hardening is given by

$$\sigma_i \propto \frac{1}{v^{1/2}} [1 - \exp(-av\phi)]^{1/2}$$

$$\text{or} \quad \sigma_i = A[1 - \exp(-B\phi)]^{1/2}. \quad . \quad . \quad . \quad . \quad . \quad (3)$$

This formula predicts that initially the lattice hardening  $\sigma_i$  will be proportional to  $\phi^{1/2}$  and that at large doses  $\sigma_i$  will saturate at a constant value  $A$ . The relationship does not depend upon the properties of any particular material and is intended to apply generally to crystalline solids which deform by slip.

The alternative relationship which has been fitted to the hardening of copper single crystals by neutron irradiation (Blewitt 1956) is that

$$\sigma_i \propto \phi^{1/3}.$$

This relationship has no sound basis in dislocation theory and is purely an empirical one which happens to fit the experimental data over the range of doses used. The importance of deciding between these two expressions is of considerable technological as well as fundamental interest since the  $\phi^{1/3}$  relationship predicts a continually increasing hardening with neutron exposure instead of the saturation expected in the new theory. In metals very high neutron doses are required to decide between the two theories since at low doses by a suitable choice of constants the two relations are very similar. In lithium fluoride damaged by electron irradiation however, only comparatively short irradiation times are required to introduce enough damage to decide which relationship is more correct.

## § 2. EXPERIMENTAL

Specimens,  $2.4 \times 2.4 \times 20$  mm in size and bounded by (100) cleavage surfaces, were cleaved from two single crystal blocks  $1\frac{1}{2}$  in.  $\times$   $1\frac{1}{2}$  in.  $\times$   $\frac{1}{2}$  in. selected from a batch of material supplied by the Harshaw Chemical Company. The cleaved specimens contain fresh surface dislocations caused by the cleavage process and dust scratches, together with about  $10^5$



aged dislocations per  $\text{cm}^2$ . Roughly half the aged dislocations are contained in low-angle boundaries and half are randomly distributed through the crystal. The two crystal blocks used in this work were of similar purity and had been subjected to similar thermal treatment and the yield stresses, which are very sensitive to these factors, were practically identical ( $0.498 \pm 0.010$  and  $0.493 \pm 0.010 \text{ kg mm}^2$  respectively).

The specimens were irradiated, three at a time, in a beam of 1 Mev electrons produced by a Van de Graaff generator. As the penetration of the electron beam in lithium fluoride is only 1.2 mm and specimens thicker than this were required in order to perform satisfactory tests, the 2.4 mm thick specimens were irradiated firstly on one face and then turned round to irradiate the opposite face. Using this technique the radiation dose was fairly uniform throughout the crystal, as shown by optical absorption, and consistent results were obtained with them. Crystals thicker than those used show a light band in the centre, where the irradiated regions do not overlap and thinner ones show enhanced absorption in the centre.

The maximum dose used was  $10^{16}$  electrons/ $\text{cm}^2$  since, above this dose cracking, produced by radiation-expansion of the lattice, was encountered. It is unlikely that strains present in specimens which had not cracked could affect the yield point since most of the stress-strain curves showed an easy glide region of  $1\frac{1}{2}\%$  even at the highest doses used. This deformation should eliminate any non-homogeneous strain present.

Care was taken to ensure that the temperature rise during irradiation was not excessive. Variation of the beam current below the maximum of  $0.54 \mu\text{A}/\text{cm}^2$  did not have any observable effect in subsequent testing. Theoretically it is estimated that the maximum temperature rise was about  $10^\circ\text{C}$ .

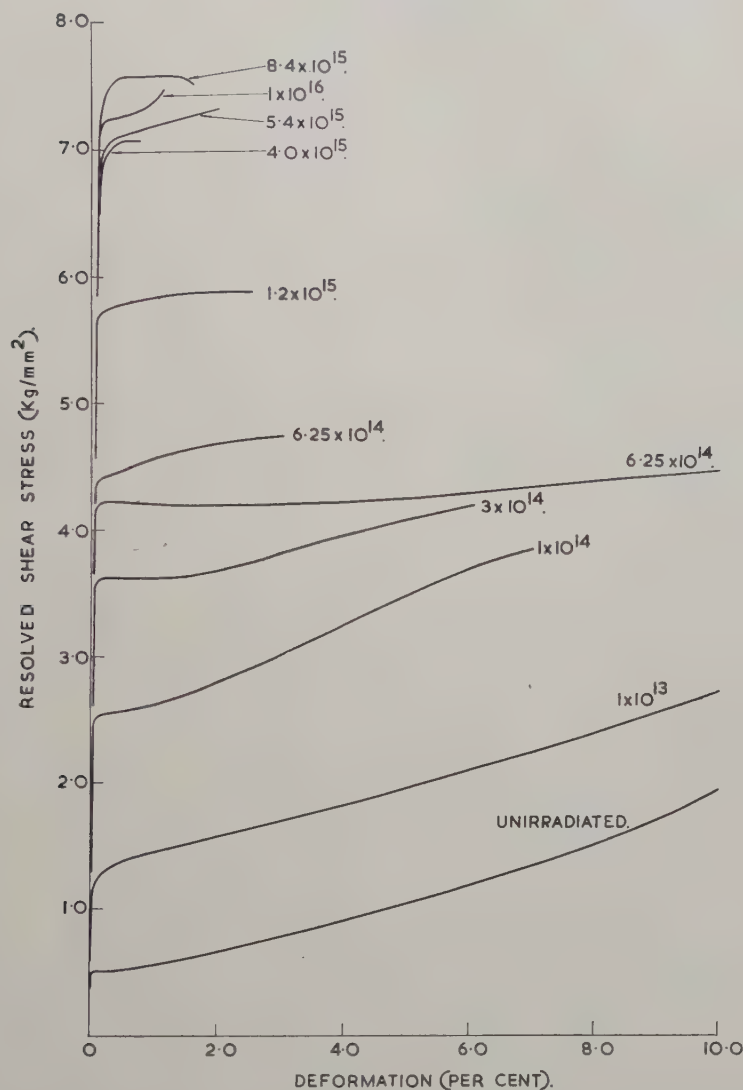
After irradiation, steel end pieces and two brass cross pieces, 10 mm apart, were fitted to the specimens, using a synthetic resin adhesive. Mounted in this way they were placed in a special compression jig designed to produce axial loading and tested at a strain rate of  $10^{-4}$  sec. The strain of the 10 mm central section of the specimens was measured by a capacitative strain measuring head attached to the two brass cross pieces. With this arrangement strains from  $0.01\%$  to  $10\%$  could be measured.

Representative stress-strain curves are shown in fig. 3. The unirradiated crystal yields at  $0.496 \pm 0.010 \text{ kg/mm}^2$ . Out of ten tests, three of the stress-strain curves show a flat easy glide of  $0.3\%$ , six showed a rate of hardening in this region which is between one-quarter and three-quarters of the following linear hardening rate, while one did not show any sign of an easy glide region. The rate of work hardening in the linear hardening region varied from test to test between the limits  $0.07$  and  $0.18 \text{ kg/mm}^2 \%$  strain. The curves with the flat easy glide region are very similar to that shown by Gilman and Johnston (1956).

After  $10\%$  strain the specimens were considerably bulged. Though, in the early stages of deformation, slip on all systems could be seen (by etching to reveal dislocations), in heavily strained specimens gross slip

occurred only on one or two systems since, while one pair of crystal faces were considerably bulged, the pair at right angles were macroscopically flat.

Fig. 3



Stress-strain curves of irradiated lithium fluoride specimens tested in compression.

It is seen from the graphs that 1 mev electron irradiation considerably increases the yield point. A dose of  $10^{12}$  electrons/cm² just produces an increase clearly beyond experimental error and at  $10^{16}$  electrons/cm² the yield stress is raised to 15 times the unirradiated value. The easy glide

region increases to  $1\frac{1}{2}\%$  strain, even at a dose of  $10^{12}$  electrons/cm<sup>2</sup> and remains at approximately this value for doses up to  $3 \times 10^{14}$  electrons/cm<sup>2</sup> though, as in the unirradiated case, the occasional test will show no sign of easy glide (e.g. the test illustrated in fig. 3 for a specimen irradiation of  $10^{13}$  electrons/cm<sup>3</sup>). At doses above  $3 \times 10^{14}$  easy glide regions of several per cent were obtained (8% in the case of one specimen which had been given a dose of  $10^{15}$  electrons/cm<sup>2</sup>). One specimen which had been given a dose of  $6.25 \times 10^{14}$  electrons/cm<sup>2</sup>, showed an easy glide region of about 4% and in the subsequent stage of up to 10% strain the hardening was only 0.05 kg/mm<sup>2</sup> % strain, whereas another specimen did not show any easy glide but a hardening rate of 0.15 kg mm<sup>2</sup> % strain. On examination of these two specimens after testing, the one which gave 4% easy glide showed deformation predominantly on only one set of {110} slip planes whereas the other specimen showed considerable intersecting slip. This dependence of the hardening rate on the degree of intersecting slip is well known in unirradiated materials. On deformation of irradiated crystals fewer slip lines are formed for a given strain but each line contains a higher linear density of dislocations than is found in the unirradiated crystals. After irradiation, therefore, a greater strain is expected before slip on intersecting planes produces hardening. This is in agreement with the longer easy glide region in irradiated crystals.

No cracks were observed in unirradiated crystals and crystals given an irradiation dose of up to  $3 \times 10^{12}$  electrons/cm<sup>2</sup> when they were tested up to 11% strain. Cracks were first observed at  $10\frac{1}{2}\%$  strain in specimens given a dose of  $10^{13}$  electrons/cm<sup>2</sup>, 6% strain with a dose of  $3 \times 10^{14}$ , 3% strain at  $1.5 \times 10^{15}$  and a specimen irradiated to  $3 \times 10^{15}$  electrons/cm<sup>2</sup> which had been given only 0.3% strain showed many cracks. Even in these highly irradiated specimens which developed cracks in the early stages of deformation, strains of 1 or 2% could be obtained before the compression specimens shattered. The mechanism of cracking in the low dose crystals ( $< 10^{15}$  electrons/cm<sup>2</sup>) is complicated, the cracks not being confined to the {001} cleavage plane. After high doses, however, a new mechanism appears to operate. The cracks occur entirely in the {001} type planes and are initiated at the intersection of orthogonal slip planes as shown in figs. 4 and 5 (Pl. 31). Even at a magnification of 500 there is no evidence of cracking on other planes at the point of initiation. The cracks occur in the crystal in the form of slits, which sometimes extend to the crystal surfaces. This type of cracking is different from that observed by Stokes *et al.* (1958, 1959) in unirradiated MgO and is similar to that proposed by Cottrell (1958) for alpha iron. In this mechanism slip dislocations on orthogonal {110} type planes coalesce to form a new dislocation on the intersection of the planes. In fig. 6 the dislocation reaction is

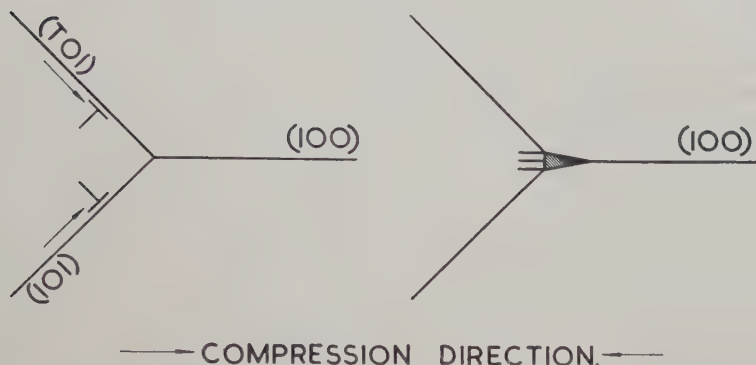
$$\frac{a}{2} [10\bar{1}] + \frac{a}{2} [\bar{1}01] \rightarrow a[00\bar{1}].$$

The new dislocation lies in the (100) cleavage plane and is equivalent to an extra half plane inserted between (100) planes. Other slip dislocations



following the original ones may also react together to form more  $a[00\bar{1}]$  dislocations so increasing the number of extra half planes on one side of the intersection until a crack forms as in fig. 6.

Fig. 6



Coalescence of slip dislocations on two slip systems to form new dislocations with extra half planes on the (100) cleavage plane to form a (100) crack.

An interesting feature of crystals which have been irradiated to doses of  $10^{14}$  electrons/cm<sup>2</sup> and above is that the slip traces show an enhanced optical absorption. This is seen clearly in fig. 4. The enhanced darkening of deformed crystals on irradiation has been reported, but this is the first observation of enhanced darkening by deformation of irradiated crystals. If, for example, the irradiation dose given to the crystal has produced a light brown colouration in it, slip produced by subsequent deformation is observed as dark brown planes extending through the crystal. The optical density in other regions, even near the slip planes, is not changed. It is possible that this enhanced optical absorption is due to colloidal lithium.

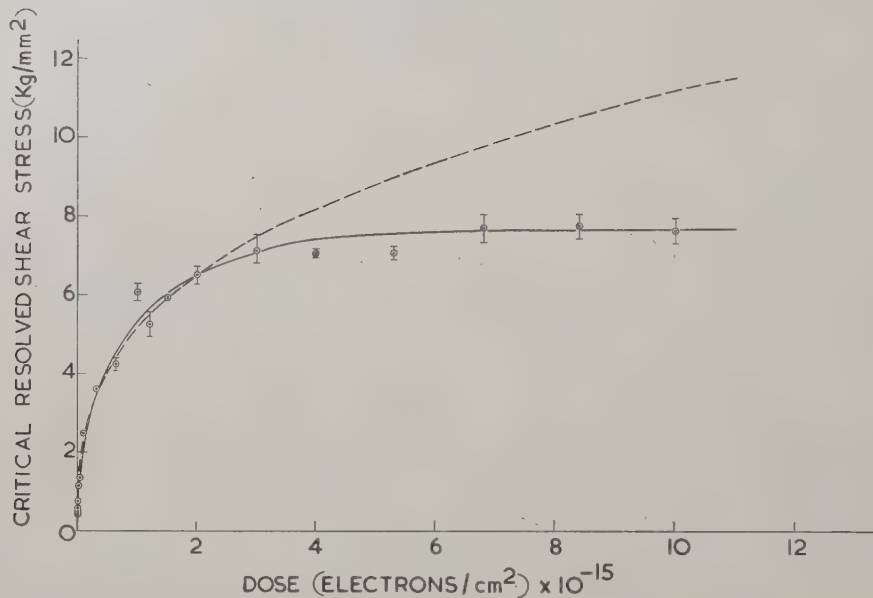
The rate of work-hardening in the linear hardening stage of the stress-strain curves for irradiated crystals is essentially the same as in the unirradiated case. There is a considerable scatter of individual hardening rates however, which would obscure a small effect.

The mean of the critical resolved shear stresses for the easy glide region is plotted against the irradiation dose  $\phi$  in fig. 7, against  $\phi^{1/2}$  in fig. 8 and  $\phi^{1/3}$  in fig. 9. Only in fig. 8 is the initial part of the curve linear indicating that at low doses ( $< 10^{14}$  electrons/cm<sup>2</sup>) the correct relationship for the dose dependence of the critical shear stress is

$$\sigma \propto \phi^{1/2}.$$

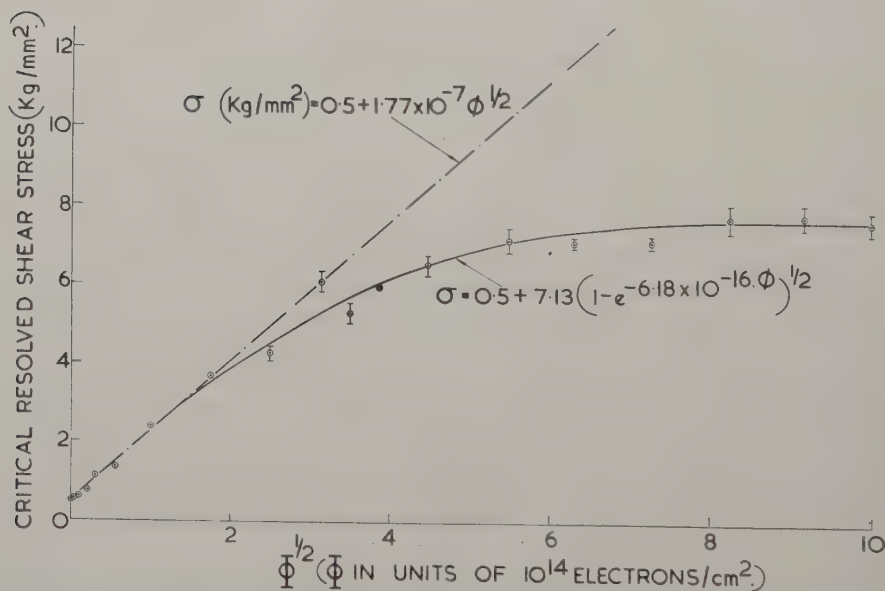
At doses greater than  $10^{14}$  electrons/cm<sup>2</sup>, however, the critical shear stress increases less rapidly than the  $\phi^{1/2}$  relationship and finally reaches a saturation value of 7.63 kg/mm<sup>2</sup>. After  $5 \times 10^{15}$  electrons/cm<sup>2</sup> the critical

Fig. 7



Plot of the critical resolved shear stress versus irradiation dose. The relation  $\sigma = 0.5 + 7.13[1 - \exp(-6.18 \times 10^{-16} \phi)]^{1/2}$  is shown as a solid line; the broken line is  $\sigma = 5.18 \times 10^{-5} \phi^{1/3}$ .

Fig. 8



Plot of the critical resolved shear stress versus the square root of the irradiation dose.

shear stress is within experimental error of the saturated value. The results have been fitted to an equation of the type

$$\sigma = \sigma_u + \sigma_i = \sigma_u + A[1 - \exp(-B\phi)]^{1/2}$$

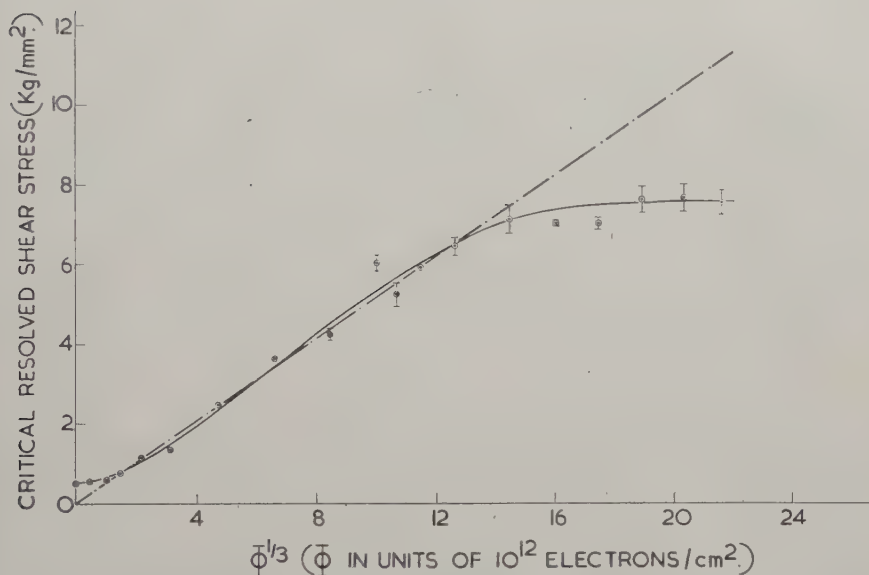
where  $\sigma_u$  = critical shear stress of unirradiated material and  $\sigma_i$  has been derived theoretically earlier in the paper.

This gives

$$\sigma = 0.5 + 7.13[1 - \exp(-6.18 \times 10^{-16}\phi)]^{1/2} \text{ kg/mm}^2.$$

This relationship is plotted as a continuous line in each graph and represents the experimental points very accurately.

Fig. 9



Plot of the critical resolved shear stress versus the cube root of the irradiation dose.

It is seen from fig. 9 that the previously used relation to describe the dose dependence of irradiation hardening in copper, namely

$$\sigma \propto \phi^{1/3},$$

does represent the experimental results between  $\phi = 10^{12}$  electrons/cm<sup>2</sup> and  $3 \times 10^{15}$  electrons/cm<sup>2</sup>. An incubation period is observed at low doses however, and above  $4 \times 10^{15}$  electrons/cm<sup>2</sup> it becomes quite clear that the cube root relationship is not the correct one.

## § 3. DISCUSSION

The most important result of this work is the establishment of the equation

$$\sigma = \sigma_u + A[1 - \exp(-B\phi)]^{1/2}$$

as the correct relationship between irradiation hardening and electron dose in lithium fluoride crystals. This equation has been derived from dislocation theory by considering the passage of dislocations through obstacles dispersed in the slip plane coupled with a saturation in the number of obstacles due to the probability of the capture of point defects by existing obstacles. At present it is not possible to determine unequivocally the volume  $v$  over which capture will occur because in the equation only the product  $av$  can be measured. An estimate of the value of  $a$  depends upon the number of defects which form an obstacle and the number of defects produced per unit irradiation dose.

Number of defects per electron	Number of point defects in a cluster ( $n_c$ )	Number of clusters per electron ( $a$ )	Volume of sphere of influence around a cluster ( $v$ in $10^{-18}\text{cm}^3$ )	Radius of sphere of influence around a cluster ( $r$ )
200	1	200	3	90 Å
	2	100	6	110 Å
	5	40	15	160 Å
	10	20	30	190 Å
	20	10	60	240 Å

Table showing how the volume  $v$  and radius  $r$  of the sphere of influence around a cluster varies with the value assumed for the number of point defects in a cluster  $n_c$ .

Values of  $v$  and the corresponding radius  $r$  based upon obstacles of various numbers of defects are given in the table. In this table it has been assumed that the cross section for the production of point defects in lithium fluoride is the same as the value (3000 barns) measured for the production of F centres in KCl by electron irradiation (Varley 1954a, b, 1956). The number of point defects estimated in this way will be a lower limit as it is possible that there may be some negative ion vacancies without an associated electron, in addition to the F centres. Here  $n_c$  is the *minimum* number of point defects which can form an obstacle which will oppose dislocation movement. It is an essential part of the theory that new defects will attach themselves to these obstacles making them grow in size as the irradiation dose increases. The volume  $v$  will be constant throughout the irradiation and will correspond to the minimum size obstacle. It is seen from the table that the most probable value of  $r$  lies between 100 and 250 Å.



It is not certain whether individual point defects could produce hardening ( $n_c = 1$ ). Gilman and Johnston (1958) notes the correlation between the onset of radiation hardening and the appearance of the 4500 Å absorption band in neutron irradiated lithium fluoride. This 4500 Å band has been ascribed to M centres (F-centre + metal-halogen vacancy pair) or some sort of electron excess centres which are larger than F centres. The etching effect in both neutron and electron-irradiated lithium fluoride observed by Gilman and Johnston (1958) is strong evidence that the obstacles grow in size with irradiation. A threshold dose is necessary for this etching effect to occur. This would be expected if obstacles could only produce an etching effect after they had grown to a critical size.

The investigations of the small angle scattering of x-rays by neutron irradiated lithium fluoride by Lambert and Guinier (1957 a) and Smallman and Willis (1957) show that small cavities having an average radius of gyration of 10–20 Å are present after exposures of greater than  $5 \times 10^{16}$  neutrons/cm<sup>2</sup>. Though no small angle scattering work has been done on electron irradiated lithium fluoride the larger cavities produced by subsequent annealing were observed and are shown in fig. 10 (Pl. 32). Further evidence of the nature of the defects in irradiated lithium fluoride is provided by the observation, by Lambert and Guinier (1957 b) of diffuse x-ray streaks along {100} directions in neutron irradiated material. These authors interpret these streaks to be caused by thin platelets of lithium metal lying on {100} planes.

The lattice hardening introduced by irradiation is on the new theory additive to the initial critical shear stress of the material. Careful analysis of the results show that the experimental formula is of the form

$$\sigma = \sigma_u + f(\phi) \quad \text{and not} \quad \sigma = f(\phi + \phi_u),$$

where  $\phi_u$  is a 'virtual' dose required to produce the critical shear stress of the unirradiated crystal. This indicates that lattice hardening introduced by irradiation is fundamentally different from the hardening responsible for the initial critical shear stress of the material.

The new relationship derived for the dose dependence of the lattice hardening component of irradiation hardening,

$$\sigma_i = A[1 - \exp(-B\phi)]^{1/2}$$

has been verified experimentally only for lithium fluoride at present. It is expected that the formula will apply generally to crystalline solids which deform by slip, however. Preliminary results on single and polycrystals of copper indicate that the equation fits the results up to the highest doses so far tested ( $10^{20}$  neutrons/cm<sup>2</sup>). The divergence between eqn. (3) and  $\sigma_i \propto \phi^{1/3}$  becomes large, however, only at high doses and the present data does not yet enable a definite decision to be made between the two relationships.

The decision between these theories is of considerable technological importance since the  $\phi^{1/3}$  relationship predicts a continually increasing

hardening with dose instead of saturation expected in the new theory. The two theories make considerably different predictions, therefore, when extrapolated to very high doses.

#### ACKNOWLEDGMENTS

The authors wish to thank Dr. J. H. O. Varley for discussions on the production of defects by irradiation, Mr. S. A. Manthorpe for experimental assistance and Dr. W. G. Burns for cooperation in irradiating the specimens.

#### REFERENCES

- BLEWITT, T. H., 1956, *Dislocations and Mechanical Properties of Crystals*, Ed. J. C. Fisher (New York : Wiley), p. 573.  
COTTRELL, A. H., 1958, *Trans. Met. Soc. A.I.M.E.*, **212**, 192.  
FRIEDEL, J., 1956, *Les Dislocations* (Paris : Gauthier-Villars).  
GILMAN, J. J., and JOHNSTON, W. G., 1956, *Dislocations and Mechanical Properties of Crystals*, Ed. J. C. Fisher (New York : Wiley), p. 116 ; 1958, *J. appl. Phys.*, **29**, 877.  
JOHNSTON, W. G., and GILMAN, J. J., 1958, *J. appl. Phys.*, **30**, 129.  
LAMBERT, M., and GUINIER, A., 1957 a, *Compt. Rend.*, **244**, 2791 ; 1957 b, *Ibid.*, **245**, 536.  
MOTT, N. F., and NABARRO, F. R. N., 1948, *Report on the Bristol Conference on the Strength of Solids* (London : Physical Society), p. 1.  
SEEGER, A. K., 1958, Second United Nations International Conference on the Peaceful Uses of Atomic Energy, A/CONF. 15/P/998.  
SMALLMAN, R. E., and WILLIS, B. T. M., 1957, *Phil. Mag.*, **2**, 1018.  
STOKES R. J., JOHNSTON, T. L., and LI, C. H., 1958, *Phil. Mag.*, **3**, 718 ; 1959, *Ibid.*, **4**, 137.  
VARLEY, J. H. O., 1954 a, *Nature, Lond.*, **174**, 886 ; 1954 b, *J. nucl. Energy*, **1**, 130 ; 1956, *Progr. nucl. Energy*, **1**, 672.  
WHAPHAM, A. D., 1958, *Phil. Mag.*, **3**, 103.

# The Electrical Resistivity of Stacking Faults†

By A. HOWIE

Crystallographic Laboratory, Cavendish Laboratory, Cambridge

[Received October 2, 1959]

## ABSTRACT

The scattering of electrons and x-rays by stacking faults is due to a phase change in the diffraction by crystal planes which do not lie parallel to the fault. A simple model of the process in copper estimates a resistivity  $\rho \approx 1 \times 10^{-12} \beta$  ohm-cm for a total stacking fault density of  $\beta$  cm<sup>-1</sup> on all planes. A wave matching calculation in which Tamm surface waves are used confirms the order of magnitude of the effect and is also in agreement with the prediction of the simple model that the distance over which scattering from two faults could interfere is less than the lattice spacing. These results are consistent with the available experimental data and it is concluded that the effect explains the resistivity caused by extended dislocations in cold worked metals and by tetrahedra of stacking faults in quenched metals.

## § 1. INTRODUCTION

### 1.1. *Resistivity of Dislocations :*

#### *Experimental Data and Theoretical Predictions*

DISLOCATIONS and point defects created during plastic deformation of a metal cause an increase in the residual electrical resistivity. The part of this resistivity increase which remains after annealing at temperatures at which point defects can diffuse is ascribed to the scattering of conduction electrons by dislocations.

From the results of Clarebrough *et al.* (1955) for the changes in density, stored energy and electrical resistivity of cold-worked copper during recrystallization, Seeger and Stehle (1956) quote for the observed resistivity increase a figure  $\rho = 2.5 \times 10^{-6}$  ohm-cm per 1% density change. If we assume that each atomic length of dislocation in the crystal increases the volume by 1.5 atomic volumes (Stehle and Seeger 1956) the dislocation density to be associated with this change in resistivity is approximately  $10^{13}$  cm<sup>-2</sup>. Thus the experimental figure for the resistivity increase in copper due to a dislocation density of  $N$  cm<sup>-2</sup> is  $\rho = 2.5 \times 10^{-19} N$  ohm-cm. More recent results of Clarebrough *et al.* (1957) for copper deformed in compression confirm this result and also indicate that the dislocation densities deduced by the above method from the density change are in reasonable agreement with those deduced from the stored energy release on recrystallization.

---

† Communicated by the Author.

The scattering of conduction electrons in copper by dislocation strain fields has been calculated by Hunter and Nabarro (1953) and for a dislocation density of  $N \text{ cm}^{-2}$  they find a resistivity increase  $\rho = 3.8 \times 10^{-21} N \text{ ohm-cm}$  which is almost two orders of magnitude smaller than the experimental figure given above. A slightly higher estimate of  $\rho = 6.0 \times 10^{-21} N \text{ ohm-cm}$  was obtained by Seeger and Stehle (1956) by considering the additional scattering effects due to anharmonic displacements and the resulting redistribution of electric charge. There might also be considerable scattering of electrons by the dislocation core where the atomic positions and electron charge distribution are not well known. Harrison (1958) has calculated the scattering from a hollow core and obtains a resistivity  $\rho = 5 \times 10^{-20} N \text{ ohm-cm}$ .

It appears therefore that even with such an extreme model of the core it is still not possible to account for almost four-fifths of the experimental value for the resistivity. Later we shall quote an example where scattering from the dislocation core is even less able to explain the observed results.

### 1.2. *Resistivity of Stacking Faults: Experimental Evidence*

A possible explanation of these anomalous dislocation resistivity results was first advanced by Broom (1952). Dislocations in the face-centred cubic lattice may dissociate, in a manner proposed by Heidenreich and Shockley (1948), into two partial dislocations separated by a ribbon of stacking fault whose width is determined by the balance between the repulsion between the two partials and the surface tension of the stacking fault. Broom suggested that stacking faults may be effective in scattering electrons and that in the case of wide ribbons most of the observed resistivity might be due to the faults. A study of the increased resistivity of nickel-cobalt wires of various alloy compositions after a standard cold drawing treatment (Broom and Barrett 1953) showed a maximum resistivity for the alloy near the transformation composition where the stacking fault energy might be expected to be low and the fault ribbons wide. If we can assume that the dislocation and point defect densities in all the wires were similar this is strong evidence in favour of a large resistivity due to scattering from stacking faults. Broom and Barrett were also able to confirm the presence of wide faults from x-ray diffraction measurements. The displacement and broadening of the diffraction peaks as a result of the presence of stacking faults has been calculated for a random distribution of parallel faults by Paterson (1952) in terms of a faulting probability  $\alpha$ . Unfortunately the interpretation of  $\alpha$  is obscure when the faults have a limited width. Nevertheless it has proved possible (Christian and Spreadborough 1956) to establish a strong correlation in several alloys between the manifestation of a large resistivity increase after cold work and a large probability of faulting  $\alpha$  in alloy filings. The experimental evidence in favour of a large resistivity due to stacking faults produced in plastic deformation is thus fairly convincing if not altogether conclusive.



To obtain an estimate of the stacking fault resistivity required to explain the experimental results we shall assume that scattering due to the dislocation core and strain field is correctly given by the theoretical predictions quoted above and is thus responsible for not more than one-fifth of the total effect. If we assume the average stacking fault ribbon width in copper (Seeger and Schoeck 1953) to be  $25\text{\AA}$  it follows that with a dislocation density of  $N\text{ cm}^{-2}$  there is associated a stacking fault density  $\beta = 2.5 \times 10^{-7} N\text{ cm}^{-1}$  considered to be equally distributed over all four slip planes. Substituting for  $N$  in the experimental value for  $\rho$  given above we find for the resistivity due to such a fault density,  $\beta$  (when the resistivity is entirely due to faults)

$$\rho = 1 \times 10^{-12} \beta \text{ ohm-cm.} \quad . \quad . \quad . \quad . \quad . \quad (1)$$

This figure is however subject to serious qualifications in view of recent suggestions (Seeger *et al.* 1959) that the stacking fault energy of copper is much higher than hitherto supposed. The equilibrium width of the stacking fault ribbon would then be much less than  $25\text{\AA}$ . Seeger (private communication) has also made new calculations of the resistivity due to the dislocation strain field and finds that the estimate should be considerably increased. The effect of these two changes is apparently to leave the predicted value for the resistivity due to stacking faults unchanged. In view of these uncertainties it is fortunate that estimates of the stacking fault resistivity can also be obtained from observations on quenched gold.

A critical study was made by Bauerle and Koehler (1957) of the annealing of the resistivity increase observed in gold wires after rapid quenching from high temperatures. It seems probable that the part of the resistivity which anneals out at temperatures above  $500^\circ\text{C}$  is due to scattering from tetrahedra of stacking faults of the type observed in foils of quenched gold by Silcox and Hirsch (1959) using the transmission electron microscope technique. Silcox (private communication) finds, on the basis of Bauerle and Koehler's data and the microscope observations, that a residual resistivity of  $\rho = 6 \times 10^{-9} \text{ ohm-cm}$ , found after quenching from  $900^\circ\text{C}$  and then annealing at  $40^\circ\text{C}$ , is to be associated with a total stacking fault density  $\beta = 1.2 \times 10^4 \text{ cm}^{-1}$  arranged in the form of tetrahedra. The resistivity of stacking faults is then

$$\rho = 0.5 \times 10^{-12} \beta \text{ ohm-cm} \quad . \quad . \quad . \quad . \quad . \quad (2)$$

where  $\beta$  is again the total fault density on all four slip planes.

It should be noted that almost all the resistivity due to the tetrahedra of stacking faults must come from the stacking faults themselves. The dislocation line length (along the edges of the tetrahedron of average length  $300\text{\AA}$ ) associated with a given area of fault is smaller by a factor of almost ten than the dislocation line length associated with the same area of fault in the deformed metal. In addition the dislocations on the edges of the tetrahedron have the small Burger's vector  $\frac{1}{6} [110]$  and are arranged so that their long range stress fields cancel. The conclusion is that the dislocations associated with the tetrahedra cannot contribute

more than a negligible amount to the scattering. Therefore although estimate (1) for the stacking fault resistivity is of more direct interest since it refers to copper (the metal to which the calculations given later apply) the quenching data for gold are probably the most reliable evidence in favour of a stacking fault resistivity of this order of magnitude.

### 1.3. *Theory of Resistivity of Stacking Faults*

A critical survey of previous attempts to investigate the scattering of conduction electrons by stacking faults has been given by Seeger (1956). He points out that in the free electron approximation (in which the potential is assumed to be constant inside the metal) electrons do not feel the presence of a stacking fault at all. For this reason a treatment by Klemens (1953), in which the fault was replaced by a scattering potential and a large reflection coefficient  $R = \frac{1}{2}$  estimated for electrons incident normal to the fault, cannot be valid since free electrons are scattered by such a potential. Another estimate of  $R = 0.4$  by Klemens (1956) was obtained by means of a deformation potential method but this approach holds only for slowly varying strains and is far outside the range of its applicability when used in the case of a stacking fault where the shear is infinite at the fault and zero everywhere else. An alternative approach to the problem is to use Bloch wave functions in the perfect crystal on either side of the fault and match these functions at the fault. Such methods have been used by Blatt *et al.* (1956) and Tweedale (see contributions of Ziman to the discussion at the end of the papers by Klemens (1956) and Seeger (1956)). Tweedale was able to perform a more complete calculation and estimated a very small reflection coefficient  $R$  of the order of  $10^{-3}$  to  $10^{-4}$ . However, as Seeger has pointed out, in neither of these investigations were surface waves at the fault considered and these waves are an essential feature of the problem.

Seeger considered the scattering from the fault in terms of a diffraction mechanism and obtained a reflection coefficient  $R$  between  $\frac{1}{10}$  and  $\frac{1}{2}$ . Unfortunately the calculation entailed a rather implausible use of perturbation theory (see § 3.1) and certain important principles of the diffraction process are obscured.

Ziman (1958) has also emphasized the part played by diffraction in the problem and has predicted a reflection coefficient proportional to the intensity of the diffracted crystal wave. He has pointed out that in view of recent results in connection with the Fermi surface in copper (see § 2) the intensity of the diffracted beam may be large. However, he has not considered in detail the effectiveness of the various diffracted beams in contributing to the resistivity.

In this paper the scattering from stacking faults as a diffraction phenomenon is examined more closely. In § 2 the necessary preliminary description of the part played by diffraction in the propagation of conduction electrons is given in terms of a specific model of the Fermi surface in copper. It then proves possible (see § 3) to build up a simple physical picture of





We shall assume that the surface near the zone has the form deduced by Pippard using a one dimensional Kronig-Penney model and shall use eqns. (6) and (7) to obtain values of  $C(\mathbf{k})$  for wave vectors  $\mathbf{k}$  on the Fermi surface where  $(\hbar^2/2m)\gamma = 5.56 \text{ eV}$ . At the Brillouin zone  $|C(\mathbf{k})| = 1$ . This follows automatically from eqn. (7) but not from eqn. (6) unless  $|U_{\mathbf{g}}|$  is chosen correctly. From the value of  $\mathbf{k}$  where the surface meets the zone we find  $(\hbar^2/2m)|U_{\mathbf{g}}| = 3.25 \text{ eV}$  so that the energy gap at the zone is  $6.5 \text{ eV}$  and compares well with Pippard's prediction of  $7.5 \text{ eV}$  on the basis of the Kronig-Penney model. We can now write eqn. (7) in a more useful form by expressing  $d$ , the distance from the end of the vector  $\mathbf{k}$  to the Brillouin zone measured normal to the zone, as a fraction  $\epsilon$  of the distance  $\Gamma L = \frac{1}{2}|\mathbf{g}|$  (fig. 2). Then  $(\mathbf{k} + \mathbf{g})^2 - \mathbf{k}^2 = 2|\mathbf{g}|d = \epsilon \mathbf{g}^2$  and using the figure deduced for  $(\hbar^2/2m)|U_{\mathbf{g}}|$  and also the value for  $(\hbar^2/2m)\mathbf{g}^2 = 34.4 \text{ eV}$  eqn. (7) can be written

$$|C(\mathbf{k})| = \frac{1}{(5.3\epsilon) + \sqrt{[(5.3\epsilon)^2 + 1]}} \quad \dots \quad (8)$$

The surface can then be divided into rings (fig. 2) which are parallel to the zone and correspond to increments of  $\epsilon$ . A value of  $|C(\mathbf{k})|$  can then be obtained for the middle of each ring using eqn. (8) and these are the first of the three values of  $|C(\mathbf{k})|$  for each ring given in table 1. The second and third figures for each ring are obtained from eqn. (6), the second from points  $\mathbf{k}$  on the surface between  $[111]$  and  $[110]$  and the third for points between  $[111]$  and  $[001]$ . These values of  $|C(\mathbf{k})|$  are in very good agreement for the first three rings and the first two figures are in fair agreement for all the rings. The deviation of the third value of  $|C(\mathbf{k})|$  for the rings furthest from the  $[111]$  Brillouin zone is due to the attraction of the Fermi surface towards the  $(002)$  Brillouin zone. In addition to this check on the usefulness of the two beam approximation we can make an estimate of the importance of the beams neglected by the theory. For electrons travelling in the  $[110]$  direction there are, by symmetry, two diffracted beams of equal amplitude. The two beam approximation holds less well for such electrons than for electrons travelling in other directions since it ignores one of these two diffracted beams entirely. The amplitude of the other diffracted beam is (using eqn. (8)) approximately  $\frac{1}{4}$  of the amplitude or  $\frac{1}{16}$  of the intensity of the direct beam. We may argue roughly therefore that the diffracted beams ignored in the two beam approximation all have intensities less than  $\frac{1}{16}$  of the intensity of the direct beam.

### § 3. A CALCULATION OF THE RESISTIVITY OF STACKING FAULTS IN TERMS OF ELECTRON DIFFRACTION

#### 3.1. *The Effect of Stacking Faults on the Diffracted Beams*

Seeger (1956) investigated the scattering in a crystal containing a fault as shown in fig. 1. He used a perturbation potential  $V'(\mathbf{r})$ .

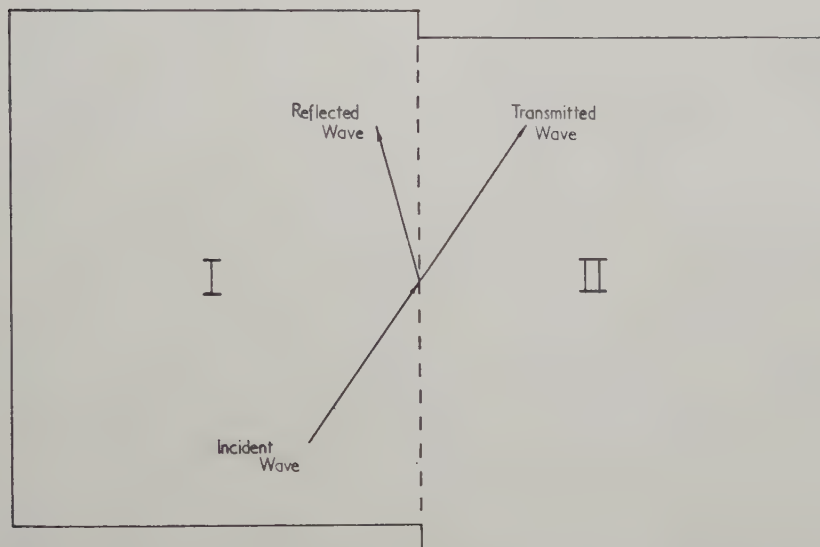
$$V'(\mathbf{r}) = 0 \text{ in region I,}$$

$$V'(\mathbf{r}) = -V(\mathbf{r}) + V(\mathbf{r} + \mathbf{R}) \text{ in region II}$$



where  $V(\mathbf{r})$  is the potential in the perfect crystal and  $\mathbf{R}$  is the displacement vector associated with the fault. Since  $V'(\mathbf{r})$  is either zero or has the same periodicity as the lattice the scattering will be from states of wave vector  $\mathbf{k}$  to those of wave vector  $\mathbf{k}' = \mathbf{k} + \mathbf{g}$  where  $(1/2\pi)\mathbf{g}$  is a reciprocal lattice vector. Perturbation theory therefore demonstrates the intimate connection between the scattering from the fault and the normal process of Bragg diffraction in the crystal. However, there is no justification for its further use since the perturbation potential  $V'(\mathbf{r})$  is as large as the crystal potential itself.

Fig. 1



Schematic diagram of a stacking fault which lies on a (111) plane and produces a shear so that the crystal in region II is translated relative to the crystal in region I by a constant amount  $\mathbf{R} = (a/6)[11\bar{2}]$ . The incident, reflected and transmitted waves used in the wave matching calculation are shown, but not the Tamm waves.

We can obtain a more precise description of the effect of the fault by noting that if the crystal potential in region I (fig. 1) is  $V(\mathbf{r})$  (eqn. (4)) and the crystal potential in region II is  $V(\mathbf{r} + \mathbf{R})$  then

$$V(\mathbf{r} + \mathbf{R}) = \frac{\hbar^2}{2m} \sum_{\mathbf{g}} U_{\mathbf{g}} \exp [i\mathbf{g} \cdot (\mathbf{r} + \mathbf{R})].$$

It then follows that in region I  $C(\mathbf{k})$  is given by eqn. (7) and in region II

$$C(\mathbf{k}) = - \frac{U_{\mathbf{g}} \exp(i\mathbf{g} \cdot \mathbf{R})}{\frac{1}{2}\{(\mathbf{k} + \mathbf{g})^2 - \mathbf{k}^2\} + \sqrt{\left\{\left[\frac{1}{2}\{(\mathbf{k} + \mathbf{g})^2 - \mathbf{k}^2\}\right]^2 + |U_{\mathbf{g}}|^2\right\}}} \quad (9)$$

Thus we see immediately that the effect of the fault is to leave the relative amplitudes of the direct and diffracted beams unchanged but to alter the relative phases of the two beams by an angle  $\alpha = \mathbf{g} \cdot \mathbf{R}$  on one

side of the fault. It is worth noting that the importance of this phase effect for the scattering of high energy (100 kv) electrons in thin foils containing stacking faults has already been realized (Whelan and Hirsch 1957) and applied to explain the contrast effects in the electron microscope image due to such specimens. The phase angle  $\alpha$  can be shown to take the values  $0^\circ$ ,  $\pm 120^\circ$  depending on the diffracting planes involved. If these planes are parallel to the fault  $\mathbf{g}$  and  $\mathbf{R}$  are mutually perpendicular so that  $\alpha=0$  and the fault has no effect. This point has been fully appreciated in the investigations made of the scattering effect of stacking faults on x-rays (Paterson 1952) and high energy electrons (Whelan and Hirsch 1957). However, it does not appear to be noted in any of the literature dealing with the scattering of conduction electrons by stacking faults. We see immediately that a fault on a (111) plane will have no effect on conduction electrons travelling in the [111] direction since these electrons will be diffracted by planes parallel to the fault. The electrons most strongly affected by the fault will be those travelling in the  $[\bar{1}11]$ ,  $[11\bar{1}]$  and  $[\bar{1}\bar{1}1]$  directions. In Seeger's calculation in which a spherical Fermi surface was used many of the diffraction effects are averaged over angles so that the simple physical picture outlined above is obscured.

Equations (7) and (9) describe the equilibrium situation between the direct and diffracted crystal waves at large distances on either side of the fault and show that it is only the phase relation between the two beams that is different on opposite sides of the fault. The detailed way in which the crystal waves change from one equilibrium situation to the other as the electron passes through the fault involves multiple Bragg scattering and interference between direct and diffracted beams from either side of the fault. Without, however, inquiring closely into these processes whose study belongs to the dynamical theory of diffraction, it is possible to come to two important conclusions.

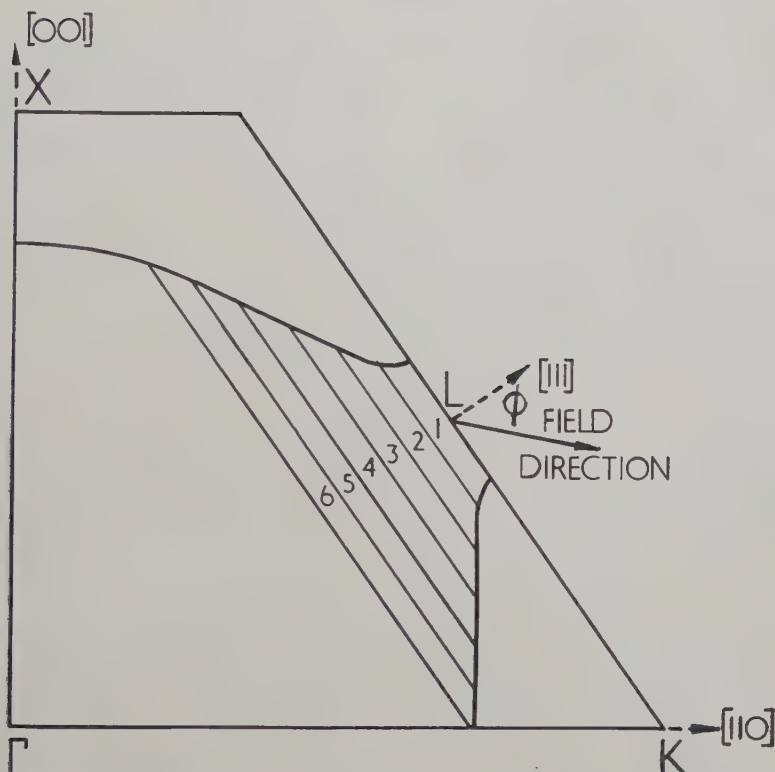
Firstly we see that the distance required to set up the new equilibrium will depend on how strongly the direct beam is diffracted. According to the dynamical theory the direct beam (when not maintained by an applied field) will be completely diffracted after travelling a distance known as the extinction distance  $t_0$  given by  $t_0 = \lambda E / |V_{\mathbf{g}}|$  (Heidenreich 1949). The extinction distance is therefore a good measure of the distance travelled by the electron before equilibrium is restored. For conduction electrons in copper diffracting from (111) planes the extinction distance is of the order of the lattice spacing.

The second conclusion is that a knowledge of what the final result of the scattering must be is sufficient to derive an expression for it. We make the assumption that the direct beam is maintained constant by the field and thus suffers no depletion as a result of the scattering. The diffracted beams, however, are purely secondary effects due to the presence of the crystal and their amplitudes and phases relative to the direct beam on either side of the fault are determined by eqns. (7) and (9) which express the conditions for dynamical equilibrium between the direct and diffracted

beams in each region. We assert, therefore, that irrespective of the detailed mechanism of the scattering, the nett effect is that enough additional electrons are scattered from the direct to the diffracted beam to set up equilibrium again. The additional intensity scattered into the diffracted beam is then

$$\begin{aligned} A(\mathbf{k}, \mathbf{k} + \mathbf{g}) &= |C(\mathbf{k})|^2 |\exp(i\mathbf{g} \cdot \mathbf{R}) - 1|^2 \\ &= 4|C(\mathbf{k})|^2 \sin^2 \frac{1}{2}\alpha. \end{aligned} \quad (10)$$

Fig. 2



Section of the Fermi surface in copper as determined by Pippard. The surface is divided into rings near the  $[111]$  direction (see text).

It is not permissible to regard this as a scattering probability since it may well be greater than unity. Values of  $A(\mathbf{k}, \mathbf{k} + \mathbf{g})$  greater than unity would of course be physically unreasonable in the absence of an applied field when there is only a definite number of electrons in the direct beam and any scattering diminishes that number. However, in the presence of the applied field the number of electrons in the direct beam is maintained constant by the acceleration of new electrons by the field and thus, since the effect of the fault extends for an infinite distance behind it, the scattering will continue until eqn. (10) is satisfied.

The rest of the calculation consists of evaluating  $A(\mathbf{k}, \mathbf{k} + \mathbf{g})$  for various values of  $\mathbf{k}$  on the Fermi surface and then of estimating the total scattering produced, for several directions of the applied field, by a given density of stacking faults equally distributed on all four sets of (111) planes. Table 1 gives the value of  $\epsilon$  and hence, by eqn. (8), of  $|C(\mathbf{k})|$  for each ring on the Fermi surface near the Brillouin zone (see fig. 2). The simplest assumptions are made about the current distribution over the surface.

Table 1

Ring No.	1	2	3	4	5	6
$\epsilon$	0.025	0.075	0.125	0.175	0.225	0.275
$ C(\mathbf{k}) $	0.87	0.68	0.54	0.44	0.36	0.31
	0.86	0.65	0.53	0.39	0.31	0.27
	0.86	0.65	0.53	0.44	0.41	0.41
$f$	0.014	0.035	0.046	0.060	0.074	0.086
$f C(\mathbf{k}) ^2$	0.011	0.016	0.013	0.011	0.010	0.008

The first row of values of  $|C(\mathbf{k})|$  are used in the calculation.

Table 2

Field Direction	Ring No.	$\gamma_1$	$\gamma_2$	$\gamma_3$	$\gamma_4$
[100]	1	0.30	0.30	0.30	0.30
	2-6	0.39	0.39	0.39	0.39
[110]	1	0.30	0	0	0.30
	2-6	0.71	0	0	0.71
[111]	1	0	0.20	0.20	0.20
	2-6	0.82	0.20	0.20	0.20

The number of current carriers from each ring is taken to be proportional to the area of the ring projected in the direction of the applied field. The velocity of the electrons assumed parallel to  $\mathbf{k}$  must also be projected in the field direction. The product  $\gamma$  of these two projection factors has been evaluated for various rings and field directions and is given in table 2.  $\gamma_1$ ,  $\gamma_2$ ,  $\gamma_3$  and  $\gamma_4$  apply to electrons near the (111), ( $\bar{1}11$ ), ( $1\bar{1}1$ ) and ( $11\bar{1}$ ) Brillouin zones respectively. The area of each ring is given in table 1 as a fraction,  $f$ , of  $\frac{1}{3}S$ .  $S$  is the total area of the Fermi surface and the factor



$\frac{1}{3}$  is the average value of the projection factor  $\gamma = \cos^2 \phi$  for a spherical surface.

The faults are assumed equally distributed on all four slip planes and each fault area must be projected in the direction of propagation of the electrons considered. This projection factor, multiplied by the appropriate value of  $4 \sin^2 \alpha / 2 = 0$  or 3, gives a further factor of  $\frac{3}{4}$  for each Brillouin zone. The fraction of the current scattered for unit area of stacking fault evenly distributed over all four slip planes is now given by

$$\chi = 2 \sum_{\text{rings}} f |C(\mathbf{k})|^2 \sum_i \gamma_i.$$

The factor 2 takes account of the four zones on the other side of the Fermi surface. We find that  $\chi$  varies by about 10% for the three field directions taken (being greatest for the [100] direction) and an average figure is  $\chi = 0.15$ . This fraction of the current is, to a fair approximation, scattered to the other side of the Fermi sphere, i.e. it is reversed in sign. Thus for the rate of change of current due to scattering we have

$$\left( \frac{\partial \mathbf{J}}{\partial t} \right)_{\text{scattering}} = -2\chi \mathbf{J} A$$

where  $A$  is the area of fault encountered per second. If  $v$  is the Fermi velocity then the average velocity,  $[\overline{v}]$ , in any direction is  $\frac{1}{2}v$  for a spherical Fermi surface and, if  $\beta$  is the density of stacking faults,  $A = \frac{1}{2}\beta v$ .

$$\text{So} \quad \left( \frac{\partial \mathbf{J}}{\partial t} \right)_{\text{scattering}} = -\chi \beta v \mathbf{J}.$$

If the rate of displacement  $\delta \mathbf{k}$  of the Fermi surface by the applied field  $\mathbf{F}$  is given by  $\delta \mathbf{k} = e\mathbf{F}/\hbar$  the current increases according to the relation

$$\begin{aligned} \left( \frac{\partial \mathbf{J}}{\partial t} \right)_{\text{field}} &= \frac{e}{4\pi^3} \int_{\text{Fermi surface}} \mathbf{v} d\mathbf{s} \cdot \delta \mathbf{k} \\ &= \frac{e^2 v S \mathbf{F}}{12\pi^3 \hbar} \text{ for a spherical Fermi surface of area } S \\ &= \frac{e^2 v S \rho \mathbf{J}}{12\pi^3 \hbar} \text{ where } \rho \text{ is the resistivity.} \end{aligned}$$

$$\text{In equilibrium} \quad \left( \frac{\partial \mathbf{J}}{\partial t} \right)_{\text{scattering}} = - \left( \frac{\partial \mathbf{J}}{\partial t} \right)_{\text{field}}$$

$$\text{so} \quad \rho = \frac{12\pi^3 \chi \hbar \beta}{e^2 S} \text{ e.s.u.}$$

Taking the area of the Fermi surface  $S = 2.2 \times 10^{17} \text{ cm}^{-2}$  and  $\chi = 0.15$  as found previously we obtain

$$\rho = 1.05 \times 10^{-12} \beta \text{ ohm-cm.}$$

It appears therefore that the stacking fault resistivity predicted by this simple model is in good agreement with the existing experimental results (eqns. (1), (2)). Doubtless the answer would be altered if a better approximation than the two beam approximation were used or if account were

taken of the variations of electron velocity over the Fermi surface but it is not expected that these refinements would affect the general order of magnitude of the result.

#### § 4. MATCHING OF BLOCH WAVE FUNCTIONS AT STACKING FAULTS

##### 4.1. *Reflection of Electrons at a Stacking Fault*

It is possible to obtain a useful check on the results derived in the last section in terms of a more formal mathematical procedure in which the various crystal waves that can propagate in the perfect crystal on either side of the fault are matched so that the wave function and its derivative normal to the fault are continuous across the fault. In addition to a wave incident on the fault in region I (fig. 1) and a transmitted wave in region II it is necessary to have a reflected wave travelling back into region I. For this reason it is possible to refer to the reflectivity of the fault although the details of the way in which the reflected wave arises from the processes of multiple diffraction which operate at the fault are not clear. Since the waves must match at all points on the fault plane it follows that all the waves used must have the same tangential components of wave vector. Consequently if the incident, reflected and transmitted waves each have a direct beam and any number  $m$  of associated diffracted beams the requirements of continuity of the wave function and its derivative will yield  $2(m+1)$  equations (two for each component beam) to be satisfied. Since it is possible to choose only the amplitudes of the direct components of the reflected and transmitted waves the problem can only be solved in the case  $m=0$  which corresponds to the free electron approximation when the fault has no effect. As Seeger (1956) has pointed out it is necessary to employ in the matching technique not only the waves which propagate in an infinite crystal but also waves localized at the surface of the fault. These waves will now be discussed.

##### 4.2. *Tamm Surface Waves*

Tamm (1932) first pointed out that it is only in an infinite crystal that all the components of  $\mathbf{k}$ , the wave vector of a Bloch wave function  $\exp(i\mathbf{k} \cdot \mathbf{r})U_{\mathbf{k}}(\mathbf{r})$  need be real. In a finite crystal there are localized surface states corresponding to complex components of  $\mathbf{k}$  normal to the surface. Such states have energies in the forbidden bands. Later authors (for references see Shockley 1939) have investigated some of their properties but they do not appear to have been extensively used. Attention seems moreover to have been restricted to the case when the Bragg diffracting planes are parallel to the surface in question. We shall require waves which are attenuated in the  $[111]$  direction and suffer diffraction from  $(\bar{1}11)$ ,  $(1\bar{1}1)$  or  $(11\bar{1})$  planes.

The conventional two-beam approximation used in § 2.2 leads to a dispersion equation

$$\{k_1^2 + k_2^2 + k_3^2 - \gamma\}\{(k_1 + g_1)^2 + (k_2 + g_2)^2 + k_3^2 - \gamma\} + |U_g|^2 = 0 \quad (11)$$

where  $\gamma = (2m/h^2)E_F - U_0$  ( $E_F$  being the Fermi energy) and the axes ( $x, y, z$ ) have been chosen so that

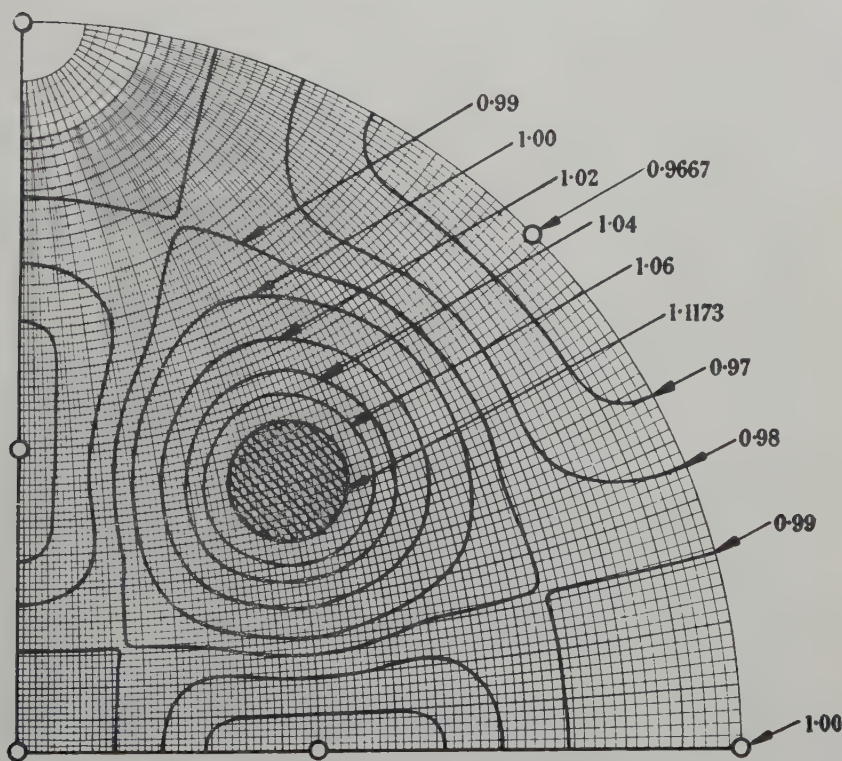
$$\mathbf{k} = (k_1, k_2, k_3)$$

and

$$\mathbf{g} = (g_1, g_2, 0).$$

Equation (11) is normally regarded as a quadratic equation for  $\gamma$  whose solution is given in eqn. (5). However, if we wish to match waves of known energy on the plane  $x=0$  it can be used as a quartic equation in  $k_1$ , the component of  $\mathbf{k}$  normal to this plane. In such wave matching calculations all allowed waves must have the same tangential components of  $\mathbf{k}$ ; i.e.  $k_2$  and  $k_3$  can also be taken as fixed. In the cases that we consider two of the roots of eqn. (11) are real and two complex. If the roots are written  $k_1, k_1', p \pm iq$  we see that  $k_1$  and  $k_1'$  represent incident and reflected waves respectively and the two complex roots describe surface waves decaying in opposite directions. Before any matching calculation can be performed it is therefore necessary to know the reflected wave vector  $\mathbf{k}' = (k_1', k_2, k_3)$

Fig. 3



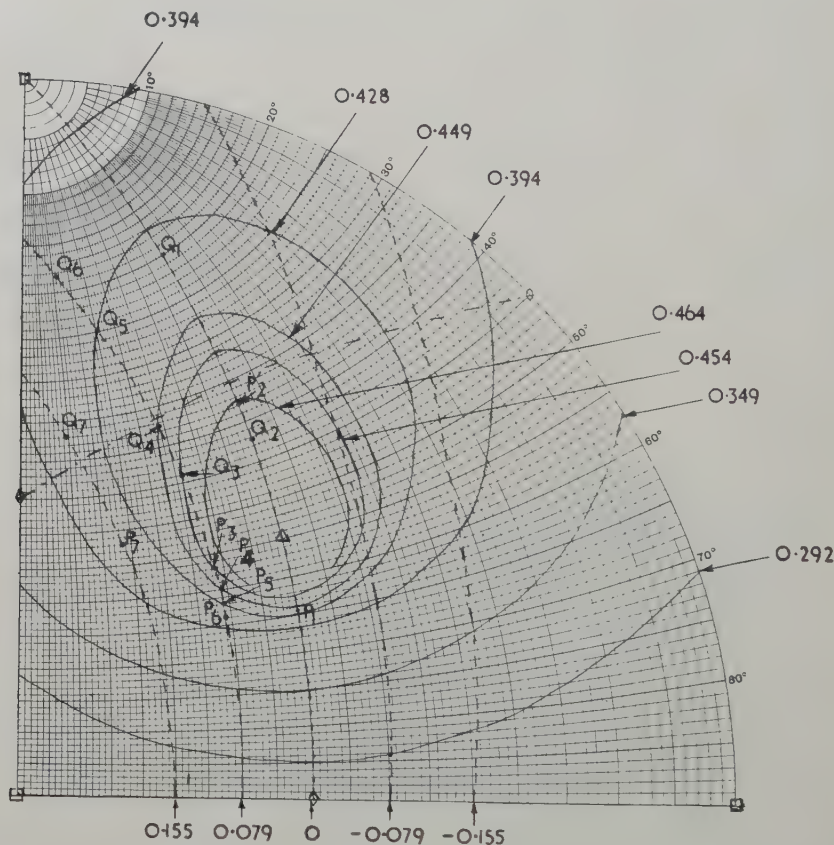
[By courtesy of the Royal Society]

Stereographic map showing contours of equal radius vector on Pippard's Fermi surface. To express the distances in the units of  $|\mathbf{g}|$  used in the text the figures given should be multiplied by 0.45.



and the Tamm wave vectors  $\mathbf{p}_{\pm} = (p \pm iq, k_2, k_3)$  associated with any incident wave vector  $(k_1, k_2, k_3)$  and energy  $E_F$  and also to know the amplitude of the diffracted wave connected with each one of these waves.

Fig. 4



Stereographic contour map for Pippard's Fermi surface showing as solid lines the contours of constant  $k_2$  (component of  $\mathbf{k}$  parallel to  $[211]$  and as dotted lines the contours of constant  $k_3$  (component of  $\mathbf{k}$  parallel to  $[011]$ ). The two points of intersection  $P$  and  $Q$  of any two contours correspond to a pair of incident and reflected waves. Note how these points do not always lie on opposite sides of the line  $k_1=0$  (the  $(111)$  plane shown with alternate dots and dashes). In these cases refraction occurs (see text). The positions of the points  $P_i$  and  $Q_i$  used in the matching are shown. The point  $P_2$  cannot be shown because it is on the other side of the Brillouin zone. It is represented by the point  $P_2'$  which has a wave vector directly opposite to that of the diffracted wave associated with  $P_2$ .

The method used to find the roots of the quartic eqn. (11) was again based on Pippard's model of the Fermi surface of copper. We take a stacking fault on a  $(111)$  plane and consider electrons moving near the



$[\bar{1}11]$  direction. It is convenient to take axis  $x, y, z$  along  $[111]$ ,  $[\bar{2}11]$  and  $[0\bar{1}1]$  respectively. With the aid of the stereographic contour map (fig. 3) that Pippard (1957) has given, a map showing contours of equal  $k_2$  and equal  $k_3$  in the vicinity of the  $[\bar{1}11]$  direction has been constructed (fig. 4). If the Fermi surface were spherical the contours of equal  $k_2$  and  $k_3$  would be small circles about  $[\bar{2}11]$  and  $[011]$  respectively but they are distorted by the attraction of the surface to the zone boundary. A given pair of contours  $k_2 = \text{constant}$  and  $k_3 = \text{constant}$  intersect in two points

Table 3

Point	$P_1$	$P_2$	$P_3$	$P_4$	$P_5$	$P_6$	$P_7$
$k_2$	0.435	0.478	0.454	0.449	0.428	0.412	0.412
$k_3$	0	0	0.079	0.079	0.079	0.079	0.155
$k_1$	0.226	0.268	0.164	0.194	0.201	0.214	0.118
$k_1'$	-0.099	0.087	0.081	0.012	-0.099	-0.145	-0.042
$p$	0.270	0.155	0.211	0.230	0.282	0.298	0.295
$q$	0.327	0.257	0.268	0.295	0.350	0.380	0.388
$C(\mathbf{k})$	0.845	1.50	0.833	0.910	0.726	0.650	0.500
$C(\mathbf{k}')$	0.403	0.795	0.607	0.490	0.403	0.382	0.371
$C(\mathbf{p}_{\pm})$	-0.070 $\pm 1.90i$	0.264 $\pm 0.857i$	0.253 $\pm 1.22i$	0.124 $\pm 1.46i$	-0.165 $\pm 2.12i$	-0.435 $\pm 2.43i$	-0.328 $\pm 2.47i$

corresponding to the incident and reflected waves. By measuring the angles to these points from  $[111]$  and using fig. 3 the values of  $k_1$  and  $k_1'$  are quickly obtained. Reference to the line  $k_1 = 0$  (the  $(111)$  plane) in fig. 4 shows that one effect of the deviation of the Fermi surface from spherical form is that  $k_1 \neq -k_1'$ , i.e. the reflection is no longer specular. Indeed for some points  $k_1$  and  $k_1'$  both have the same sign so that it appears that the direct beam is refracted rather than reflected. It is interesting to note, however, that the current  $\mathbf{J}$ , which on the average flows in the direction  $\mathbf{k} + |C(\mathbf{k})|^2(\mathbf{k} + \mathbf{g})$  is in all cases reflected (though not necessarily specularly reflected) at the fault. After  $k_1$  and  $k_1'$  have been determined by this method  $p$  and  $q$  (the real and imaginary parts of the Tamm wave vector component normal to the fault) are obtained from the relations between the roots of eqn. (11)

$$\left. \begin{aligned} k_1 + k_1' + 2p &= -2g_1, \\ 2p(k_1 + k_1') + k_1 k_1' + p^2 + q^2 &= g_1^2 + k_2^2 + (k_2 + g_2)^2 + 2(k_3^2 - \gamma) \end{aligned} \right\}. \quad (12)$$

Values of  $k_1, k_2, k_3, k_1', p$  and  $q$  in units of  $|\mathbf{g}|$  for several points  $P_1, P_2 \dots P_7$  on the Fermi surface near the  $[\bar{1}11]$  direction are given in table 3. These points correspond to different incident wave vectors  $\mathbf{k}$  and are shown in fig. 4 together with the associated points  $Q_1, Q_2 \dots Q_7$  which correspond to the reflected wave vector  $\mathbf{k}'$ . It should be noted that all the values of  $|q|$  are in the range  $\frac{1}{4}|\mathbf{g}|$  to  $\frac{2}{3}|\mathbf{g}|$  so that  $1/|q|$  the 'penetration depth' of the Tamm waves, is rather less than a lattice spacing. Thus  $1/|q| \sim t_0$  the extinction distance (see § 3.1).

Values of  $C(\mathbf{k}), C(\mathbf{k}'), C(\mathbf{p}_+)$  and  $C(\mathbf{p}_-)$ , the last two quantities describing the diffracted component of the Tamm waves, are also given in table 3 and have been calculated from eqns. (6) and (7) with the origin of  $\mathbf{r}$  so chosen that  $U_{\mathbf{g}}$  (eqns. (4), (6), (7)) is real and negative. It should be noted that because of the symmetry of the problem the situation is the same in the vicinity of the  $(\bar{1}11), (1\bar{1}1)$  and  $(11\bar{1})$  zones and also that the problem is symmetrical in  $\pm k_3$ .

#### 4.3. Matching of Waves at the Fault

The waves to be matched are two beam solutions of the Schrödinger equation in region I and II of the crystal shown in fig. 1. In region I we have:

An incident wave

$$\psi_I(\mathbf{r}) = \exp(i\mathbf{k} \cdot \mathbf{r}) + C(\mathbf{k}) \exp[i(\mathbf{k} + \mathbf{g}) \cdot \mathbf{r}].$$

A reflected wave

$$\psi_I'(\mathbf{r}) = R\{\exp(i\mathbf{k}' \cdot \mathbf{r}) + C(\mathbf{k}') \exp[i(\mathbf{k}' + \mathbf{g}) \cdot \mathbf{r}]\}$$

and a Tamm wave

$$\phi_I(\mathbf{r}) = A\{\exp(i\mathbf{p}_- \cdot \mathbf{r}) + C(\mathbf{p}_-) \exp[i(\mathbf{p}_- + \mathbf{g}) \cdot \mathbf{r}]\}.$$

Because of the fact that the current which is the important physical quantity, is always reflected at the fault the wave  $\psi_I'(\mathbf{r})$  is always considered to propagate in region I.

In region II we have:

A transmitted wave

$$\psi_{II}(\mathbf{r}) = T\{\exp(i\mathbf{k} \cdot \mathbf{r}) + C(\mathbf{k}) \exp(i\alpha) \exp[i(\mathbf{k} + \mathbf{g}) \cdot \mathbf{r}]\}$$

and a Tamm wave

$$\phi_{II}(\mathbf{r}) = B\{\exp(i\mathbf{p}_+ \cdot \mathbf{r}) + C(\mathbf{p}_+) \exp(i\alpha) \exp[i(\mathbf{p}_+ + \mathbf{g}) \cdot \mathbf{r}]\}$$

where the phase factor  $\alpha$  is  $-120^\circ$ . The requirement that the wave function be continuous at the fault gives the two equations:

$$\left. \begin{aligned} 1 + R + A &= B + T, \\ C(\mathbf{k}) + RC(\mathbf{k}') + AC(\mathbf{p}_-) &= B \exp(i\alpha)C(\mathbf{p}_+) + T \exp(i\alpha)C(\mathbf{k}). \end{aligned} \right\}$$

The requirement that the normal derivative of the wave function be continuous at the fault yields two further equations:

$$\begin{aligned} k_1 + Rk_1' + A(p - iq) &= B(p + iq) + Tk_1, \\ (k_1 + g_1)C(\mathbf{k}) + R(k_1' + g_1)C(k') + A(p - iq + g_1)C(\mathbf{p}_-) \\ &= B(p + iq + g_1) \exp(i\alpha)C(p_+) + T(k_1 + g_1) \exp(i\alpha)C(\mathbf{k}). \end{aligned}$$

The solutions to these equations for the real ( $R_1$ ,  $A_1$ ,  $B_1$ ,  $T_1$ ) and imaginary ( $R_2$ ,  $A_2$ ,  $B_2$ ,  $T_2$ ) parts of the wave amplitudes have been obtained on a computer and are given in full in table 4. The first set of seven values refer to the situation when the points  $P_1$ ,  $P_2$ ,  $\dots$ ,  $P_7$  in table 3 represent the incident beam. The second set of seven refers to the situation when these points represent the reflected beam and the incident beam is represented by the points  $Q_1$ ,  $Q_2$ ,  $\dots$ ,  $Q_7$  (see fig. 4).

Table 4

Point	$R_1$	$R_2$	$T_1$	$T_2$	$A_1$	$A_2$	$B_1$	$B_2$
$P_1$	-0.262	-0.383	+0.218	-0.863	-0.102	-0.335	-0.336	+0.289
$P_2$	-0.481	-0.417	-0.892	+0.069	-0.664	-0.239	+0.264	+1.008
$P_3$	-0.746	-0.406	-0.456	-0.401	-0.292	-0.051	-0.161	+0.391
$P_4$	-0.519	-0.455	-0.354	-0.725	-0.298	-0.252	-0.285	+0.457
$P_5$	-0.235	-0.377	+0.383	-0.791	-0.077	-0.264	-0.283	+0.188
$P_6$	-0.149	-0.324	+0.620	-0.670	-0.001	-0.218	-0.226	+0.135
$P_7$	-0.359	-0.456	+0.407	-0.686	-0.075	-0.136	-0.161	+0.090
$Q_1$	-0.251	+0.369	+0.884	-0.113	-0.022	-0.192	-0.172	-0.280
$Q_2$	-0.230	+0.208	+0.055	-0.900	-0.430	-0.377	-0.777	-0.118
$Q_3$	-0.654	+0.353	+0.583	-0.164	-0.047	-0.215	-0.168	-0.316
$Q_4$	-0.404	+0.336	+0.746	-0.238	-0.027	-0.218	-0.219	-0.332
$Q_5$	-0.271	+0.436	+0.879	-0.004	+0.023	-0.185	-0.157	-0.238
$Q_6$	-0.196	+0.427	+0.912	+0.031	+0.025	-0.168	-0.156	-0.186
$Q_7$	-0.388	+0.493	+0.762	+0.236	+0.065	-0.114	-0.081	-0.146

In view of the large number of manipulations that have been performed with quantities (the  $C(\mathbf{k})$ 's for instance) that cannot be accurately known less significance is attached to individual figures in table 4 than to the general order of magnitude of the results. Values of  $|R|^2 = R_1^2 + R_2^2$  (the second row of values referring to the second set of results in table 4) and of  $|T|^2 = T_1^2 + T_2^2$  are given in table 5. For some reason, not at present understood, the values of  $|T|^2$  seem to be almost the same irrespective of whether  $\mathbf{k}$  describes the incident or reflected beam and only one set is given.

The table shows that there is certainly a rough correlation between high values of  $|R|^2$  and low values of  $|T|^2$ . However, it is difficult to interpret the values of  $|R|^2$  directly since the velocity of the reflected electrons may be quite different to that of the incident electrons. It should also be born in mind that the waves used were not normalized. Neither of these difficulties apply to the interpretation of the values of  $|T|^2$  which show immediately that over a large area (perhaps almost all) of the Fermi surface the 'transmission coefficient' of the fault will be of the order of 0.75 say. Moreover we may regard the fraction of the electrons not transmitted (25% say) as being scattered through a fairly large angle ( $40^\circ$  which is the scattering angle for specular reflection in a (111) plane from the [111] incident direction, might be taken as a typical angle). This is to be compared with the results of the diffraction calculation made in §3 where it was shown that a fraction  $\chi = 0.15$  of the electrons were scattered through an angle of almost  $180^\circ$ . On the basis of these approximate considerations it appears that the resistivity predicted by the wave matching calculation would be rather less (perhaps by a factor of 4) than that obtained from the diffraction calculation.

Table 5

Point	$P_1$	$P_2$	$P_3$	$P_4$	$P_5$	$P_6$	$P_7$
$ R ^2$	0.21	0.40	0.72	0.48	0.20	0.13	0.34
$ R ^2$	0.20	0.10	0.56	0.28	0.26	0.22	0.40
$ T ^2$	0.79	0.80	0.37	0.65	0.77	0.83	0.64

It should be noted (see table 4) that the Tamm waves used in the wave matching calculation have in most cases rather small intensities. For the points  $P_1, P_5, P_6, P_7$   $|A|^2$  and  $|B|^2$  have values of the order of 0.1 and often less. For the other points  $P_2, P_3, P_4$  higher values occur the largest being  $|B|^2 = 1.1$  for  $P_4$ . The reason why these higher values should be associated with the cases when the direct beam is refracted at the fault is not understood. It would of course be of interest to compute the total charge density bound in surface states at the fault but this involves not only the electrons considered so far but also those inside the Fermi surface with lower energies. It seems unlikely that the average Tamm wave intensity for all these electrons is greater than one tenth of the intensity of the unattenuated waves. Since the Tamm waves appear to have a 'penetration depth' of about one-third of a lattice distance a tentative estimate would be that for every thirty atoms at the fault one electron is bound in the surface states. As a result of this charge density at the fault



the wave functions would be modified in such a way as to keep the Fermi level constant throughout the metal. The charge density would then be replaced by a scattering potential. Possibly the extra scattering produced would become important for wide ribbons of stacking fault but for ribbon widths of the order of ten atomic spacings we would expect the charge to behave rather like a line of vacancies. The charge density quoted above would be equivalent to one vacancy every three atomic distances along the dislocation and this would increase the scattering by only a few per cent.

### § 5. CONCLUSIONS

The scattering of conduction electrons by stacking faults has been shown to be due to a phase change in the diffraction from those crystal planes which do not contain the displacement vector of the fault. By using a simple physical model it has been possible to obtain an estimate of the magnitude of the effect which agrees well with experimental data and has been roughly confirmed by a wave matching calculation. The resistivity of extended dislocations in copper is therefore mainly due to the stacking fault ribbon.

The two calculations are also in agreement that the scattering from two faults should be independent provided they are further apart than one lattice spacing. This means for instance that it is justifiable to compute the effective area of a tetrahedron of stacking faults simply by adding up the areas of the faces.

It is of great importance to know whether the resistivity of stacking faults depends critically on the shape of the Fermi surface and thus varies greatly from one metal to another. We know that the resistivity will be proportional to an average value of the intensity of the diffracted beam for the electrons at the Fermi level but since the calculations described have dealt with a specific model of the Fermi surface it is not easy to draw any other general conclusions. However it is possible to calculate the stacking fault resistivity corresponding to any particular model of the Fermi surface. For instance, a rough estimate based on the Fermi surface proposed by Heine (1957) indicates that in aluminium, where the electrons are almost free, the stacking fault resistivity may be only about one-tenth of the value in copper. A low value of stacking fault resistivity might also be expected in nickel where the Fermi surface is a sphere containing 0.5 electrons per atom and does not come near any of the Brillouin zones. However, it should be borne in mind that the two-beam approximation does not provide a very good description of the conduction electrons in such a metal. In gold and silver the Fermi surface is probably rather similar to that in copper although, if the energy gap at the Brillouin zones is much less than the value of 6.5 eV assumed for copper, the surface may not make contact with the zone. Ziman (1959) has calculated that if the energy gap at the zone in copper were reduced to 5.6 eV contact would just occur. For such a Fermi surface the stacking fault resistivity would

be about three-quarters of the value calculated for Pippard's model of the Fermi surface. It thus appears that the stacking fault resistivity in these metals will still be considerable even if the Fermi surface does not touch the zone but only comes very close to it.

The wave matching technique using Tamm waves could be greatly improved in power and scope if three beams could be considered instead of two. At present the method is restricted to regions of the Fermi surface where both the incident and reflected beams are diffracted by the same set of planes. It would be interesting to apply the technique to simple tilt and twist boundaries as well as to stacking faults. Such studies would give useful information about the resistivity of undissociated dislocations (composing the boundary).

In connection with the resistivity from undissociated dislocations it should be noted that there exists a diffraction effect somewhat similar to that due to stacking faults. A dislocation of Burger's vector  $1/2 [110]$  produces a phase change in the diffracted beam which is zero for the (111) and  $(\bar{1}\bar{1}\bar{1})$  reflections and  $180^\circ$  for the (111) and  $(1\bar{1}\bar{1})$  reflections. This phase change is not, however, abrupt as in the case of the stacking fault (except near the centre of the dislocation) but takes place gradually so that the crystal waves can adapt themselves continuously to the changing conditions. However, if the phase change is significant over a distance comparable to the extinction distance the crystal waves will not be able to change rapidly enough and a large scattering will result. This will be true for electrons passing within about an extinction distance of the dislocation so that an undissociated dislocation should behave like a stacking fault of width one or two extinction distances. It is of interest to note that the close connection between the extinction distance and the distance from the dislocation within which this diffraction phase change produces strong scattering is also found in the case of high energy electrons passing through thin foils (Hirsch *et al.* 1960). For these electrons the extinction distances are about one hundred Angstroms and the image of the dislocation which is observed in the electron microscope as a result of the scattering is approximately of this width.

In copper this type of scattering might be responsible for about one-fifth of the resistivity due to the dislocations (assuming the stacking fault ribbon width to be ten atomic spacings and the extinction distance to be one atomic spacing). In aluminium where the ribbon width is only about one atomic spacing but the extinction distance is perhaps ten atomic spacings the effect is much more important and using these figures together with the estimate given above for the stacking fault resistivity in aluminium one can estimate a rough figure for the resistivity due to a dislocation density of  $N \text{ cm}^{-2}$  in this metal of  $\rho = 5 \times 10^{-20} N \text{ ohm-cm}$ . The effect may also be of importance in nickel. Thus, although detailed calculations have not been carried out, the diffraction scattering from dislocations is expected to make a contribution to the resistivity several times greater than that which would be predicted on the Hunter-Nabarro treatment.

## ACKNOWLEDGMENTS

My thanks are due to Professor N. F. Mott, F.R.S., and Dr. W. H. Taylor for their interest and encouragement, and to Drs. P. B. Hirsch and M. J. Whelan for many stimulating discussions about diffraction by stacking faults and dislocations. I am also grateful to Dr. J. Friedel, Dr. W. M. Lomer, Professor A. Seeger and Dr. J. M. Ziman for valuable comments and to Mr. C. Hunter for assistance with the use of the high speed computer. Finally I wish to thank the Master and Fellows of Trinity College for a Research Studentship.

## REFERENCES

- BLATT, F. J., HAM, F. S., and KOEHLER, J. S., 1956, *Bull. Amer. phys. Soc.*, **1**, 114.  
BAUERLE, J. E., and KOEHLER, J. S., 1957, *Phys. Rev.*, **107**, 1493.  
BROOM, T., 1952, *Proc. phys. Soc. Lond. B*, **65**, 871.  
BROOM, T., and BARRETT, C. S., 1953, *Acta Met.*, **1**, 305.  
CHRISTIAN, J. W., and SPREADBOROUGH, J., 1956, *Phil. Mag.*, **1**, 1069.  
CLAREBROUGH, L. M., HARGREAVES, M. E., and WEST, G. W., 1955, *Proc. roy. Soc. A*, **232**, 255; 1957, *Acta Met.*, **5**, 738.  
HARRISON, W. A., 1958, *J. Phys. Chem. Solids*, **5**, 44.  
HEIDENREICH, R. D., 1949, *J. appl. Phys.*, **20**, 993.  
HEIDENREICH, R. D., and SHOCKLEY, W., 1948, *Report on a Conference on Strength of Solids* (London: The Physical Society).  
HEINE, V., 1957, *Proc. roy. Soc. A*, **240**, 340.  
HIRSCH, P. B., HOWIE, A., and WHELAN, M. J., 1960, *Phil. Trans. A* (to be published).  
HUNTER, S. C., and NABARRO, F. R. N., 1953, *Proc. roy. Soc. A*, **220**, 542.  
KLEMENS, P. G., 1953, *Aust. J. Phys.*, **6**, 122; 1956, *Canad. J. Phys.*, **34**, 1212.  
PATERSON, M. S., 1952, *J. appl. Phys.*, **23**, 805.  
PIPPARD, A. B., 1957, *Phil. Trans. A*, **250**, 325.  
SEEGER, A., 1956, *Canad. J. Phys.*, **34**, 1219.  
SEEGER, A., BERNER, R., and WOLF, H., 1959, *Z. Phys.*, **155**, 247.  
SEEGER, A., and SCHOECK, G., 1953, *Acta Met.*, **1**, 519.  
SEEGER, A., and STEHLE, H., 1956, *Z. Phys.*, **146**, 242.  
SHOCKLEY, W., 1939, *Phys. Rev.*, **56**, 317.  
SILCOX, J., and HIRSCH, P. B., 1959, *Phil. Mag.*, **4**, 72.  
STEHLE, H., and SEEGER, A., 1956, *Z. Phys.*, **146**, 217.  
TAMM, I., 1932, *Phys. Z. Sowjet.*, **1**, 733.  
WHELAN, M. J., and HIRSCH, P. B., 1957, *Phil. Mag.*, **2**, 1121, 1303.  
ZIMAN, J. M., 1958, *Nuovo Cim. Suppl.* **7**, 353; 1959, *Proc. roy. Soc. A*, **252**, 63.

## Infra-red Measurements of the Optical Constants of Liquid Silver†

By J. N. HODGSON

University College of North Staffordshire, Keele, Staffordshire

[Received October 22, 1959]

### ABSTRACT

The optical constants of liquid silver have been measured in the infra-red between wave numbers 4000 and 17 000  $\text{cm}^{-1}$ . The results are compared with the Drude theory and lead to a value of about 1.1 for the effective number of free electrons per atom. The electrical conductivity of the surface layer, calculated from optical constants, differs by less than 10% from the bulk conductivity. Some results on the temperature variation of the optical constants are presented. The optical constants of liquid copper have also been measured at two wave numbers in the infra-red.

### § 1. INTRODUCTION

THE programme of infra-red measurements of the optical constants of liquid metals, which was begun with mercury, Hodgson (1959), has been continued with silver. Silver has been chosen as a typical monovalent metal. It has the lowest melting point (961°C) of the monovalent noble metals but a new furnace was needed to reach this temperature. The new furnace will maintain temperatures up to 1050°C but the heating coil fused when the temperature was raised above this value. Attempts to measure liquid copper (M.P. 1083°C) were only partly successful for this reason.

The optical constants of solid silver have been previously measured over a wide spectrum range from infra-red to ultra-violet; references in Schulz (1957). The infra-red values of the dielectric constant,  $\epsilon$ , at wave numbers less than  $10^4 \text{ cm}^{-1}$ , are in agreement with the Drude free electron formula assuming about 1.0 free electron per atom. At wave numbers above  $10^4 \text{ cm}^{-1}$  the values of  $\epsilon$  deviate from the free electron curve due to inter-band transitions. The infra-red values of the conductivity,  $\sigma$ , agree with the Drude free electron formula if the relaxation time is treated as an adjustable parameter. The required relaxation time is several times smaller than the value deduced from the static conductivity. The ratio varies for different silver surfaces and is probably connected with surface imperfections.

---

† Communicated by the Author.



## § 2. APPARATUS AND FURNACE DESIGN

The apparatus and method used for measuring optical constants were the same as previously reported (Hodgson 1959). The silver was melted in a furnace inside a water-cooled brass tank, filled with hydrogen at a pressure of about 2 cm Hg. The furnace consisted of a silica tube, 3 cm diameter by 7 cm long, wound with a heating coil of nichrome wire. The tube was supported in a steel frame and thermally insulated with alumina cement. The temperature inside the silica tube was measured with a chromel-alumel thermocouple. The melting point of silver was reached with just under 1 kw power dissipation in the heating coil. A steel crucible was used at first to contain the silver in the silica tube. Two series of measurements were made with this crucible but it gradually deformed. There was also a possibility of contamination of the liquid silver by the steel. A second crucible was made from hard carbon rod. This crucible was unaffected by liquid silver and has been used for most measurements. The water cooling did not extend to the baseplate of the brass tank and it was feared that the rubber seals of the electrodes might overheat. The rubber O-rings were therefore replaced by lead O-rings which have functioned satisfactorily. The two Pyrex windows on the tank were held against silicone rubber O-rings by atmospheric pressure.

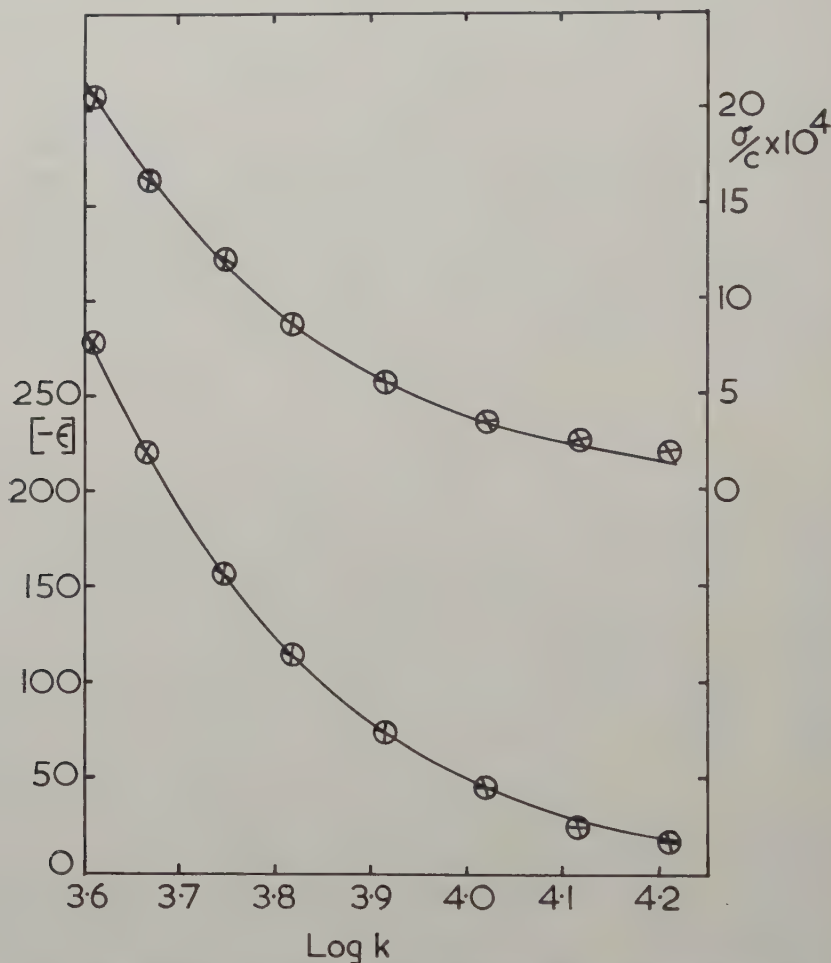
## § 3. MEASUREMENTS ON LIQUID SILVER

About 100 g of silver were needed to fill the steel or carbon crucibles. The silver used was of purity greater than 99.98%. A steel and a carbon crucible were filled with separate lots of silver. The curvature of the surface of liquid silver due to surface tension was greater than with mercury and the reflecting area was limited to the flat central part of the liquid surface. The surface was very sensitive to vibration and the supporting table had to be well insulated from the vibration of the vacuum pump. When first melted the silver had a cloudy surface but the cloudy areas soon moved to each end of the silver blob leaving a clear area in the middle. This clear area showed no scattered light even at angles close to the reflected beam. The impossibility of cleaning a liquid silver surface *in situ* was a disadvantage of this apparatus. A surface cleaning method similar to that used for mercury would be difficult to apply.

Optical constants were measured at eight points in the infra-red spectrum. The experimental errors have been estimated by taking probable errors of the measured angles and calculating the corresponding errors in  $\epsilon$  and  $\sigma$ . In fig. 1, the errors lie within the plotted circles. The ribbon filament lamp used as radiation source in the infra-red measurements was replaced by a mercury lamp for visible and ultra-violet measurements. The angle of incidence ( $81.5^\circ$ ) was unsuitable for measurements on silver in this spectrum range. The accuracy of the results is therefore low, but much better for  $\epsilon$  than  $\sigma$ . The experimental values of  $-\epsilon$  and  $\sigma/c$  in fig. 2 have probable errors  $\pm 0.4$  and  $\pm 0.2 \times 10^4$ , respectively.

Four sets of infra-red measurements were made over a period of several months, two on silver in the steel crucible and two on silver in the carbon crucible. These sets of measurements show differences which will be described later. The points of fig. 1 represent a typical set of results. An attempt was made to measure the temperature variation of  $\epsilon$  and  $\sigma$  over the limited temperature range available, about  $100^\circ\text{C}$ .

Fig. 1



Liquid silver (infra-red). Experimental points for liquid silver (Ag-1); theoretical curves calculated from (3) and (4) with  $k_0^2 = 5.26 \times 10^8$ ,  $k_R = 1.51 \times 10^8$ , (i.e.  $N_0 = 1.13$ ,  $\sigma_0/c = 174 \times 10^4$ ).

#### § 4. DISCUSSION

The number of atoms per  $\text{cm}^3$  ( $N_A$ ) and the static electrical conductivity in e.s.u. ( $\sigma_0$ ) for liquid silver, have been calculated from data in *Metals*

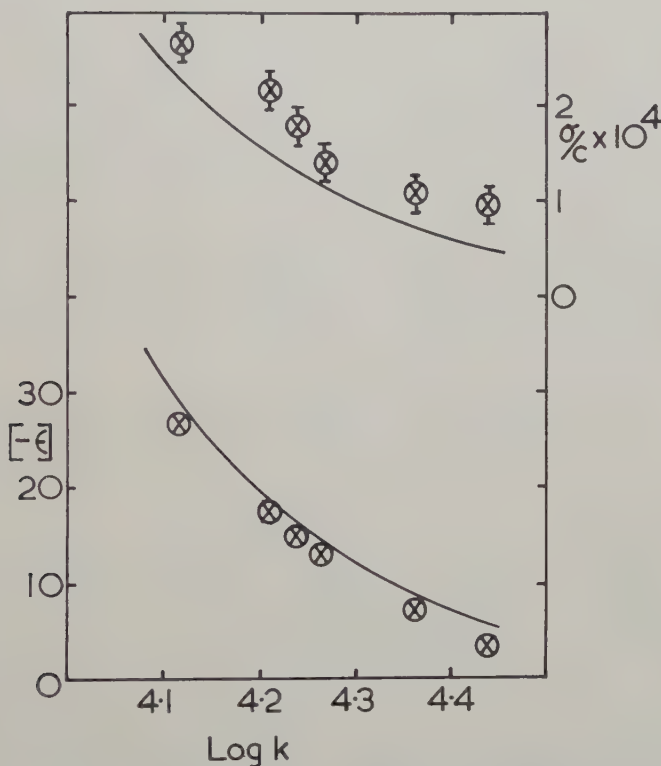
*Reference Book* (Smithells 1955). At a temperature  $t^\circ\text{C}$  between the melting point and  $1100^\circ\text{C}$ :

$$N_A = 5.20 \times 10^{22} [1 - 9 \times 10^{-5}(t - 961)], \quad . . . . . (1)$$

$$\sigma_0/c = 1.82 \times 10^6 [1 - 5.8 \times 10^{-4}(t - 961)]. \quad . . . . . (2)$$

The ratio of the conductivity of the solid to the conductivity of the liquid at the melting point is 2.1. This agrees with the theory of Mott (1934) who assumed no change in the number of conduction electrons per atom when a metal melts.

Fig. 2



Liquid silver (visible and ultra-violet). Experimental points for liquid silver; theoretical curves continued from fig. 1.

The experimental values of  $\epsilon$ , the dielectric constant, and  $\sigma$ , the conductivity in e.s.u., have been compared with Drude's free electron formulae:

$$1 - \epsilon = k_0^2 / (k^2 + k_R^2), \quad . . . . . (3)$$

$$\sigma/c = \frac{1}{2} k_0^2 k_R / (k^2 + k_R^2) \quad . . . . . (4)$$

$k$  is the wave number in  $\text{cm}^{-1}$ ;  $k_0^2 = (N e^2) / (\pi m^* c^2)$ , where  $N$  is the number of free electrons per  $\text{cm}^3$  of charge  $-e$  and effective mass  $m^*$ ;  $k_R = 1 / (2\pi c \tau)$ ,

where  $\tau$  is the relaxation time. The effective number of free electrons per atom is defined by:

$$N_0 = \left( \frac{N}{m^*} \right) / \left( \frac{N_A}{m} \right). \quad . . . . . (5)$$

When  $k=0$ , then:

$$\sigma_0/c = \frac{1}{2} k_0^2 / k_R. \quad . . . . . (6)$$

The formula (3) for  $\epsilon$  does not include a small term due to ion core polarization. Using the value of polarizability of the  $\text{Ag}^+$  ion given by Van Vleck (1932), the ion core contribution to  $\epsilon$  has been estimated as 1.1.

Values of  $k_0^2$  and  $k_R$  were calculated by means of (3) and (4) for each pair of experimental values of  $\epsilon$  and  $\sigma$  at the same wave number,  $k$ . For  $\log k$  between 3.6 and 4.0, these values of  $k_0^2$  and  $k_R$  are constant, within experimental error, for each set of measurements. This may be seen in fig. 1 where the experimental values Ag-1 are compared with curves calculated from formulae (3) and (4). Average values of  $k_0^2$  and  $k_R$  for each set of measurements are given in the table. Ag-1 and Ag-2 refer to liquid silver in a steel crucible; Ag-3 and Ag-4 refer to liquid silver in a carbon crucible. The temperatures used for Ag-1 and Ag-2 are uncertain because of a fault in the thermocouple circuit.  $N_0$  and  $\sigma_0/c$  were calculated by means of (5) and (6). The reason for the variations in  $k_0^2$  and  $k_R$  for different sets of measurements has not been found and requires further investigation.

Experimental Values for Liquid Silver

	$k_0^2$	$k_R$	$N_0$	$\sigma_0/c$	$t$
Ag-1	5.26	1.51	1.13	174	—
Ag-2	5.44	1.66	1.17	164	—
Ag-3	5.02	1.53	1.09	164	1020
Ag-4	5.34	1.44	1.15	185	1000
	$\times 10^9 \text{ cm}^{-2}$	$\times 10^3 \text{ cm}^{-1}$		$\times 10^4$	$^{\circ}\text{C}$

The infra-red values of  $\sigma_0/c$  do not differ by more than 10% from the electrical values given by formula (2). This indicates that for liquid silver the surface layer has nearly the same conductivity as the bulk metal. The values of  $N_0$  for liquid silver are larger than the accepted optical value for solid silver,  $N_0 = 1.03$  ( $m^*/m = 0.97$ ), quoted by Schulz (1957). This value is probably uncertain by at least  $\pm 3\%$ . The experimental points at wave numbers greater than  $10^4 \text{ cm}^{-1}$  deviate from the infra-red theoretical curves as shown in fig. 2.

The temperature variation of the optical constants was measured at  $\log k = 3.748$  and  $4.020$ . The constants were measured initially at about  $1000^{\circ}\text{C}$ , then at about  $1090^{\circ}\text{C}$ , and finally again at about  $1000^{\circ}\text{C}$ . The initial and final values agreed within experimental error and the measurements were repeated with consistent results. Values of  $k_0^2$ ,  $k_R$ , and



$\sigma_0/c$  (infra-red) were calculated from the experimental values of  $\epsilon$  and  $\sigma$ . The temperature coefficients have been calculated as fractions of the initial values (i.e. near the melting point).

Parameter	$k_0^2$	$k_R$	$\sigma_0/c$
Temperature coefficient per °C	$-2 \times 10^{-4}$	$+6 \times 10^{-4}$	$-8 \times 10^{-4}$
	(probable error $\pm 1 \times 10^{-4}$ )		

The coefficients of  $k_0^2$  and  $\sigma_0/c$  are of the same order as the coefficients of  $N_A$  and  $\sigma_0/c$  (electrical) in formulae (1) and (2).

### § 5. MEASUREMENTS ON LIQUID COPPER

Pieces of sheet copper of 99.998% purity were melted in a carbon crucible. The furnace maintained a temperature sufficient to melt copper for only a few minutes before the heating coil fused. Measurements of the optical constants of liquid copper were obtained at two wave numbers.

$\log k$	$-\epsilon$	$\sigma/c$	$k_R$	$k_0^2$
3.645	209	30.7	2.94	5.91
3.748	146	22.3	3.05	5.97
		$\times 10^4$	$\times 10^3 \text{ cm}^{-1}$	$\times 10^9 \text{ cm}^{-2}$

The average values of  $k_0^2$  and  $k_R$  lead to  $N_0 = 0.84$  and  $\sigma_0/c$  (infra-red)  $= 99 \times 10^4$ , compared with  $\sigma_0/c$  (electrical)  $= 141 \times 10^4$  at the melting point.

### § 6. CONCLUSION

The infra-red optical constants of liquid silver can be explained by the simple Drude free electron theory. The number of free electrons per atom is about 1.1 and their relaxation time about  $7 \times 10^{-15}$  sec. The value of the static electrical conductivity derived from the infra-red measurements agrees fairly well with the electrically measured value. These results are in contrast to those for liquid mercury, which cannot be represented by the free electron formulae.

### ACKNOWLEDGMENT

I would like to thank Professor D. J. E. Ingram for valuable discussion of this paper.

### REFERENCES

- HODGSON, J. N., 1959, *Phil. Mag.*, **4**, 183.  
 MOTT, N. F., 1934, *Proc. roy. Soc. A*, **146**, 465.  
 SCHULZ, L. G., 1957, *Advanc. Phys.*, **6**, 102.  
 SMITHELLS, C. J., 1955, *Metals Reference Book* (Butterworths), p. 639.  
 VAN VLECK, J. H., 1932, *Electric and Magnetic Susceptibilities* (Oxford: University Press), p. 225.

# The Damage and Recovery of Neutron Irradiated Tungsten†

By M. W. THOMPSON

Atomic Energy Research Establishment, Harwell, Berks.

[Received October 6, 1959]

## ABSTRACT

Residual electrical resistivity has been used as an index of the damage present in tungsten irradiated in a nuclear reactor at 4°K and 77°K. A comparison was made between four different types of specimen prepared from cold-drawn wire respectively annealed before irradiation at 2000, 1500, 800°C and not at all. A fifth type of specimen was prepared from wire in a different state of purity.

Four stages of recovery have been identified, the first occurring below -170°C, the second between -170 and 350°C with an activation energy rising from 0.25 to 1.7 ev, the third between 350 and 450°C with a single activation energy of 1.7 ev and the fourth above 450°C. Second-stage recovery was enhanced by the presence of cold-work, affected by impurities and in well-annealed samples after light irradiations it was suppressed.

A comparison of recovery with that in other metals leads to the conclusion that vacancies in tungsten migrate at 400°C with an activation energy of 1.7 ev. The general suggestion is advanced that vacancy migration occurs in all metals at a temperature approximately 20% of the absolute melting point  $T_m$  °K, with an activation energy roughly  $5 \times 10^{-4} T_m$  ev.

Recovery in tungsten above -170°C is attributed to the release of interstitials from traps associated with impurity atoms and dislocation lines. The free interstitial is assumed to become mobile below -170°C.

The resistance *versus* dose curve for cold-worked tungsten shows acceleration and this is considered as evidence for the action of spikes on the unstable arrays of vacancies produced by deformation.

A quantitative theory of damage and recovery developed from the above model predicts the observed behaviour of the five types of tungsten specimen.

## § 1. INTRODUCTION

In this paper experiments are presented in which neutron irradiation damage has been studied by observing changes in the electrical resistivity of tungsten. It has previously been shown that after irradiation at -196°C this damage recovers by thermal annealing in two main stages at -80°C and at 350°C, the activation energies associated with these stages being 0.5 ev and 1.7 ev (Kinchin and Thompson 1958). Later work showed that the low-temperature recovery was not observed after very short irradiations and this led to the suggestion that low-temperature recovery was due to a mobile defect being released from trapping centres (Thompson 1958 a).

---

† Communicated by the Author.

The following experiments have been designed to determine both the nature of the mobile defect and of its traps:

- (i) The effect of neutron dose on recovery.
- (ii) A comparison of annealed and cold worked tungsten.
- (iii) A comparison of material from different manufacturers.
- (iv) Recovery after irradiation in liquid helium.

## § 2. EXPERIMENTAL

### 2.1. Specimens

In table 1 the various types of specimen which have been used are listed with some physical properties. Specimens made of Johnson Matthey tungsten annealed at 1500°C were used for reference in all comparative experiments. Specimens made direct from manufactured wire were found to be in a sufficiently cold-worked state for experiment (ii).

Table 1. Specimens

Type	A	B	C	D	E
Experiment	(i)	(i), (ii), (iii) & (iv)	(ii)	(ii)	(iii)
Manufacture	Johnson-Matthey Co., London				Tungsten Mfg. Co. London
Spec. analysis	0.005% Fe				spec. pure
Temp. of pre- irradiation anneal, °C	2000	1500	500	No anneal	1500
Grain size, microns	100	10	needles 1 × 25	needles 1 × 25	10
Residual resistivity micro-ohm cm	0.04	0.06	0.30	0.36	0.09

The specimens were made from 0.008 in. diameter wire which had been cleaned electrolytically in caustic soda solution using a nickel anode. A 7 cm length of wire had potential leads of the same wire spot welded at a distance of 1 cm from either end. The resulting specimen was spot welded to leads passing through a pressed glass seal which was subsequently fused into a lead glass envelope using a purified argon atmosphere to prevent oxidation. The envelope was evacuated and outgassed at 350°C after

which type A, B and E specimens were given a pre-irradiation anneal by passing a current before finally sealing off. In the case of type C specimens the pre-irradiation anneal was given to the wire before mounting.

## 2.2. Resistance Measurements

All resistance measurements were carried out in liquid helium using a potentiometer to compare the voltage drop across the specimen with that across a standard resistance carrying the same current. In order to eliminate drifts a regulating device (Thompson 1958b) held this current constant to 0.001%. The residual resistance of the specimen was measured to an accuracy of 0.003%. Because of uncertainties in the dimensions absolute resistivity could only be measured to a few per cent.

## 2.3. Irradiations

Irradiations were carried out in three vertical holes of the BEPO reactor at Harwell. These holes, TE.1, TE.3 and TE.13, penetrate the reactor core transverse to the fuel channels and have approximately the same thermal neutron flux of  $10^{12}$  neutrons  $\text{cm}^{-2}\text{sec}^{-1}$ . Using sulphur detectors (Martin and Stanwix 1956) alongside the resistance specimens, the flux of neutrons with energies in excess of 1 mev was measured and found to be  $3 \times 10^{10}$  in TE.1 and TE.13 but  $1.2 \times 10^{11}$  in TE.3. However, in spite of these variations the resistance increase for a given time and a given type of specimen, was constant to within 10% in any of the holes used. This implies that damage is chiefly due to neutrons below 1 mev in these holes. In view of this constant resistance increase all irradiation doses have been specified as times rather than integrated neutron fluxes.

Short irradiations in liquid nitrogen were carried out in an open lead glass dewar which was lowered into the TE.13 hole whilst the reactor ran at full power. The 12-hour irradiation was carried out in a liquid nitrogen cryostat (Thompson and Jefferson-Loveday 1958) in hole TE.1. Irradiations lasting 1 week were performed with the nitrogen cryostat in hole TE.3. After all these irradiations the specimens were removed from the pile in liquid nitrogen and mounted in the laboratory cryostat without warming up.

An irradiation lasting  $8\frac{1}{2}$  min was carried out in liquid helium using two concentric dewars, the outer one containing liquid nitrogen and the inner one about 200  $\text{cm}^3$  of liquid helium. This assembly was lowered into the TE.13 hole, a carbon resistance thermometer indicating when two-thirds of the liquid helium had boiled away. At this stage the dewars were removed from the pile and topped up with liquid. After waiting an hour for radioactivity to decay the complete assembly was removed to the laboratory where the residual resistance of the specimen was measured *in situ* through leads which had been attached before irradiation.



### 2.4. Annealing After Irradiation

After irradiation in liquid nitrogen the specimens were attached to measuring leads and placed in a cryostat-furnace assembly mounted above a liquid helium bath (Stubbs and Thompson 1958). This apparatus enabled resistance measurements to be made in liquid helium between 30 min annealing periods at successively higher temperatures in the range  $-196$  to  $200^{\circ}\text{C}$ . For annealing at higher temperatures specimens were removed to a separate furnace. Temperature was in all cases measured and controlled to  $\pm 0.1^{\circ}\text{C}$ .

Recovery curves were obtained by plotting  $(R_T - R_0)/(R_I - R_0)$ . Where  $R_T$  is the residual resistance after annealing at temperature  $T$  and  $R_0$  and  $R_I$  are the values before and after irradiation.

## § 3. RESULTS

### 3.1. The Effect of Neutron Dose

In fig. 1 the recovery curves for a Johnson-Matthey specimen annealed before irradiation at  $1500^{\circ}\text{C}$  and irradiated at  $-196^{\circ}\text{C}$  for 1, 12 and 140 hours are compared. Before each successive irradiation current was passed through the specimen to heat it to  $150^{\circ}\text{C}$  and to restore its residual resistance to  $R_0$ . To check reproducibility two other specimens were irradiated for 1 hour and 140 hours, their results are also plotted in fig. 1. The increase of resistivity of the first specimen with irradiation is shown in fig. 4(b).

Apparently the effect of decreasing dose is to reduce the proportion of recovery at low temperatures. The increase of resistance with irradiation time shows slight deceleration.

### 3.2. Comparison of Annealed and Cold-worked Tungsten

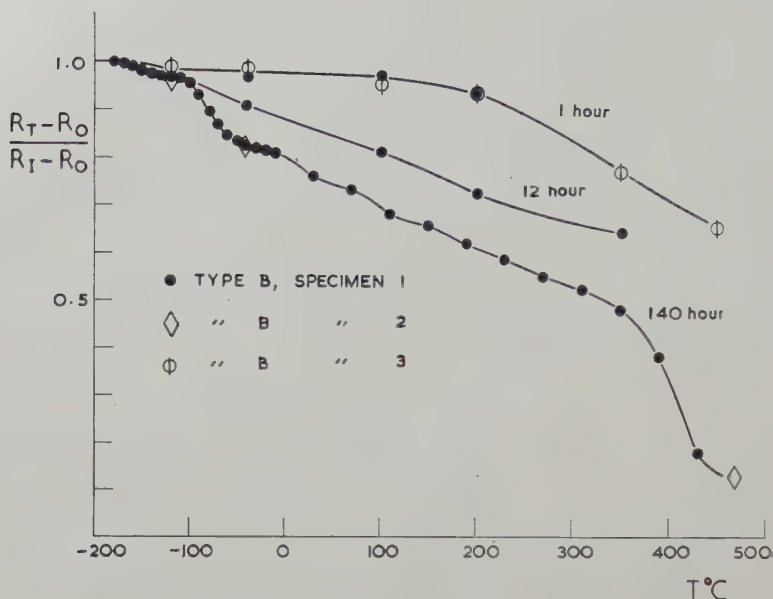
The recovery curves for Johnson-Matthey tungsten wire in the cold-worked,  $500^{\circ}\text{C}$  annealed,  $1500^{\circ}\text{C}$  annealed and  $2000^{\circ}\text{C}$  annealed states are compared in fig. 2 after 140 hour irradiations at  $-196^{\circ}\text{C}$ . In fig. 3 the comparison is made after a 1-hour irradiation. The increase of resistivity with irradiation time is shown in fig. 4 for the four types of specimen.

The presence of cold-work evidently introduced its own recovery above  $250^{\circ}\text{C}$  (which is in agreement with the findings of Schultz (1959)) and enhanced recovery in irradiated specimens below  $30^{\circ}\text{C}$ . Although there is little difference between the recovery of  $1500^{\circ}\text{C}$  annealed and  $2000^{\circ}\text{C}$  annealed specimens those which were annealed at  $500^{\circ}\text{C}$  before irradiation showed rather less recovery in the range  $350$  to  $450^{\circ}\text{C}$ . The resistance of cold-worked specimens increased more slowly with irradiation time than that of annealed specimens and showed acceleration rather than deceleration.

### 3.3. Comparison of Material from Two Manufacturers

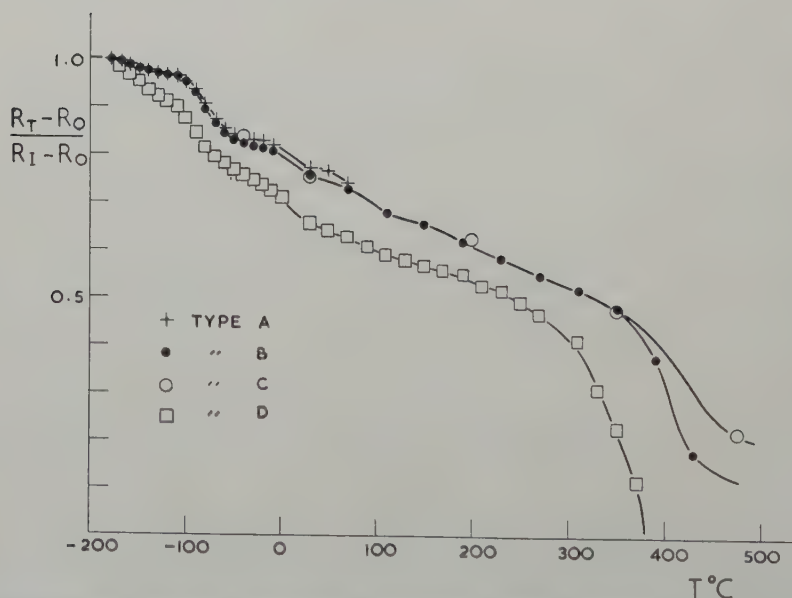
In view of the difficulty experienced in obtaining tungsten with controlled impurities, it was decided to compare two materials from different manufacturers. In fig. 5 the recovery of tungsten supplied by Johnson-Matthey

Fig. 1



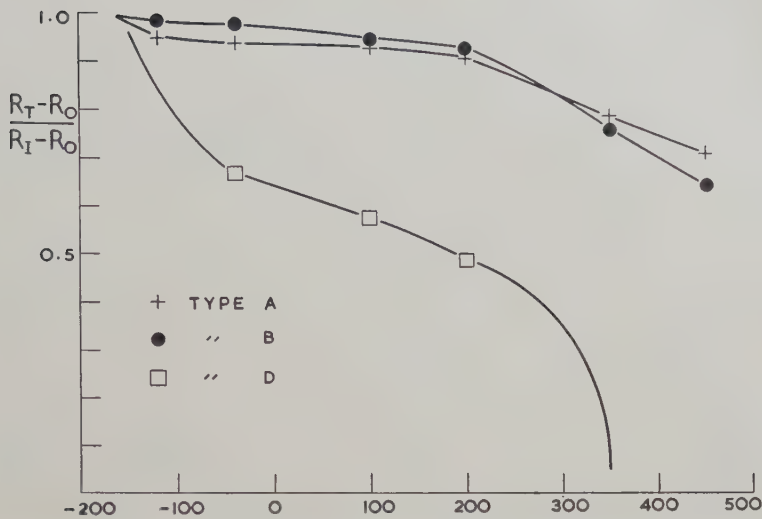
The effect of irradiation time on recovery for specimens of type B.

Fig. 2



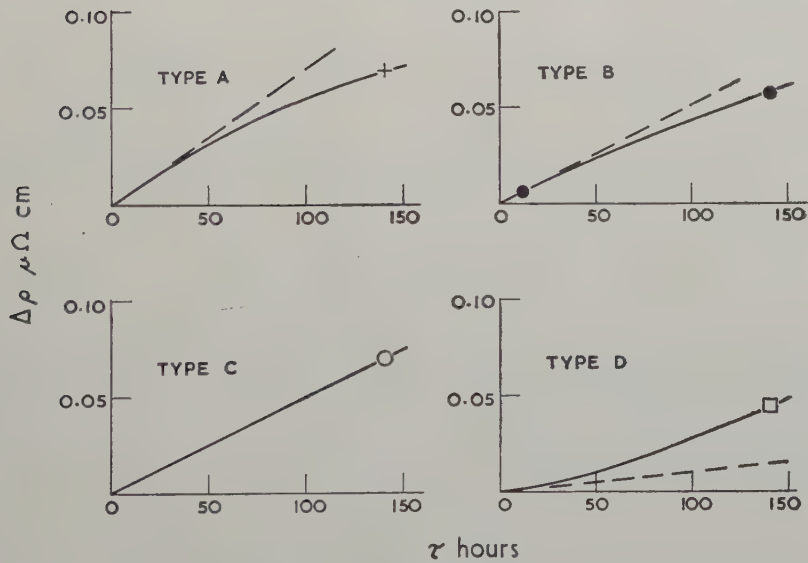
Recovery as a function of annealing treatment before irradiation; specimens of type A, B, C and D after 140 hour irradiations at  $-196^\circ\text{C}$ .

Fig. 3



Recovery as a function of annealing treatment before irradiation; specimens of type A, B and D after 1 hour irradiations at  $-196^{\circ}\text{C}$ .

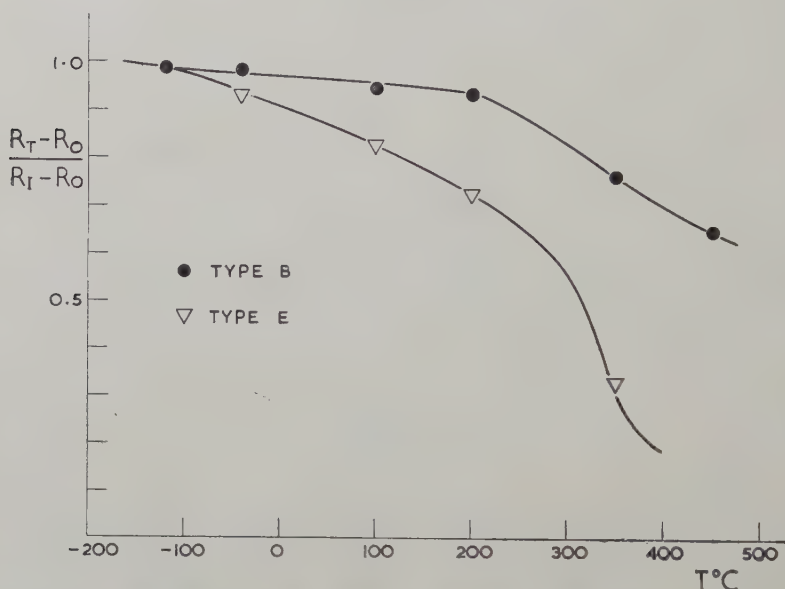
Fig. 4



Resistance increase *versus* irradiation time at  $-196^{\circ}\text{C}$  for four types of specimen A, B, C and D. Slope at the origin is estimated from increase observed after 1-hour irradiations.

is compared with that from the Tungsten Manufacturing Co. after both specimens had been irradiated together in liquid nitrogen for 1 hour. Both were annealed at  $1500^{\circ}\text{C}$  before irradiation. Whereas the Johnson-Matthey specimen increased by  $5.4 \times 10^{-4}$  micro-ohm-cm the other increased by only  $1.7 \times 10^{-4}$  micro-ohm-cm in the same time. From the residual resistivities, given in table 1, it is clear that this second specimen was in a different state of purity from the Johnson-Matthey specimen. The effect of these impurities is evidently to enhance recovery after short irradiations, particularly above  $0^{\circ}\text{C}$ .

Fig. 5



Comparison of recovery in materials of different purity but the same pre-irradiation annealing treatment; specimens of type B and E irradiated for 1 hour at  $-196^{\circ}\text{C}$ .

### 3.4. Recovery after Irradiation at $4^{\circ}\text{K}$

After  $8\frac{1}{2}$  min irradiation in liquid helium the resistivity of a Johnson-Matthey specimen annealed before irradiation at  $1500^{\circ}\text{C}$  increased by 0.0028 micro-ohm-cm. Of this increase 30% annealed after 30 min at  $-196^{\circ}\text{C}$  and a further 20% after 30 min at  $25^{\circ}\text{C}$ . Since it is known that for short irradiations little recovery occurs in the range  $-120$  to  $100^{\circ}\text{C}$  the recovery curve may be sketched as in fig. 6.

## § 4. DISCUSSION

### 4.1. The Resistivity Increase

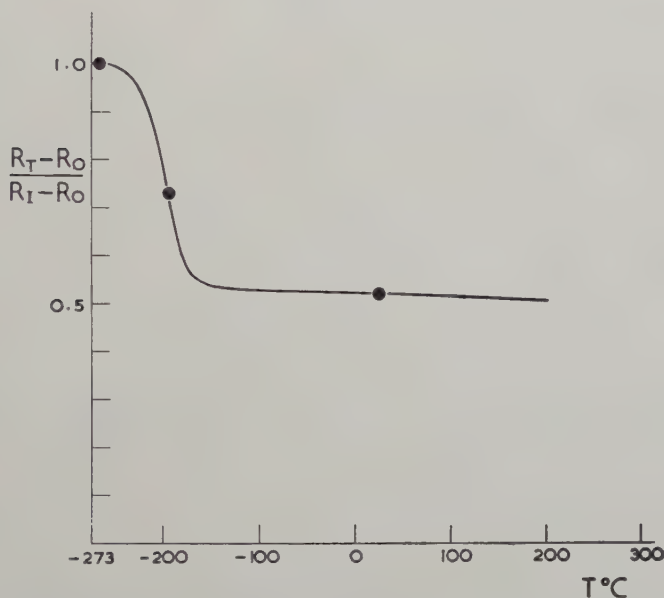
The observed change of resistivity with irradiation time may be interpreted using a model based on the following three postulates.



(i) Irradiation produces interstitial atoms and vacant lattice sites in equal numbers, the former defect being mobile at liquid nitrogen temperature. An attempt to justify this assumption will be made in §4.2.

(ii) It also produces 'spike' regions of temporary local disorder containing of the order  $10^5$  atoms. The existence of such regions has been demonstrated in the III-V compounds by Gonser and Okkerse (1958). In tungsten the recoiling atom from a neutron collision is in the energy range ( $10^4$  ev) where it behaves like a hard sphere with a mean free path of a few angstrom units. It therefore enters the spike region straight away and we may expect that all interstitials and vacancies are left as debris after the spikes have subsided. Thus it is unlikely that further spikes will affect the vacancies already present.

Fig. 6



Recovery after an irradiation of 8 min at  $4^\circ\text{K}$ ; B type specimen.

(iii) In a perfect infinite crystal at a temperature where only interstitials are mobile mutual annihilation would prevent the accumulation of defects. In a real specimen however, in addition to vacancies there will be the following sinks for interstitials: surfaces and suitable grain boundaries, dislocations and foreign atoms of favourable size. These last two may only be temporary sinks, or traps, from which the interstitial is activated by heating the specimen (Lomer and Cottrell 1955, Blewitt *et al.* 1957). It follows, therefore, that the number of vacancies present at any stage is equal to the number of interstitials which have either been trapped on temporary sinks or been lost to the permanent sinks.

Let  $C$  be the total concentration per atom of interstitials or vacancies produced by irradiation,  $T_r$  be the initial concentration of the  $r$ th type of trap,  $C_r$  the concentration per atom of interstitials on the  $r$ th trap and  $C_b$  the concentration lost to boundary sinks of which there is a constant concentration  $B$ .  $B$  must be regarded as an effective concentration which would apply if the sinks were uniformly distributed through the crystal. Consider the situation as  $C$  increases to  $C + dC$ . The extra  $dC$  interstitials have the choice of  $(T_r - C_r)$  unfilled traps of type  $r$ , of any other unfilled trap, of finding a boundary sink, or of annihilating the vacancies present at a concentration  $(\sum C_r + C_b)$ . It follows from simple proportion that the increase in the concentration trapped on the  $r$ th trap is:

$$dC_r = \frac{(T_r - C_r)dC}{B + \sum(T_r - C_r) + \sum C_r + C_b};$$

$$\therefore \frac{dC_r}{dC} = \frac{(T_r - C_r)}{B + C_b + \sum T_r} \quad \dots \dots \dots (1)$$

Similarly

$$\frac{dC_b}{dC} = \frac{B}{B + C_b + \sum T_r} \quad \dots \dots \dots (2)$$

Hence

$$C_b = (B + \sum T_r) \left\{ \left[ 1 + \frac{2BC}{(B + \sum T_r)^2} \right]^{1/2} - 1 \right\} \quad \dots \dots (3)$$

Solving (1) we obtain for  $C_r$

$$C_r = T_r \left[ 1 - \exp \left( - \frac{C_b}{B} \right) \right] \quad \dots \dots \dots (4)$$

Now if the resistivity change due to interstitials being trapped on the  $r$ th trap is  $a_r C_r$  and that due to a concentration  $V$  of vacancies is  $bV$ , then we may write for the resistivity increase:

$$\Delta\rho = \sum a_r C_r + \sum b C_r + b C_b$$

or

$$\Delta\rho = b \left\{ \left[ 1 - \exp \left( - \frac{C_b}{B} \right) \right] \sum T_r \left( 1 + \frac{a_r}{b} \right) + C_b \right\} \quad \dots \dots (5)$$

In this expression the first set of terms, arising from the trapped interstitials and their associated vacancies, saturate with the same period as  $C$  increases. The term  $bC_b$  which is due to the vacancies left behind by interstitials lost to boundaries, shows slight deceleration without saturation.

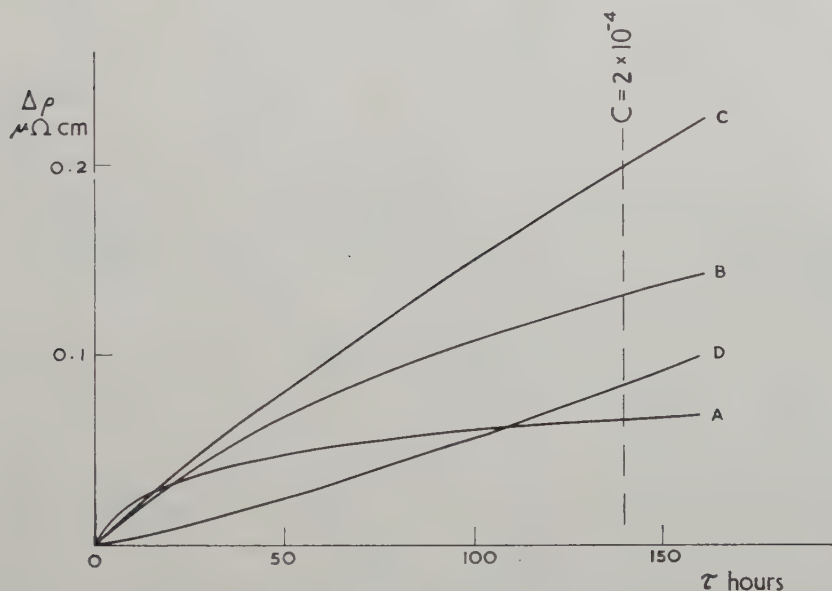
Let us apply this analysis to predict the resistivity increase of an annealed sample of tungsten. First the relation, between  $C$  and irradiation time may be established as:

$$C = n\sigma\phi \quad \dots \dots \dots (6)$$

Where  $n$  is the number of interstitial-vacancy pairs per neutron hit,  $\sigma$  is the total fast neutron cross section ( $\sim 10^{-23} \text{ cm}^2$ ),  $\phi$  is the fast neutron flux ( $\sim 3 \times 10^{11} \text{ neutron cm}^{-2} \text{ sec}^{-1}$ ), and  $\tau$  is the irradiation time. Taking  $n$  as 30 the value of  $C$  is of the order  $10^{-4}$  for a 140-hour irradiation.

The concentration of traps,  $\sum T_r$ , may be estimated as follows; the residual resistivity of the tungsten suggests an impurity concentration of  $10^{-4}$ , assuming the reasonable value of 500 microhm cm per unit concentration of impurities. This concentration is not in contradiction with the spectrographic analysis. Those traps which are due to impurities will have this order of concentration. Dislocations might also provide traps, a density of  $10^{10}$  lines  $\text{cm}^{-2}$  producing a concentration of order  $10^{-4}$  if ten trapping sites exist in each atomic plane, pierced by a dislocation. It would appear then that  $10^{-4}$  is a reasonable value for  $\sum T_r$ .

Fig. 7



Resistance increase as a function of irradiation time calculated from theory for A, B, C and D type specimens with the sink concentrations given in table 2.

The value of  $B$ , the effective concentration of permanent sinks, will depend primarily on grain size. An order of magnitude may be obtained as the ratio of lattice sites at the grain surface to the total of sites in the grain

$$\text{i.e. } B \sim 6/dA^{1/3}$$

where  $d$  is the linear grain size and  $A$  the density of atoms. For 10 micron grains  $B$  is of the order of  $10^{-4}$ .

In previous work (Kinchin and Thompson 1958) a value of  $2 \times 10^3$  microhm cm was deduced for the resistivity increase in molybdenum per unit concentration of interstitials and vacancies. For the purposes of the present order of magnitude calculation let us take  $a_r = b = 10^3$  microhm cm

for tungsten which behaves similarly to molybdenum. We may then sketch  $\Delta\rho$  as a function of  $C$  for specimen types A, B and C as in fig. 7 using the estimates of table 2.

Table 2. Estimated Sink Concentrations ( $\times 10^4$ ) for Four Types of Specimen

Type	B	$\Sigma T_r$	$T_1$	$V_0'$	Temp. of annealing °C
A	0.05	0.20	0.05	0	2000
B	0.50	0.30	0.15	0	1500
C	5.00	1.00	—	0	500
D	5.00	1.00	—	2.00	None

A comparison of the curves in fig. 7 with the results of fig. 4 shows that the theory explains the qualitative effects and gives the correct order of magnitude of the resistivity change. Expressed in physical terms, an increase in grain size favours both the trapping process and annihilation of vacancies. Consequently there is a greater tendency to saturate and a greater initial rate of increase.

In the publication referred to above, the change in resistivity of tungsten irradiated at 30°C was reported to show an initial deceleration up to 5 weeks irradiation followed by steady rise. Here again there is agreement with the behaviour of the two terms in eqn. (5) the first of which might be expected to saturate after about five weeks' irradiation.

Let us now consider the resistivity increase in cold-worked tungsten. The acceleration with irradiation time suggests that there is a process occurring simultaneously with the accumulation of vacancies and trapped interstitials, which causes a decrease in resistivity. This process might be the action of spikes on unstable defect configurations produced by cold-work. For instance it has been suggested that vacancies are produced in strings during cold-work (Cottrell 1957) and the effect of a spike on such an array might well be to cause aggregation with an associated decrease in resistivity.

Suppose that such a process occurs and that one spike containing  $S$  atoms is produced per neutron hit. From our previous definition there will be  $n$  interstitials and vacancies associated with each spike. The concentration of spikes is thus  $C/n$  and the concentration of lattice sites affected by spikes is  $SC/n$ . The effect of increasing  $C$  by  $dC$  will be to increase the concentration of spike sites by  $SdC/n$ . If  $V'$  is the concentration of vacancies due to cold work then a concentration  $V'$  of these extra spike sites will be strings of vacancies and the concentration of vacancies aggregated will be:

$$\frac{SV'}{n}dC.$$



The concentration of cold-work vacancies will be further reduced by annihilation with radiation-produced interstitials. We shall neglect the effect of this annihilation on the aggregation process. By an argument analogous to that used above the following equations may be shown to govern the concentrations  $V$ ,  $V'$ ,  $C_r$  and  $C_b$ :

$$\frac{dV}{dC} = \frac{\sum(T_r - C_r) + B + V'}{B + \sum(T_r - C_r) + V + V'}, \quad \dots \dots \dots (6)$$

$$\frac{dV'}{dC} = -\frac{SV'}{n} - \frac{V'}{B + \sum(T_r - C_r) + V + V'}, \quad \dots \dots \dots (7)$$

$$\frac{dC_r}{dC} = \frac{T_r - C_r}{B + \sum(T_r - C_r) + V + V'}, \quad \dots \dots \dots (8)$$

$$\frac{dC_b}{dC} = \frac{B}{B + \sum(T_r - C_r) + V + V'}, \quad \dots \dots \dots (9)$$

with the boundary conditions

$$C = 0; \quad V = C_r = C_b = 0$$

and  $V' = V'_0$ .

A numerical solution of these equations has been obtained for the case of cold-worked tungsten using the values of  $V'_0$ ,  $B$  and  $\sum T_r$  in table 2, taking  $S$  as  $10^5$  and  $n$  as 30. The value of  $V'_0$  was deduced from the residual resistivity difference of type  $C$  and  $D$  specimens. From this solution  $\Delta\rho$  has been calculated as a function of  $C$  and values are shown in fig. 7. The predicted acceleration with  $C$  is in agreement with the observations recorded in fig. 6.

#### 4.2. Recovery

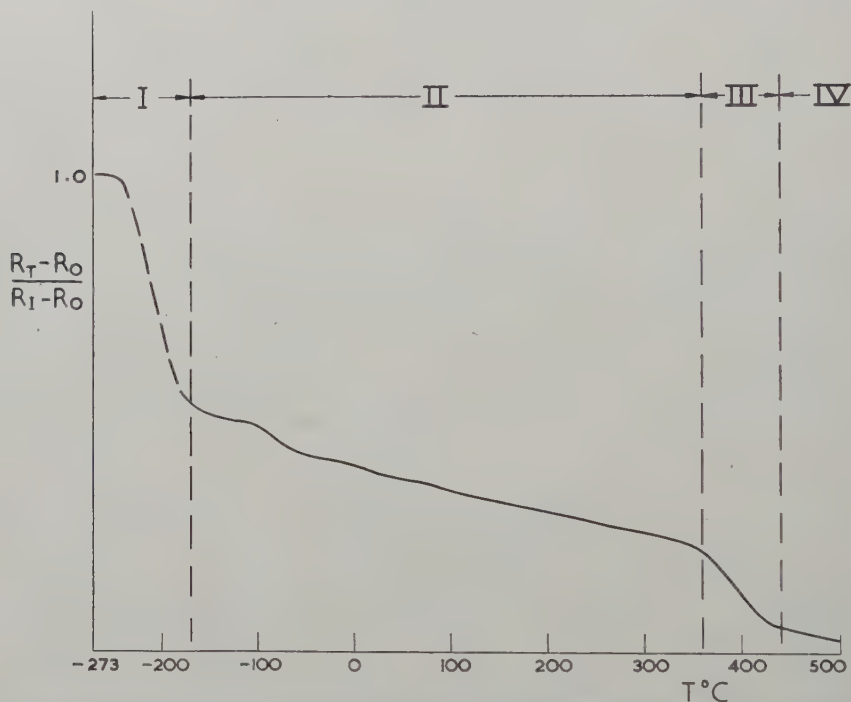
Blewitt (private communication) has shown that tungsten irradiated at 20°K for 1 week in the Oak Ridge pile recovers about 50% of its resistivity increase after annealing at liquid nitrogen temperature. Since this is in substantial agreement with the tungsten irradiated at low temperatures for 8 min it appears that the effect of dose on this part of the recovery curve is small. An approximate recovery curve between 4°K and 500°C for a 140-hour irradiation may then be sketched as in fig. 8. Recovery below -170° has been designated stage I, that between -170 and 350°C as stage II, that between 350 and 450°C as stage III and above 450°C as stage IV.

Previous work (Kinchin and Thompson 1958) has shown that activation energies in stage II rise from 0.25 to 1.7 ev and that stage III proceeds at 1.7 ev.

Recovery curves of this type have been observed in other metals, the difference being that in some cases, notably gold, stage I is absent (Cooper *et al.* 1954) and that in the case of electron irradiation stage II is greatly reduced (Corbett *et al.* 1957). However, in all reported cases of irradiated, quenched or cold-worked metals stages III occurs at an absolute temperature roughly 20% that of the melting point. Table 3 lists some typical activation energies and temperatures for stage III in Ag, Al, Au, Cu, Mo, Nb, Ni, Pt. and W.

It will be noticed that the ratio of activation energy to absolute melting temperature varies little with the type of damage in a given metal or from element to element. It has long been established that such a relation exists between self diffusion activation energies (Kidson and Ross 1957) where vacancy formation and migration is the common mechanism. This suggests that the same stage III recovery mechanism operates after irradiation, cold work or quenching and that this mechanism is the same for all the above metals.

Fig. 8



A schematic recovery curve for annealed tungsten after a 140-hour irradiation at 4°K.

Since stage III recovery after quenching is generally attributed to the migration of vacancies (Koehler *et al.* 1957) it is assumed that this is also the case in irradiated and cold-worked material. In particular, let us attribute stage III in tungsten to vacancy migration.

In order to explain the low temperature recovery it is necessary to postulate that interstitial migration occurs either in stage I or at some even lower temperature. For the purposes of this discussion let us assign stage I to interstitial migration.

Specimen types C and D have the same grain size and impurities and should have roughly the same dislocation density. Type D, however,

Table 3

Metal	$T_m$ °K	Damage	$E$ ev	$T$ °K	$\frac{E}{T_m} \times 10^4$	$\frac{T}{T_m}$	Reference
Ag f.c.c.	1234	C.W.	0.65	230	5.3	0.17	Manintveld 1952
Al f.c.c.	933	Irrad.	0.55	190	5.9	0.20	McReynolds <i>et al.</i> 1955
		Quench	0.44	300	4.7	0.32	Bradshaw and Pearson 1957 b
		Quench	0.52	270	5.6	0.30	de Sorbo and Turnbull 1959
Au f.c.c.	1336	C.W.	0.69	290	5.2	0.22	Manintveld 1952
		Quench	0.82	310	6.1	0.23	Baurle and Koehler 1957
		Quench	0.68	370	5.1	0.28	Bradshaw and Pearson 1957 a
Cu f.c.c.	1356	Irrad.	0.68	250	5.0	0.19	Overhauser 1955
		C.W.	0.67	230	5.0	0.17	Eggleston 1952
Mo b.c.c.	2893	Irrad.	1.3	420	4.5	0.15	Kinchin and Thompson 1958
		C.W.	1.26	430	4.4	0.15	Martin 1957
Nb b.c.c.	2220	Irrad.	1.3	420	5.9	0.19	Makin 1959
Ni f.c.c.	1728	C.W.	1.0	500	5.8	0.28	Nicholas 1955
Pt f.c.c.	2047	Irrad.	1.2	420	5.9	0.21	Dugdale 1952
		Quench	1.1	570	5.4	0.29	Bradshaw and Pearson 1956
W b.c.c.	3643	Irrad.	1.7	670	4.7	0.18	Kinchin and Thompson 1958
		C.W.	1.7	620	4.7	0.17	Schultz 1959

has an initial concentration of vacancies formed during deformation. The recovery curves of fig. 2 show that the effect of these vacancies is to enhance stage II recovery. This is evidence that stage II is in some way associated with interstitial migration resulting in vacancy annihilation.

It was pointed out in an earlier publication (Thompson 1958 a) that the absence of stage II in lightly irradiated tungsten may be explained by assuming that this stage is due to the thermal activation of interstitials from traps in the lattice. After a one hour irradiation  $C \sim 10^{-6}$  whereas  $\sum T_r \sim 10^{-4}$ . Under these conditions interstitials being activated from

the shallowest traps will become attached to deeper traps rather than annihilating the small concentration of vacancies present. Provided that the resistivity change associated with those interstitials which reach boundaries is balanced by that due to interstitials changing traps there will be no net recovery observed. In the case of type E specimens, which have a different set of impurities, the presence of stage II recovery after light irradiations might indicate that the decrease in resistivity due to migration to boundaries is not balanced by an increase due to changing traps. If the trapping mechanism of stage II recovery is accepted, then this difference in behaviour between types B and E is clear evidence that impurity atoms are capable of trapping interstitials. A similar conclusion has been reached by Blewitt *et al.* (1957) and Martin (1959, private communication) during studies of neutron-irradiated doped copper. The role of dislocations in recovery is not obvious from the experimental results, owing to simultaneous changes in grain size, but will be considered in the analysis which follows.

Using the three postulates of § 4.1 let us develop a quantitative theory of stage II recovery for comparison with the experimental observations. In order to simplify the analysis the following substitutions will be made:

$$x = \frac{C_b}{B},$$

$$t = 1 + \frac{\sum T_r}{B},$$

$$E = 1 - \exp(-x).$$

It follows from eqns. (3) and (4) that after irradiation the following concentrations of sinks for interstitials will be present:

$$\text{Vacancies:} \quad B(x + (t-1)E),$$

$$\text{Unfilled traps:} \quad B(t-1)(1-E),$$

$$\text{Boundary sinks:} \quad B;$$

$$\therefore \text{total concentration of sinks} = B(t+x).$$

Now suppose that the temperature of the specimen is raised sufficiently to liberate the interstitials from the first trap ( $T_1$ ) and that these constitute a small proportion of the total number of trapped interstitials, i.e.

$$T_1 = \alpha \sum T_r,$$

The total concentration of released interstitials is found from eqn. (4) as

$$\alpha B(t-1)E.$$

Then the concentration of these which annihilate vacancies is

$$\alpha B(t-1)E \left[ \frac{x + (t-1)E}{t+x} \right]$$



the concentration going to the  $r$ th unfilled trap ( $r \neq 1$ ) is

$$\alpha B(t-1)E \left[ \frac{(1-E)(t_r-1)}{t+x} \right], \quad t_r = 1 + \frac{T_r}{B}$$

and the concentration lost to boundaries is

$$\alpha B(t-1)E \left[ \frac{1}{t+x} \right].$$

Now  $(a_1+b)$  is the resistivity change due to unit concentration of released interstitials annihilating vacancies.  $a_1$  is that due to unit concentration migrating to boundaries and  $(a_1-a_r)$  is that due to unit concentration becoming trapped on the  $r$ th type of trap. The net recovery of resistivity is then

$$(\Delta\rho)_1 = -\frac{\alpha B(t-1)E}{t+x} \{ (a_1+b)(x+(t-1)E) + \sum (t_r-1)(a_1-a_r)(1-E) + a_1 \}.$$

The total change in resistivity due to irradiation is given by eqn. (5). We may therefore write the proportion of recovery due to interstitials being released from trap 1 as

$$\frac{(\Delta\rho)_1}{\Delta\rho} = -\frac{\alpha(t-1)E}{t-x} \frac{[1+a_1/b](x+(t-1)E) + \sum (t_r-1)(a_1-a_r/b)(1-E) + a_1/b}{E \sum (t_r-1)[1+a_r/b] + x}. \quad (7)$$

From experiment it is known that for A and B type specimens recovery is zero for small doses, i.e.

$$\frac{(\Delta\rho)_1}{\Delta\rho} \rightarrow 0 \quad \text{as } x \rightarrow 0.$$

Putting this condition into eqn. (7) we conclude that

$$\sum (t_r-1)(a_1-a_r) = -a_1, \text{ in A and B type specimens.} \quad (8)$$

In physical terms, the resistivity change due to released interstitials migrating to boundaries is compensated by that due to changing traps. Under these special circumstances equation (7) becomes:

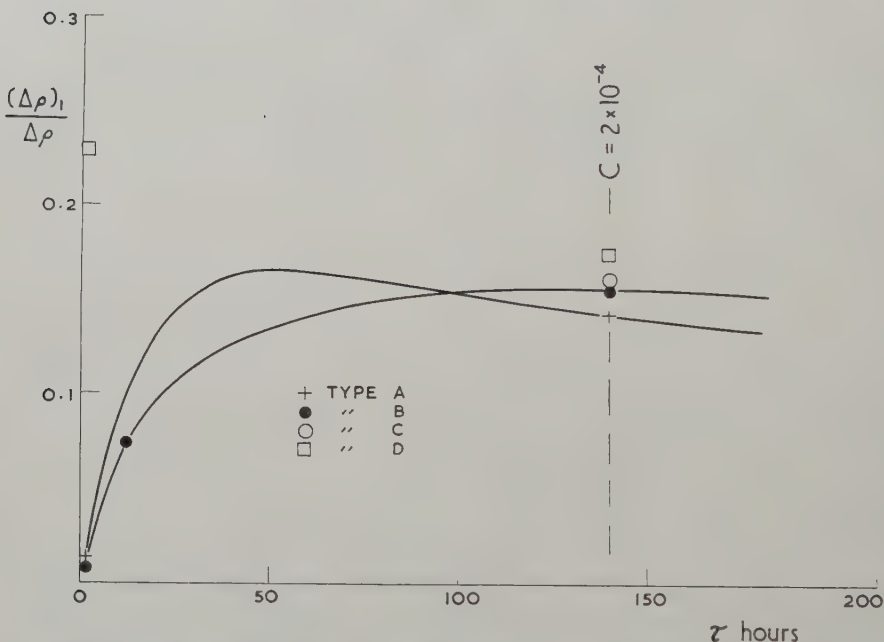
$$\frac{(\Delta\rho)_1}{\Delta\rho} = \frac{\alpha(t-1)E}{t+x} \frac{[1+a_1/b](x+(t-1)E) + (a_1/b)E}{\sum (t_r-1)[1+a_r/b]E + x}. \quad (7a)$$

In fig. 9 observed values of  $(\Delta\rho)_1/\Delta\rho$  for the recovery occurring between  $-120$  and  $-40^\circ\text{C}$  are plotted as a function of irradiation time for A, B, C and D type specimens. The expression (7a) has been made to agree with the type A and B experimental points at 140 hours by choosing suitable values for  $T_1$ . It will be seen that the remaining points then fall on the theoretical curves. This indicates that the theory predicts at least the correct functional dependence of recovery on irradiation time. The selected values of  $T_1$  are shown in table 2 and it will be noticed that there is a factor of 3 between the values for specimen types A and B. Because

the coefficients  $a_r$  are unknown for types *C* and *D* and because there is no simplifying relation like (8), it is not possible to tabulate the expression (7) for these other specimens.

Let us now consider the evidence for traps being associated with dislocation lines. The theoretical curves of resistance increase were obtained by assuming a decrease in  $\sum T_r$  with increasing pre-irradiation annealing temperature. The temperatures involved strongly suggest that part of the trap concentration follows the dislocation density with the implication that dislocations provide trapping sites. The further fact that  $T_1$  varies with pre-irradiation annealing temperature in a similar way, strengthens this suggestion.

Fig. 9



Recovery between  $-120$  and  $-40^\circ\text{C}$  as a function of irradiation time: the solid lines represent theoretical curves which have been fitted to the observations at  $\tau = 140$  using the sink concentrations given in table 2.

#### 4.3. Summary of Conclusions

A quantitative theory which is consistent with the experimental facts may be derived from the following postulates:

1. Interstitials and vacancies are produced by irradiation in equal numbers.
2. Interstitials are mobile at  $77^\circ\text{K}$ , stage I recovery between  $4^\circ\text{K}$  and  $77^\circ\text{K}$  being tentatively assigned to interstitials first becoming mobile.

3. Vacancies become mobile between 350°C and 450°C and this mechanism is responsible for stage III recovery.
4. Three types of sink compete for interstitials :
  - (a) Vacancies.
  - (b) Grain boundaries.
  - (c) Traps.

Thermal activation of interstitials from traps is responsible for stage II recovery (– 196 to 350°C). These traps are associated both with impurities and dislocations, the concentration depending on pre-irradiation annealing treatment.

5. Irradiation produces spike regions of temporary disorder containing  $10^5$  atoms.
6. Cold-work produces vacancies in strings and the action of spikes on these is to cause aggregation.

#### ACKNOWLEDGMENTS

I should like to thank Miss J. Stubbs for her invaluable assistance throughout this work and Dr. T. H. Blewitt and Mr. D. G. Martin for permission to refer to unpublished work.

#### List of Symbols

$R_0$  = resistance of specimen before irradiation.

$R_I$  = resistance of specimen after irradiation.

$R_T$  = resistance of specimen after annealing for 30 min at T°C.

$\tau$  = Irradiation time.

$n$  = the number of interstitials and vacancies per neutron hit.

$S$  = the number of atoms affected by a spike.

$C$  = total concentration of interstitials and vacancies produced.

$C_r$  = total concentration of interstitials on the  $r$ th trap.

$C_b$  = total concentration of interstitials lost to boundaries.

$V$  = total concentration of vacancies present due to irradiation.

$V'$  = total concentration of vacancies present due to cold work  
(initial value  $V'_0$ ).

$T_r$  = total concentration of traps of the  $r$ th type.

$B$  = total concentration of boundary sinks.

$a_r$  = resistivity due to unit concentration of interstitials on the  $r$ th trap.

$b$  = resistivity due to unit concentration of vacancies.

$x = C_b/B$ .

$t_r = 1 + T_r/B$ .

$t = 1 + \sum T_r/B$ .

$\alpha = T_1/\sum T_r$ .

$E = 1 - \exp(-x)$ .

## REFERENCES

- BAURLE, J. E., and KOEHLER, J. S., 1957, *Phys. Rev.*, **107**, 1493.  
 BLEWITT, T. H., COLTMAN, R. R., KLABUNDE, C. E., and NOGGLE, T. S., 1957, *J. appl. Phys.*, **28**, 639.  
 BRADSHAW, F. J., and PEARSON, S., 1956, *Phil. Mag.*, **1**, 812; 1957 a, *Ibid.*, **2**, 379; 1957 b, *Ibid.*, **2**, 570.  
 COOPER, H. C., KOEHLER, J. S., and MARX, J. W., 1954, *Phys. Rev.*, **94**, 496.  
 CORBETT, J. W., DENNEY, J. M., FISKE, M. D., and WALKER, R. M., 1957, *Phys. Rev.*, **108**, 954.  
 COTTRELL, A. H., 1957, *Symposium on Point Defects* (London: Inst. of Metals), p. 26.  
 DUGDALE, R. A., 1952, *Phil. Mag.*, **43**, 912.  
 EGGLESTON, J., 1952, *J. appl. Phys.*, **23**, 1400.  
 GONSER, U., and OKKERSE, B., 1958, *Phys. Rev.*, **109**, 663.  
 KIDSON, G., and ROSS, R., 1957, Conf. sur l'utilisation des radioisotopes dans la recherche Scientifique, UNESCO/NS/RIG/216.  
 KINCHIN, G., and THOMPSON, M. W., 1958, *J. nucl. Energy*, **6**, 275.  
 KOEHLER, J. S., SEITZ, F., and BAURLE, J. E., 1957, *Phys. Rev.*, **107**, 1499.  
 LOMER, W. M., and COTTRELL, A. H., 1955, *Phil. Mag.*, **46**, 711.  
 McREYNOLDS, A. W., AUGUSTYNIAK, W., McKEOWN, M., and ROSENBLATT, D. B., 1955, *Phys. Rev.*, **94**, 1417.  
 MAKIN, M. J., 1959, *Acta Met.*, **7**, 361.  
 MANINTVELD, J. A., 1952, *Nature, Lond.*, **169**, 623.  
 MARTIN, D. C., and STANWIX, P., 1956, U.K. Atomic Energy Authority report, AERE-M/M-138; 1957, *Acta Met.*, **5**, 371.  
 NICHOLAS, J. F., 1955, *Phil. Mag.*, **46**, 88.  
 OVERHAUSER, A. W., 1955, *Phys. Rev.*, **90**, 393.  
 SCHULTZ, H., 1959, *Z. Naturf.*, **14**, 4, 361.  
 DE SORBO, W., and TURNBULL, D., 1959, *Acta Met.*, **7**, 83.  
 STUBBS, M. J., and THOMPSON, M. W., 1958, *J. sci. Instrum.*, **35**, 68.  
 THOMPSON, M. W., 1958 a, *Phil. Mag.*, **3**, 28, 421; 1958 b, *J. sci. Instrum.*, **34**, 515.  
 THOMPSON, M. W., and JEFFERSON-LOVEDAY, D. W., 1958, *J. sci. Instrum.*, **35**, 397.



## CORRESPONDENCE

# A Possible Example of the Muon Radiative Decay with Internal Conversion of the $\gamma$ -ray

By VALERIE MAYES

H. H. Wills Physical Laboratory, University of Bristol

[Received March 30, 1960]

IN making an area scan for  $\pi$ - $\mu$ -e, in a stack which had been exposed to the cosmic rays at an altitude of approximately 13 kilometres, an event was found (Pl. 33) in which three relativistic electrons escaped from the decay of a  $\mu$ -meson at rest. A similar event has been observed by I. I. Gurevich *et al.* (1959). The nature of the  $\mu$ -meson was established from its origin and from its range,  $613\mu$ . (The average range for  $\mu$ -mesons from  $\pi$ - $\mu$  decay in G5 emulsion is  $595\mu$ .) The pair and positron tracks dipped steeply down into the emulsion at angles to the emulsion plane of approximately  $70^\circ$  and  $45^\circ$  respectively. It was not possible to follow the electron tracks in more than one emulsion because the stack consisted of alternate layers of  $600\mu$  emulsion and 1.6 mm tungsten. The recorded track lengths were  $Le_1 = 188\mu$ ,  $Le_2 = 186\mu$ ,  $Le_3 = 242\mu$ . The short length of the tracks and their steepness made energy determinations difficult. Apparent values for the energy of the pair and of the positron were obtained from scattering measurements, these gave

$$E_{\text{pair}} = 40 \pm 16 \text{ mev,}$$

$$E_{\text{positron}} = 18 \pm 5 \text{ mev.}$$

From the opening angle of the pair an estimate of  $E_{\text{pair}}$  of approximately 25 mev was obtained. The angles between the tracks are

$$\psi_{e_1 e_2} \sim 5^\circ, \quad \psi_{e_1 e_3} \sim 60^\circ, \quad \psi_{e_2 e_3} \sim 58^\circ.$$

Since the electron tracks are not coplanar and the directions of the pair and of the positron are not collinear, the event cannot be identified with either  $\mu \rightarrow 3e$  or  $\mu \rightarrow e + \gamma$  with subsequent conversion of the  $\gamma$ -ray. The event can be identified, however, with either (1)  $\mu^+ \rightarrow e^+ + (e^+ + e^-) + \nu + \bar{\nu}$  or (2) the coincidence of a converting  $\gamma$ -ray with the decay point of a  $\mu$ -meson. The probability of radiative decay has been assessed by N. Tzoar and A. Klein (1958) as  $10^{-5}$  per  $\mu$ -meson and hence that of (1) is of the order of  $10^{-7}$  per  $\mu$ -meson. The probability of finding a back-ground electron pair within 10 cubic microns of the  $\mu^+$  decay was determined from the density of  $\pi^+$  in the emulsion and was of the order of  $10^{-9}$  per

$\mu$ -meson, i.e. several orders of magnitudes smaller than the theoretical probability of radiative decay with internal conversion. In order to check that this did not underestimate the probability of coincidence, an area scan for electron pairs was made. This showed that the density of pairs was not greater than the density of  $\pi^+$  (400 per  $\text{cm}^3$ ) in the vicinity of this event.

The probability of a positron producing an electron pair, either by conversion of bremsstrahlung or by trident production (i.e. direct pair production in the field of a nucleus), in the first few microns of its path after normal  $\mu$  decay, is of the same order of magnitude as the probability of radiative decay with internal conversion. In this event, however, the positron and electron pair were separated by approximately  $60^\circ$  and in the above two processes, at this energy, the electrons would be collimated within a few degrees. In the event observed by Gurevich *et al.* the pair and positron were indistinguishable, all three tracks lying within approximately  $10^\circ$  of one another.

#### ACKNOWLEDGMENTS

It is my pleasure to thank Professor C. F. Powell for the facilities of this laboratory. I am indebted to Dr. D. H. Perkins and Dr. P. H. Fowler who interpreted this event and to Dr. K. Pinkau for helpful advice. Mr. W. Harbor photographed the event and I am grateful to him for his skill and patience. My thanks are due to D.S.I.R. for a maintenance grant.

#### REFERENCES

- GUREVICH, I. I., *et al.*, 1959, *J. exp. theor. Phys.*, **37**, 318 (translation, *Soviet Phys.*, **37**, 225, 1960).  
TZOAR, N., and KLEIN, A., 1958, *Nuovo Cim.*, **8**, 482.

---

### Direct Electron Microscopy of Thin Foils of Internally Oxidized Dilute Copper Alloys

By M. F. ASHBY and G. C. SMITH

Department of Metallurgy, University of Cambridge

[Received February 26, 1960]

SEVERAL workers (Bollman 1956, Hirsch *et al.* 1956, Nicholson *et al.* 1957, Nicholson and Nutting 1958, Whelan *et al.* 1957) have developed techniques for examining thin metal foils by direct electron transmission. This paper describes the application of these techniques to the examination of an internally oxidised copper 0.25% aluminium alloy. The authors have obtained electron micrographs which show the internal oxide particles in the copper matrix and the interaction of dislocations with these particles.

This alloy, rolled to a strip 200 microns thick, was internally oxidized by placing it in cuprous oxide and heating for 20 min at 950°C, producing a dispersion of alumina in a pure copper matrix. Electron diffraction of electropolished specimens, using a reflection technique, showed the dispersion to be of  $\gamma$  high temperature alumina. This analysis was confirmed by preparing carbon extraction replicas from the specimen surface, and photographing diffraction patterns from them, using a selected area electron diffraction technique.

Satisfactory foils of this internally oxidised strip were obtained by using the Bollman (1956) technique. The bath used was a methyl alcohol: concentrated nitric acid mixture in the proportion 2 : 1, at a potential of 9 volts and a temperature of -20°C. Figure 1 (Pl. 34) is an electron micrograph of a foil of an unstrained specimen produced in this way. Many of the alumina particles, of diameter about 300 Å, are clearly defined as triangular plates or tetrahedra, and there is evidence of precipitation along preferred planes in the copper matrix. Pronounced contrast effects can be seen around the particles in the twin, where the lattice orientation is favourable for diffraction contrast. Two explanations in terms of strain fields are possible. Firstly, Nicholson and Nutting (1958) have shown that coherency strains can give rise to this type of strain pattern, so the alumina particles may be coherent with the copper matrix; attempts to fit the alumina and copper lattices to allow coherency have so far proved unsatisfactory. Secondly, while the material is cooling after the internal oxidation process, the considerable difference in coefficient of thermal expansion of copper and alumina must produce strain fields around the particles. This second explanation seems the more probable one. The dark rings surrounding some of the particles in fig. 1 are due to carbon contamination of the foil in the microscope; carbon builds up round particles which project from the surface of the foil.

Other foils, also internally oxidized, were strained in tension by amounts varying from 0.5 to 6.0%. From among these foils, two, strained 4%, have been selected for illustration (figs. 2 and 3, Pl. 34).

Dislocations are visible in fig. 2 bowed out between points where alumina particles prevent their movement. At first sight this pattern of dislocations seems consistent with Orowan's theory of hardening of metal by a dispersed phase (Orowan 1947). The foil is of the order of 1000 Å thick, so that any one particle will not intersect all the slip planes in the plane of the foil. However, by measuring the distance apart ( $2R$ ) of particles between which a single dislocation is bowing out, an estimate of the yield stress ( $\sigma$ ) of the material can be calculated, using the relationship:

$$\sigma = \frac{\alpha G b}{R}$$

(where  $\alpha$  is a constant approximately equal to  $\frac{1}{2}$ ;  $G$  is the shear modulus

of the matrix; and **b** is the Burgers vector of the dislocation.) The mean calculated yield stress was  $1.4 \times 10^4$  p.s.i. The measured yield stress was  $1.58 \times 10^4$  p.s.i.

Heavily jogged dislocations and triangular dislocation loops attached to particles can be seen in fig. 3. These loops have not collapsed onto the particles, but bow out from them. A stable configuration such as that seen in fig. 3 can be explained by supposing the loops to be prismatic, i.e. that all parts of the loop do not lie in the same slip plane. The authors have used a modification of Orowan's theory first proposed by Hirsch (1957) to explain the formation of these loops. This is illustrated schematically in fig. 4.

Fig. 4



In 1 a pure edge dislocation, moving in the direction of its Burgers vector (**b**), has been held up by a set of particles intersecting the slip plane. As the applied stress rises, the screw components of the dislocation, formed when the dislocation took up the shape shown in 1, cross slip, as shown in 2. These screw components are of opposite sign on each side of a single particle; they attract each other, as in 3; and annihilate each other, as in 4. The process leaves a prismatic loop round each particle and corresponding prismatic jogs in the dislocation line. The loops can move on the surface of a cylinder whose axis is parallel to the Burgers vector, but they cannot collapse completely. This diagram shows the simplest form of this type of interaction. Any dislocation with an edge component should behave in a similar way.



A prediction from this mechanism is that the direction of elongation of the loops projected on to a slip plane will be parallel to a slip direction in the matrix metal. This prediction could be checked by electron diffraction experiments: these have not yet been tried. Inspection of fig. 3 shows that the loops appear to have a common direction of elongation.

## ACKNOWLEDGMENT

The authors are indebted to Dr. P. B. Hirsch and Dr. A. Kelly for many helpful discussions and to Mr. R. S. M. Revell for his help in obtaining the electron micrographs. All electron micrographs were taken on a Metropolitan-Vickers E.M.6.

## REFERENCES

- BOLLMANN, W., 1956, *Phys. Rev.*, **103**, 1588.  
HIRSCH, P. B., 1957, *J. Inst. Met.*, **86**, 13.  
HIRSCH, P. B., HORNE, R. W., and WHELAN, M. J., 1956, *Phil. Mag.*, **1**, 677.  
NICHOLSON, R. B., THOMAS, G., and NUTTING, J., 1957, *Brit. J. appl. Phys.*, **9**, 25.  
NICHOLSON, R. B., and NUTTING, J., 1958, *Phil. Mag.*, **3**, 531.  
OROWAN, E., 1947, Discussion, *Symposium on Internal Stresses* (London: Inst. Metals).  
THOMAS, G., NUTTING, J., and HIRSCH, P. B., 1957, *J. Inst. Met.*, **86**, 7.  
WHELAN, M. J., HIRSCH, P. B., HORNE, R. W., and BOLLMANN, W., 1957, *Proc. roy. Soc.*, **240**, 525.

## REVIEWS OF BOOKS

*Manual of Mathematical Physics.* By PAUL I. RICHARDS. (London : Pergamon, 1960.) [Pp. 486.] £5 10s. 0d.

Most dictionaries of mathematics or physics are useless: the topics are too intimately linked in logical chains; a single word, or phrase, cannot be pulled out and discussed in isolation; it carries with it strands of meaning connected with every other word in the list. This Manual is something different—it is a cryptic summary of the most important subjects in Mathematical Physics, more or less logically derived. It might be, as it were, the notes one prepares before an examination, reminding one of all the formulae and their relations, without going into all the rigorous details. The idea is a good one, and it seems to have been undertaken very conscientiously. Thus, the general pattern is sound, the style is extraordinarily easy for such a condensed work, and all is well indexed and complete with cross references. It is impossible to do more than check one's own field; it seemed sensible though I must admit that there were a few typographical errors in the formulae. The level is that of the well-educated theoretical physicist who is not a specialist in the particular field in which he is seeking guidance. As a work of reference it should be very handy, in a library or in the private collection of the experienced research worker. J. M. Z.

*Fluid Mechanics.* By L. D. LANDAU and E. M. LIFSHITZ. (Pergamon Press, 1960.) [Pp. xii+536.] £5 5s. 0d.

THIS book provides a concise and, on the whole, clear account of the fundamental physical phenomena associated with the mechanics of moving fluids. The structure of fluids is not considered, except in so far as it determines the macroscopic variables of state and the various transport coefficients of mass, momentum and energy. It is written from the standpoint of the theoretical physicist, and little mention is made of many aspects of fluid mechanics related to phenomena of geophysical and engineering interest. Not much space is devoted to the detailed solution of particular problems or the presentation of empirical results, except where these illuminate the topics. On the other hand, there are accounts of subjects, such as thermal diffusion, geometrical acoustics, relativistic fluid mechanics, and the dynamics of superfluids, which are not usually included in treatises on fluid mechanics.

The book starts with the motion of an ideal, but not necessarily uniform, fluid, and this is followed by accounts of the motion of a viscous fluid, turbulence, and boundary layers. These first four chapters are not altogether satisfactory, although the good features outweigh the bad. They make very interesting reading for the fluid dynamicist and contain some important new material, in particular a proof that a laminar boundary layer can separate only at a point where the wall stress is zero; but the arrangement of the material is somewhat arbitrary and occasionally the ideas are not presented clearly. There are next three brief chapters on some flows in which temperature gradients, diffusion, and surface effects, are important. These are followed by seven chapters on the motion of a compressible fluid or gas dynamics, which constitute a first class and stimulating account of the subject as it was a few years ago. The book concludes with chapters on relativistic fluid dynamics, the dynamics of superfluids, and fluctuations in fluid dynamics.

This book, although not without some flaws, is a stimulating and welcome addition to the growing list of treatises on fluid mechanics. One serious fault, however, is that it is useless as a bibliography, since only the author and date are given for most of the original papers referred to. P. G. S.

*Quantum Particle Dynamics.* By J. McCONNELL. (North Holland Publishing Company, 1960.) [Pp. 266.] 40s.

THIS second revised edition, appearing only two years after the first edition, is a readable and well presented account of quantum mechanics, quantum field theory and elementary particles. In a book of such short length certain topics have to be left out. This is especially noticeable in the last two chapters on nuclear physics and elementary particles. This may reduce the value of the book for those who wish to understand the modern theory of elementary particles. But it is still a valuable guide to the earlier stages in the development of this theory.

The first half of the book is a detailed discussion of quantum mechanics. Chapter headings show the ground covered: Special Theory of Relativity, Introduction to Quantum Theory, Schrödinger's Wave Mechanics, Heisenberg's Matrix Mechanics, Angular Momentum Systems, of Particles, The Dirac Equation. Then a careful discussion of quantisation of the electromagnetic field is given, and applied to the photoelectric and Compton effects, Bremsstrahlung and Electron Pair Production. Finally in the last two chapters a brief consideration of nuclear forces and an even briefer one of elementary particles is given. The manner in which the topics are discussed makes this book very suitable for undergraduate level. The last two brief chapters should certainly whet the appetite of the interested reader for more detailed discussions of recent work in elementary particle physics.

J. G. T.

*Taylor-Memorial Manual of Advanced Undergraduate Experiments in Physics.* American Association of Physics Teachers (Editor-in-Chief: THOMAS B. BROWN.) (Reading, Mass.: Addison-Wesley, 1959.) [Pp. 550 with 241 line diagrams.] 72s.

THIS manual, dedicated to one of the foremost teachers of experimental physics in the United States, is designed primarily as an aid to those responsible for arranging advanced practical courses in universities and colleges. It is therefore much more a compendium of principles for the teacher than a working text-book for the individual student. The latter type of book is regrettably lacking, at least in Great Britain, and the former non-existent in the reviewer's experience until now. The nearest equivalent in the past would be the series of books on experimental physics by Searle, which had the advantages and disadvantages of their single authorship. The new Manual is a cooperative effort, in which contributions from 191 individual physicists have been co-ordinated and boiled down by a board of eight editors. The result is a mine of information, which any University physics department will do well to quarry, and not least those (not a few) brought up on and still anchored to 'Searle'. Whilst it is true that the basic philosophy of experimental physics can be distilled out of almost any experiment, it is equally true that the individual student's interest is likely to be more readily aroused by examples related to a modern context. Also a considerable number of new practical techniques have come out of modern physics and ought now to find a place in an undergraduate course. It will be helpful to many, for instance, to look through the section on non-linear oscillators, which includes a simple illustration of a relaxation oscillation, and the next section in which servomechanisms are discussed.

All the main branches of physics are covered, the chapters on electricity and magnetism and on nuclear physics being particularly extensive. The former includes microwave optics and the latter a section on health hazards. Inevitably in such an encyclopaedia the level and the detail of treatment vary considerably. Much of the Optics chapter is hardly more than a statement of physical principles, with little in the way of information about apparatus and its setting up. In the chapters on Heat, on Acoustics, and to a lesser extent in

those on Electronics and Atomic Physics, there is much more practical detail. Of intent, however, 'old, familiar experiments' are given little more than a mention and a reference, so as to make space for the less familiar and the new.

The Manual has clearly been a labour of love by the friends and colleagues of Professor L. W. Taylor. In creating such a memorial, they must be congratulated on performing also a valuable service to Physics. It should serve as a guide and reference book to all who are involved in bringing up to date the advanced practical teaching of the subject, and in this instance 'advanced undergraduate' seems indeed to mean the same thing in both Britain and the United States.

V. E. C.

### CORRIGENDA

*Magnetoresistance of Copper, Silver and Gold*, by M. G. PRIESTLEY, 1960, *Phil. Mag.*, **5**, 111.

On p. 114 of this paper the last two lines of the table should read as follows:

[111]	(110)	5	5	6.1
	(211)	6	6	5.3

---

[The Editors do not hold themselves responsible for the views expressed by their correspondents.]

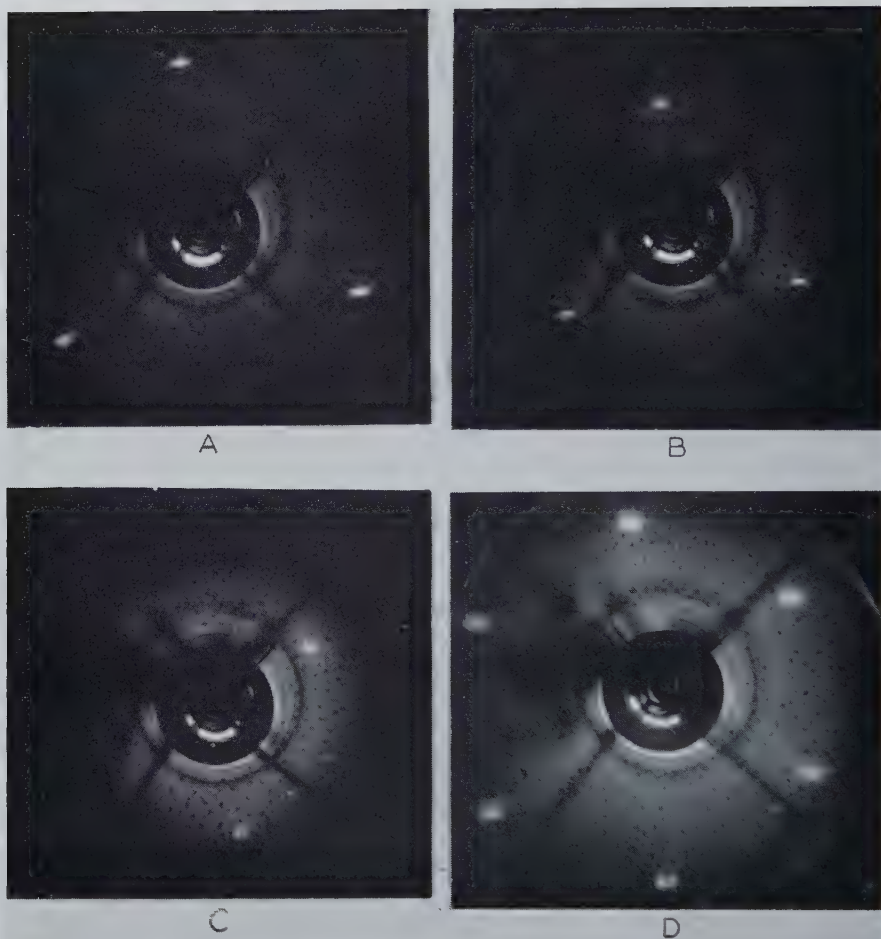


Fig. 2



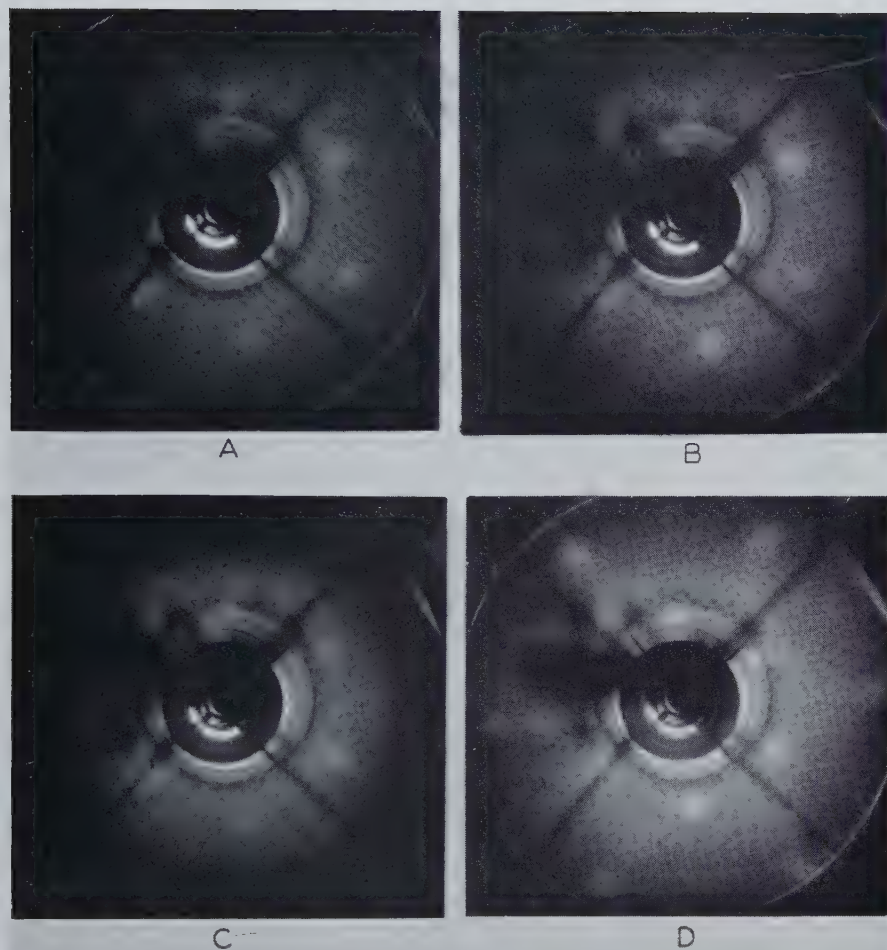
Relative temperature of platinum wire *vs* time when quenched into water.  
The temperature is measured by the resistance of the sample which is proportional to the voltage if the heating current is left on during the quench.

Fig. 2



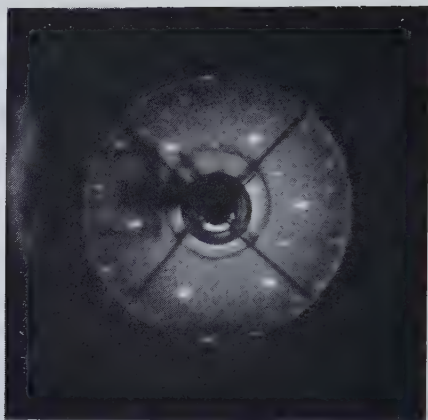
Representative diffraction patterns from the (111) face of a clean nickel crystal (see table 1). (A) (533) reflections at 129 v ; (B) (644) reflections at 200 v ; (C) (466) reflections at 262 v ; (D) reflections in both of the principal azimuths at 120 v.

Fig. 7



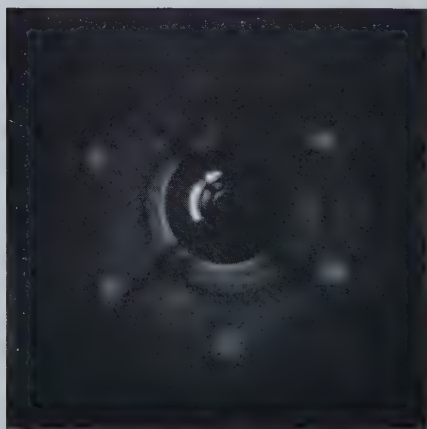
Diffraction patterns representing a monolayer of nitrogen atoms on a (111) nickel surface, arranged in the 4 structure (see table 2). (A) 52 v, diffraction beams strong in B azimuth ; (B) 57 v, diffraction beams strong in A azimuth ; (C) 65 v, diffraction beams strong in B azimuth ; (D) 77 v, diffraction beams in A and B azimuths equally strong.

Fig. 5



Diffraction pattern from unknown material upon crystal, before it had been thoroughly cleaned. Taken at 78 v, 1.39 Å.

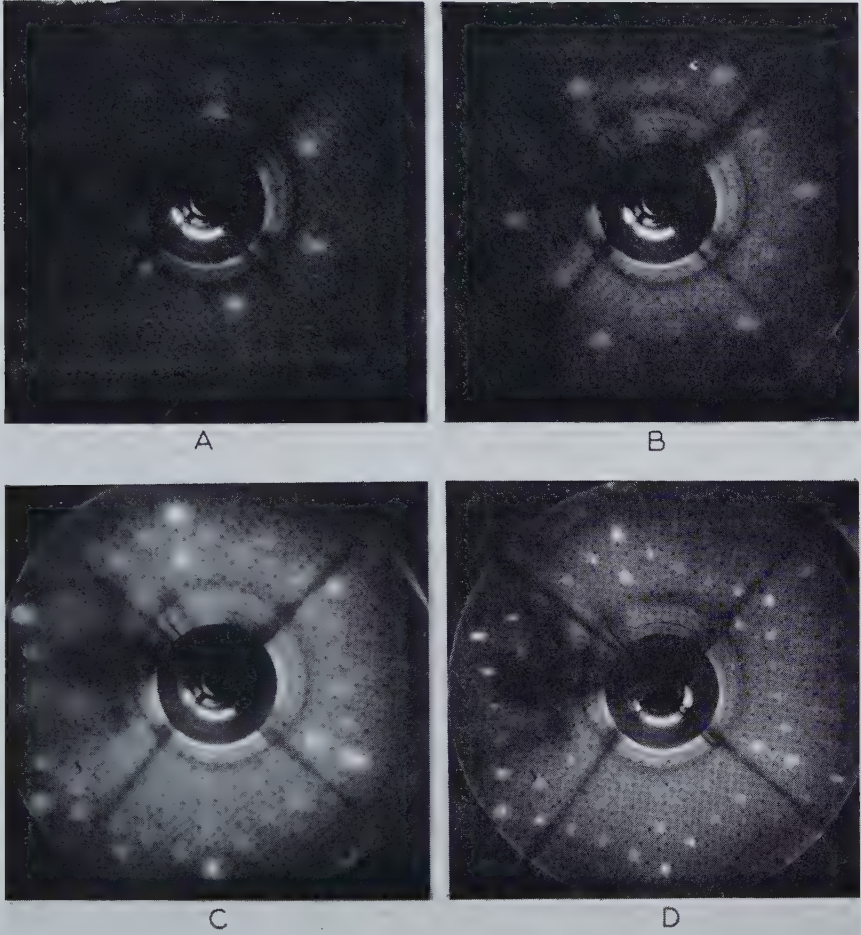
Fig. 8



Diffraction pattern from a monolayer of nitrogen atoms on a (111) nickel face, arranged in the 3 structure. 62 v (see table 2).

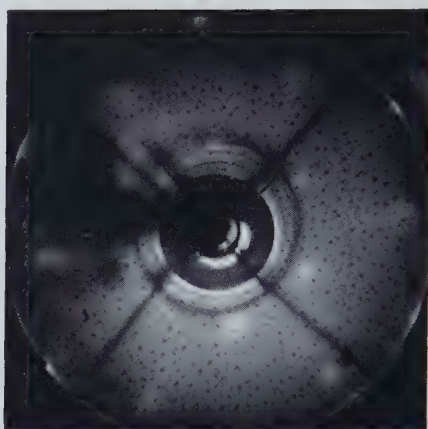


Fig. 9



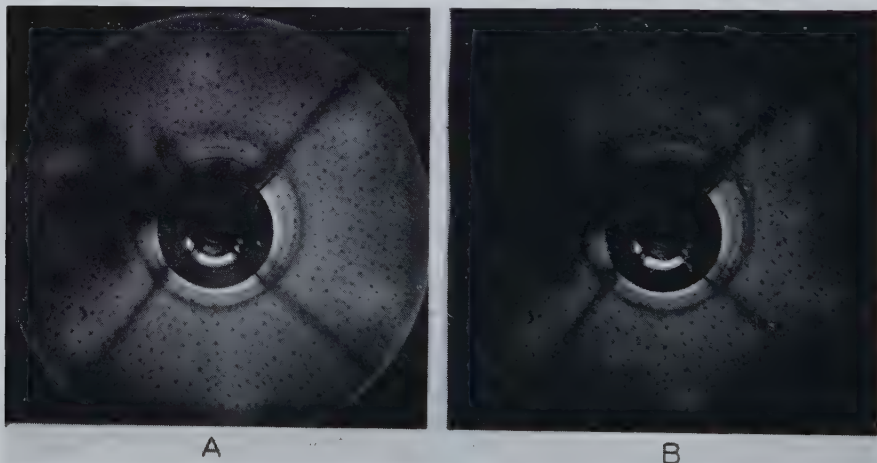
Diffraction patterns from nitrogen atoms arranged in the Q structure (see table 3). (A) 48 v ; (B) 75 v ; (C) 120 v, pattern diffuse ; (D) 120 v, pattern sharp after heating to 375°C.

Fig. 10



Diffraction pattern from a monolayer of CO molecules arranged in the 4 structure. The pattern is as sharp as one would expect from a single two-dimensional crystal.

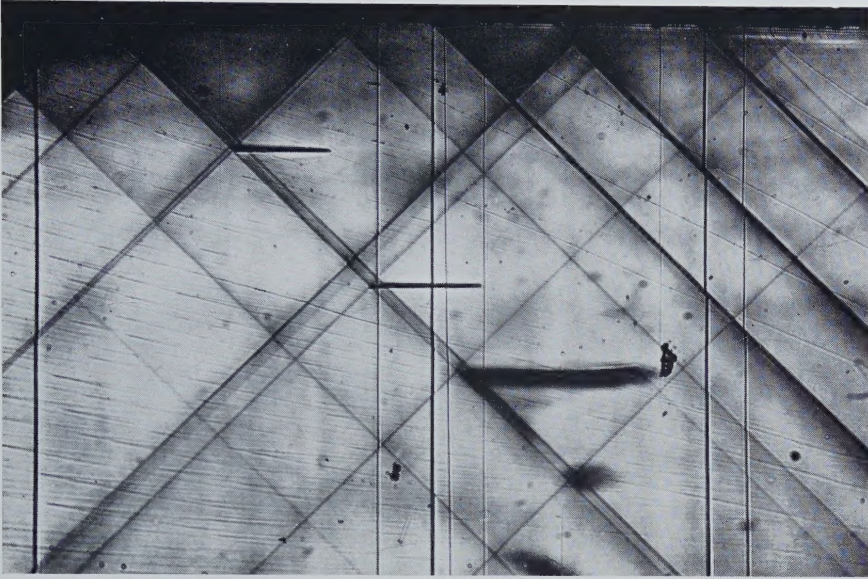
Fig. 11



Diffraction patterns from a heavy layer of oxygen on the crystal surface, so much oxygen that no patterns at all appear from the crystal itself. 82 v, 1.35 Å. Before anneal even the oxygen gave no pattern. (A) after anneal at 200°C; (B) after further anneal. Heating the crystal sufficiently to bring back the Laue beams to full intensity resulted in no further change of the oxygen pattern. Apparently the Q structure (see table 4).

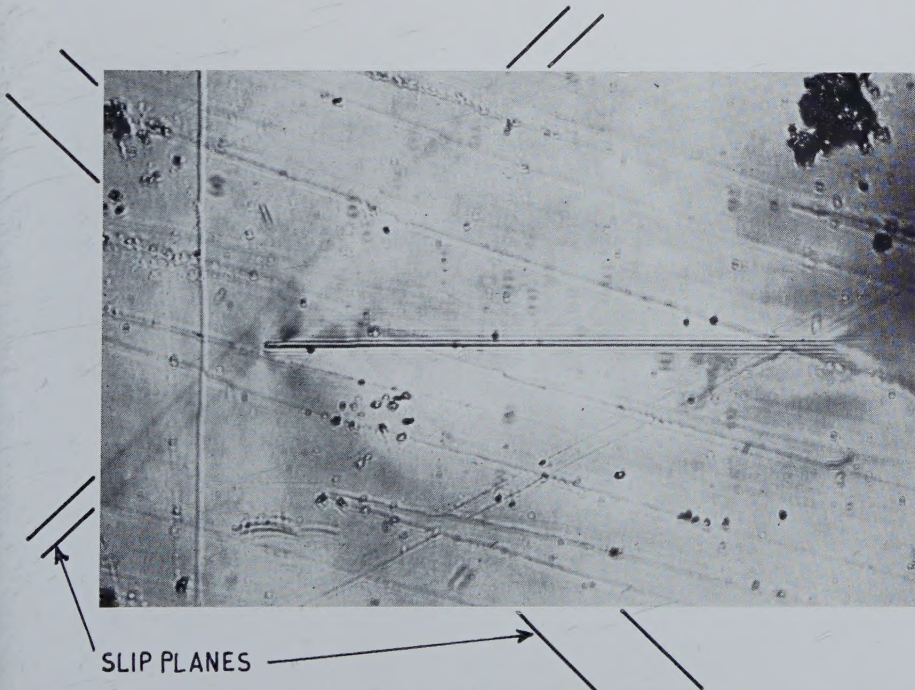


Fig. 4



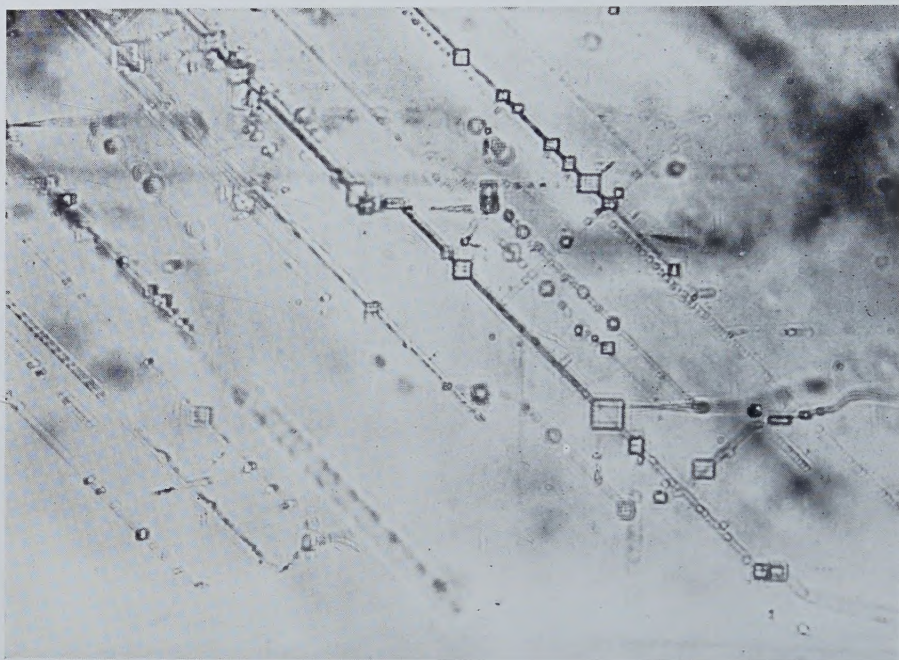
Group of three cracks seen in a lithium fluoride specimen which had been irradiated with  $4 \times 10^{15}$  1 mev electrons/cm<sup>2</sup> and then compressed 0.7% along [001]. The cracks which form on the usual (100) cleavage planes parallel to the compression axis, are initiated at slip-plane intersections. The slip planes are made visible by enhanced optical absorption produced by deformation of the irradiated crystal. (90 $\times$ .)

Fig. 5



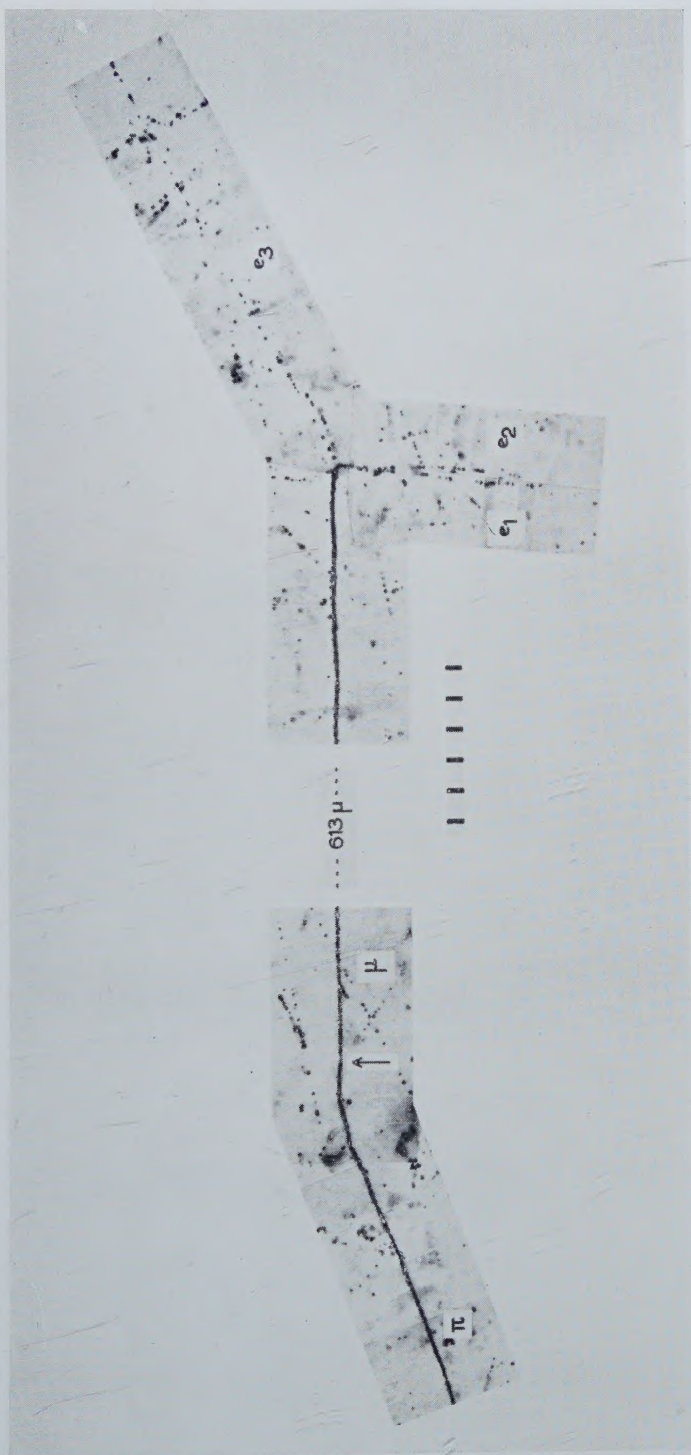
The upper crack of the group of three in fig. 4 at higher magnification. There is no sign of any component of the crack on any plane other than (100). (500 $\times$ .)

Fig. 10



Lithium fluoride single crystal annealed for  $\frac{1}{2}$  hr at  $700^{\circ}\text{C}$  after an irradiation dose of  $2 \times 10^{16}$  1 mev electrons/cm<sup>2</sup>, showing the rectangular cavities produced by vacancy condensation. The diagonal lines lie on {110} slip planes and are thought to result from non homogeneous, radiation-induced expansion of the crystal lattice.





Decay of  $\mu^+$  meson which is consistent with  $\mu^+ \rightarrow e^+ + (e^+ + e^-) + \nu + \bar{\nu}$ .

The  $613 \mu$  refers to the total range of the  $\mu$ -meson.

The scale shows 10  $\mu$  intervals.

Fig. 1

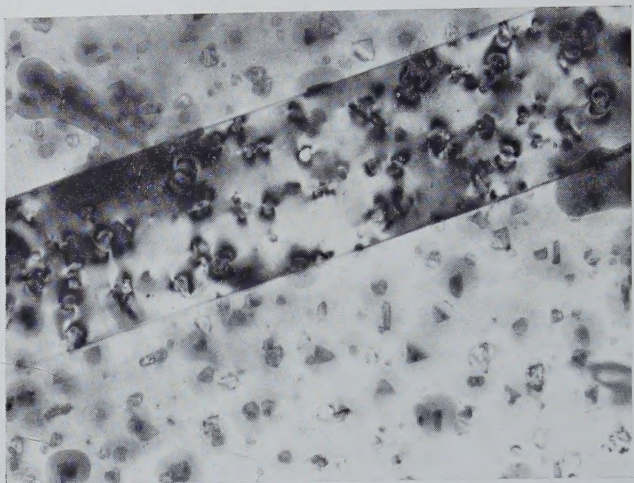


Fig. 2

$\times 60\,000$

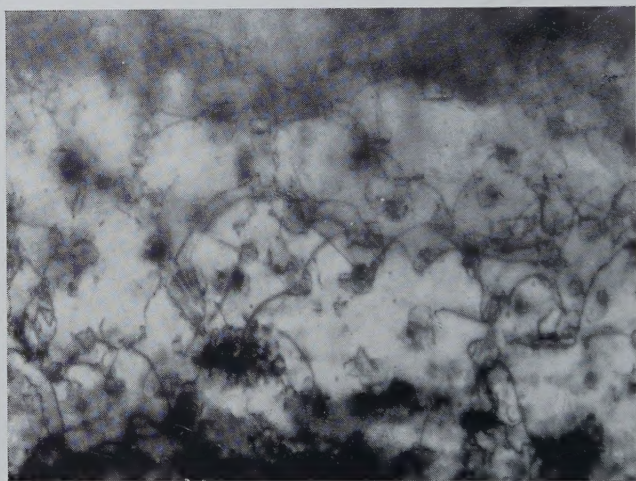
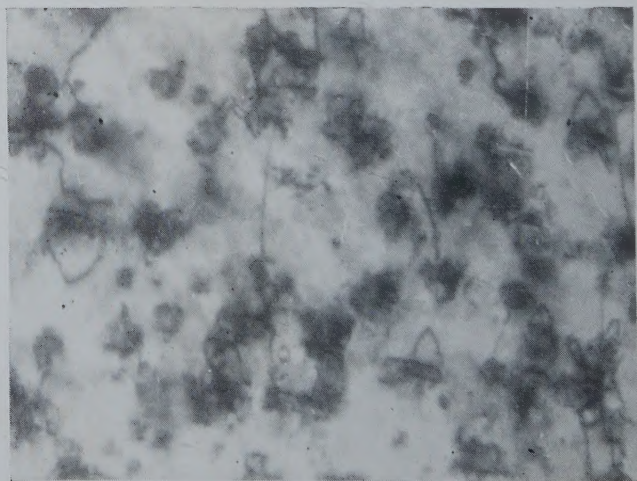


Fig. 3

$\times 60\,000$



$\times 100\,000$